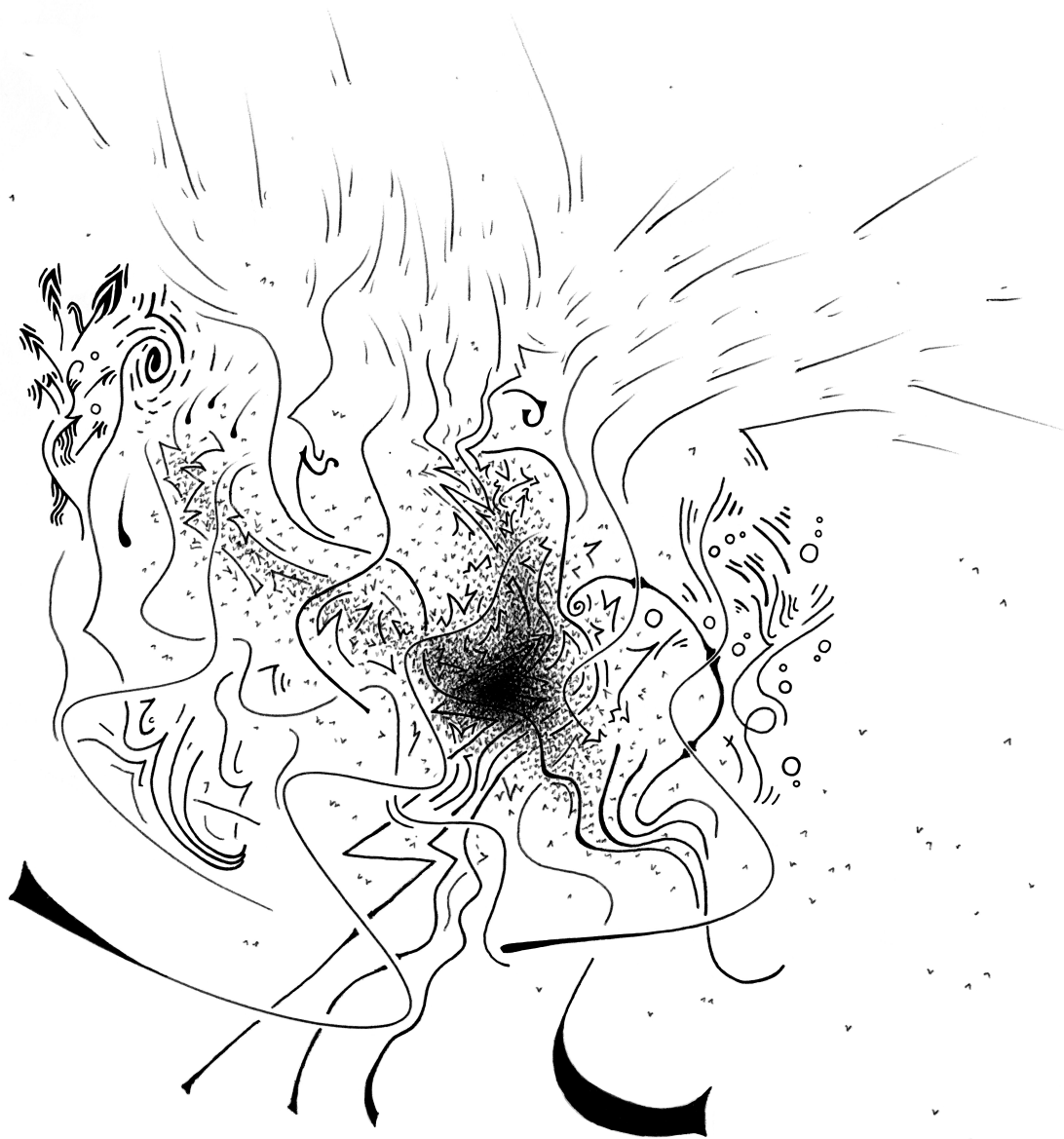# Sterile Neutrino Dark Matter

by

Samuel B. Roland

A dissertation submitted in partial fulfillment
of the requirements for the degree of
Doctor of Philosophy
(Physics)
in the University of Michigan
2017

Doctoral Committee:

Professor James D. Wells, Chair
Professor Ratindranath Akhoury
Professor Dante E. Amidei
Professor Gordon L. Kane
Professor Thomas Lam

Samuel B. Roland

rolandsa@umich.edu

ORCID iD: 0000-0003-0162-3464

Dedication

To my parents, for their love, support, and unwavering commitment to my education.

Acknowledgements

I would like to give special acknowledgements to my advisor, Professor James Wells, as well as Bibhushan Shakya. Without their patience and guidance, this work would not have been possible. I am incredibly grateful for the support I received from them while working on this research.

I would also like to thank Professors Ratindranath Akhoury, Dante Amidei, Gordon Kane, Thomas Lam, and James Wells for serving on my dissertation committee. Your time, effort, and feedback are truly appreciated.

Table of Contents

List of Tables

List of Figures

List of Appendices

Abstract

After reviewing the relevant background in cosmology and dark matter physics, we show that active neutrino masses and a keV-GeV mass sterile neutrino dark matter candidate can result from a modified, low energy see-saw mechanism if right-handed neutrinos are charged under a new symmetry broken by a scalar field vacuum expectation value at the PeV scale. The dark matter relic abundance can be obtained through active-sterile oscillations or freeze-in through its interactions with this scalar field. We focus on the observable cosmological aspects of sterile neutrino dark matter produced via the freeze-in mechanism. The study is performed in a framework that admits many cosmologically interesting variations: high temperature production via annihilation processes from higher dimensional operators or low temperature production from decays of a scalar, with the decaying scalar in or out of equilibrium with the thermal bath, in supersymmetric or non-supersymmetric setups, thus allowing us to both extract generic properties and highlight features unique to particular variations. We find that while such sterile neutrinos are generally compatible with all cosmological constraints, interesting scenarios can arise where dark matter is cold, warm, or hot, has nontrivial momentum distributions, or provides contributions to the effective number of relativistic degrees of freedom during Big Bang nucleosynthesis large enough to be probed by future measurements. We also connect our model to two recent observations: PeV energy neutrinos at IceCube and a 3.5 keV X-ray line in the spectra of several galaxies. One or both of these observations can be explained within an extended supersymmetric neutrino sector. The same symmetry under which the sterile neutrinos are charged can sufficiently stabilize an additional PeV particle, produce its abundance through the freeze-in mechanism, and lead to decays that can give the energetic neutrinos observed by IceCube. The lightest sterile neutrino, if at 7 keV, is a non-resonantly produced fraction of dark matter, and can account for the 3.5 keV X-ray line. This framework naturally provides a sterile neutrino dark matter candidate with several possibilities for its production with interesting cosmological and astrophysical signatures.

Chapter 1

Introduction

The Standard Model (SM) is an incredibly successful framework, describing physics over a vast range of energies and length scales. The theory is based upon an $SU(3) \times SU(2) \times U(1)$ gauge group, which dictates the interaction of matter and forces. Neutrinos are unique in that they are the only fermions of the SM that are uncharged under the electromagnetic and strong force; their only interaction in the SM is through the weak force. Wolfgang Pauli originally predicted their existence in order to explain the continuous spectrum of β-decay. But their meager coupling to ordinary matter lead him to suggest that neutrinos would never be discovered. In fact, he famously bet a case of champaign that no one would ever detect the elusive particle. But in 1956 when Clyde Cowan and Fred Reines detected (electron-)neutrinos from nuclear decays at the Savannah River reactor in South Carolina [1], Pauli paid up. Later, in 1962, a group at Brookhaven first detected muon-neutrinos from the decay of pions [2]. It was not until 2000 that the DONUT collaboration discovered the tau-neutrino [3], confirming that neutrinos come in three flavors.

In the SM, the Higgs field generates masses for fermions by coupling their left and right chiral states[1]. However, until recently, experimental evidence indicated that neutrinos (anti-neutrinos) only come in left-handed (right-handed) states and are extremely light, if not entirely massless. The lack of a right-handed neutrino in the particle spectrum of the SM suggests that neutrinos are massless: no renormalizable operator in the SM gives them a mass[2]. But in the late 1990s, evidence began to surface that neutrinos are more complex than the SM suggests. Observations of solar, atmospheric, reactor, and accelerator neutrinos show that they change flavor as they propagate, suggesting that flavor states are not eigenstates of

---

[1]Here, chirality refers to the representation of the Lorentz group. In the limit where a particle is massless, chirality coincides with the more familiar concept of helicity: the sign of the projection of spin onto the momentum vector.

[2]At the non-renormalizable level, one can introduce a neutrino mass term: the so-called Weinberg operator [4]. However, if one insists that lepton number is exactly conserved, then no such terms are allowed.

the free-particle Hamiltonian. The best explanation for flavor oscillations is that (i) the three neutrino eigenstates of the free-particle Hamiltonian (the "mass eigenstates") correspond to three *different* masses and (ii) the three flavor states do not coincide with the three mass eigenstates, i.e. there is a non-trivial unitary transformation between the mass and flavor states. If a particular flavor state is a linear combination of the different mass eigenstates, a simple quantum mechanical treatment of the problem demonstrates how, for example, an electron neutrino emitted from the Sun can arrive at the Earth as a muon or tau neutrino.

Adding right-handed neutrinos to the SM is a very natural extension, as every other fermion has a left- and right-handed chiral state. With this addition, a Dirac mass term for the neutrinos can emerge once electroweak symmetry is broken. However, this hypothetical right-handed neutrino differs from the other fields of the SM in that it is uncharged under the SU(3)× SU(2) × U(1) gauge group. We expect this right-handed neutrino to lack color or electromagnetic charge, just like its left-handed counterpart. But it should not have any weak interactions either, since only left-handed chiral fermions couple to the W and Z bosons of the weak force. Such a singlet fermion is often called a "sterile neutrino", a term first introduced by Bruno Pontecorvo in 1967 [5]. The only interaction of the sterile neutrino with SM particles is through its mixing via the Dirac mass term.

Because sterile neutrinos have no associated charges, they may have a mass term of their own: a Majorana mass. Unlike the Dirac mass, which involves electroweak symmetry, there is no symmetry to indicate the scale of this right-handed Majorana mass. One might naturally expect this mass to be at the Planck scale ($\sim 10^{19}$ GeV), or the scale of grand unification ($\sim 10^{16}$ GeV) if the sterile neutrino is charged under a larger group which contains the SM gauge group. Such high scales for the right-handed neutrino mass successfully predict a very small scale for the light SM neutrinos via the see-saw mechanism: heavier masses for the sterile neutrinos lead to lighter masses for the "active" ones. Indeed, a Majorana mass of $\mathcal{O}(10^{16})$ GeV leads to active neutrino masses near the meV scale, in rough agreement with oscillation experiments, as well as cosmological considerations. This type of see-saw between the active and sterile neutrino mass scales is achieved with $\mathcal{O}(1)$ dimensionless coupling constants, and is quite a natural explanation for the smallness of the active neutrino masses. However, if sterile neutrinos are as heavy as the see-saw mechanism suggests, there is very little hope of experimentally detecting them. Colliders cannot reach energies near the Planck or grand unified scale, and any heavy neutrinos that may have been present in the early Universe would have decayed away long ago.

If these sterile neutrinos have smaller masses, below the electroweak scale, they may have very interesting phenomenological implications. In particular, their lack of interactions with more familiar forms of matter suggests that sterile neutrinos might play the role of

dark matter. We know that a significant fraction of the matter in the Universe is dark - it does not interact with ordinary matter in a measurable way, other than its gravitational influence. With the right-handed neutrino being a well-motivated extension of the SM, it is worth exploring the implications of these singlet fermions comprising dark matter. Sterile neutrino dark matter has been well studied in the literature since the early 1990s. Various astrophysical and cosmological observations restrict its mass to be at the keV scale. However, most models do not offer an explanation as to why the sterile neutrino mass should fall in this range. Without a guiding symmetry or mass generation mechanism, the keV scale appears quite fine tuned. Furthermore, in order to produce the light active neutrino masses through the see-saw mechanism, a keV sterile neutrino requires dimensionless couplings of $\mathcal{O}(10^{-10})$.

The purpose of this work is to explore the consequences of coupling sterile neutrinos to new degrees of freedom in a way that naturally yields a viable dark matter candidate and produces the light active neutrino masses with $\mathcal{O}(1)$ couplings. We introduce a new symmetry that governs these interactions between sterile neutrinos and new, beyond the SM particles. These new particles will come from a well motivated extension of the SM framework: supersymmetry.

A natural resolution of the hierarchy problem has long pointed to the weak scale as the natural scale for supersymmetry. Weak scale supersymmetry was additionally motivated by the WIMP miracle[3], which offered a natural explanation of dark matter and its observed abundance. However, the predictions of the most natural setups – a light Higgs boson, weak scale superpartners (in particular stops and gluinos) within reach of the first run of the LHC, and detection of dark matter at direct detection experiments – have all failed to materialize, suggesting that the electroweak scale may be fine-tuned after all, and the scale of new physics may lie elsewhere.

Independent of such preconceived notions of naturalness, the measured mass of the Higgs boson at 125 GeV now provides a direct probe of where this scale might lie. In the Minimal Supersymmetric Standard Model (MSSM) with $\tan\beta \approx \mathcal{O}(1)$ [4], the observed Higgs mass is obtained for sfermion masses at the PeV ($= 10^6$ GeV) scale [6, 7, 8]. Even prior to the Higgs mass measurement, there were strong arguments for supersymmetry at such high scales from flavor, CP, and unification considerations [9, 10, 11, 12].

In our extension of the SM, light active neutrinos and sterile neutrino dark matter emerge naturally from connections between the neutrino sector and a new physics at the PeV scale. These interactions lead to novel production mechanisms for dark matter with interesting

---

[3]A WIMP stands for Weakly Interacting Massive Particle. This kind of dark matter, and its associated miracle, will be discussed in section 3.1.

[4]$\tan\beta$ is the ratio of the vacuum expectation values of the two Higgs doublets.

astrophysical and cosmological signatures. Our framework admits several variations, which we thoroughly explore and connect to experimental observables.

The next two chapters serve as an introduction to the basic theoretical concepts upon which this investigation is based. Chapter 2 presents a summary of the tools in cosmology that will be utilized throughout this work, while chapter 3 lays out the essentials of dark matter physics. In chapter 4 we review much of the research that has been done on sterile neutrino dark matter, with a particular focus on the production mechanisms and associated constraints. The last three chapters are based on the author's original research: [13, 14, 15]. Chapter 5 introduces the basic framework that connects sterile neutrinos with new physics at the PeV scale. Here we explore several possibilities for producing a viable dark matter candidate that is consistent will all existing experimental and observations constraints. In chapter 6 we preform a detailed analysis of the production mechanisms that are unique to our model. We carefully track the non-thermal production and evolution of dark matter in several scenarios, and explore the impact on cosmological observables. Finally, in chapter 7, we examine two observational hints that point toward the relevance of this study: a 3.5 keV X-ray line in the spectra of several galaxies [16, 17] and neutrinos with PeV scale energies at the IceCube neutrino observatory [18].

Chapter 2

Elements of Cosmology

This chapter presents a review of the basic cosmology which will be the foundation for the studies presented later on. We first introduce the Friedmann equations to explore the dynamics of the expanding Universe. Next, we turn our attention to the Boltzmann equations which will enable us to track the evolution of non-thermal particle species. This will be of critical importance to understanding the production of sterile neutrino dark matter in later chapters. In writing this chapter, the author found the following references invaluable: [19, 20, 21, 22].

2.1 Standard Cosmology

2.1.1 The Friedmann-Robertson-Walker Metric

The standard model of cosmology is built upon the framework of Einstein's theory of general relativity. To start, we assume that our Universe is homogenous and isotropic on scales larger than the Hubble length (which will be discussed below). In other words, the large scale structure of the Universe, as observed from any location and in any direction, looks the same. These assumptions single out a particular form of the metric for spacetime, the so-called Friedmann-Robertson-Walker (FRW) metric:

$$ds^2 = dt^2 - R(t)^2 \left(\frac{dr^2}{1 - kr^2} + r^2(d\theta^2 + \sin^2\theta \, d\phi^2) \right) . \qquad (2.1)$$

The spatial coordinates (r, θ, ϕ) are called *comoving* coordinates, and t is the proper time as measured by an observer at rest in a comoving frame. *Physical* distances are scaled by a factor of $R(t)$ with respect to comoving distances. This scale factor, $R(t)$, therefore describes the expansion of the Universe, the dynamics of which are described by Einstein's equations.

The constant k will determine the curvature of the Universe; depending on the sign of k the curvature will be positive, negative, or zero.

Now, a few remarks about units. Our convention here will be to take the spatial coordinate r to be dimensionless. This implies that the scale factor $R(t)$ has units of length and the constant k is dimensionless. We may always re-scale $R(t)$ and r so that $k \in \{+1, -1, 0\}$.

Another common convention is to let the coordinate r have units of length. In this convention, $R(t)$ will be dimensionless and k will have units of length^{-2}. When the scale factor is dimensionless, it is typically expressed as $a(t)$, and chosen so that today $a = 1$. This choice may always be accomplished by a re-scaling of r and k.

As the Universe expands, the momentum of a freely moving particle will scale as $|\vec{p}| \propto R^{-1}$. For a massive particle, moving non-relativistically, its kinetic energy will therefore scale as $E \propto R^{-2}$. On the other hand, for a relativistic particle (including all massless particles), its energy will scale as R^{-1}.

Now consider a photon emitted at time t_0 with frequency ω_0. If the photon is received at a later time t_1, its frequency will have been distorted by the expansion of spacetime to a different frequency ω_1. Since the frequency of the photon is proportional to its energy, we know that the frequency scales as

$$1 + z \equiv \frac{\omega_0}{\omega_1} = \frac{R(t_1)}{R(t_0)}, \tag{2.2}$$

where we have introduced the *redshift* z. When astronomers observe distant galaxies, they appear redshifted ($z > 0$), implying that $R(t)$ is increasing with time, i.e. the Universe is expanding.

The rate of expansion is often characterized by the Hubble parameter $H \equiv \dot{R}/R$. The present value of the Hubble parameter, H_0, is called the Hubble constant. Using observations of the Planck space observatory, the Planck collaboration has determined the Hubble constant to be

$$H_0 = 67.8 \pm 0.9 \text{ km s}^{-1} \text{ Mpc}^{-1} \tag{2.3}$$

[23]. This measurement is often parameterized by h, defined as

$$h = \frac{H_0}{100 \text{ km s}^{-1} \text{ Mpc}^{-1}}. \tag{2.4}$$

2.1.2   Dynamics of the FRW Model

The evolution of the FRW metric, which is completely described by the scale factor $R(t)$, is governed by Einstein's equations. These equations describe the coupled dynamics of the

spacetime metric and matter content of the Universe:

$$R_{\mu\nu} - \frac{1}{2}g_{\mu\nu}\mathcal{R} = 8\pi G T_{\mu\nu} + \Lambda g_{\mu\nu} \tag{2.5}$$

where $R_{\mu\nu}$ and $\mathcal{R}$ are the Ricci tensor and scalar, respectively, and $T_{\mu\nu}$ is the symmetric stress-energy tensor for all matter in the Universe. G is Newton's constant, which in natural units defines the Planck mass

$$M_{Pl} = \frac{1}{\sqrt{G}} = 1.22 \times 10^{19} \text{ GeV}. \tag{2.6}$$

We have also included the contribution of a cosmological constant Λ, which can be seen as a contribution to the stress-energy tensor from the vacuum.

The stress-energy tensor, $T_{\mu\nu}$, contains all the information about the state of matter in the Universe. We will make the approximation that the Universe is filled with an isotropic fluid, characterized only by its energy density, ρ, and pressure, P, which is at rest in the comoving frame. In this case the stress-energy tensor is simply

$$T_{\nu}^{\mu} = \text{diag}(\rho, -P, -P, -P). \tag{2.7}$$

From the local conservation of energy and momentum, $\nabla_{\nu}T^{\mu\nu} = 0$, the $\mu = 0$ component gives the first law of thermodynamics for this ideal fluid:

$$\frac{\mathrm{d}}{\mathrm{d}t}\left(\rho R^3\right) = -P\frac{\mathrm{d}R^3}{\mathrm{d}t}. \tag{2.8}$$

The energy density and pressure are further related by the equation of state for the specific kind of energy in question. We will be concerned with three types of energy that have very simple equations of state:

Matter

Non-relativistic matter (usually just called "matter") is well approximated as a pressureless gas, or dust. Setting $P_M = 0$ in equation 2.8 yields the conservation law

$$\frac{\mathrm{d}}{\mathrm{d}t}\left(\rho_M R^3\right) = 0. \tag{2.9}$$

This implies that the energy density of matter scales as $\rho_M \propto R^{-3}$.

Radiation

For relativistic matter (or radiation), the pressure and energy density are related by $P_R = \frac{1}{3}\rho_R$. Substituting this equation of state into 2.8 reveals that the energy density of radiation scales as $\rho_R \propto R^{-4}$. Therefore, given some mixture of radiation and matter, the ratio of matter to radiation energy density will *increase* proportionally to R. Indeed, after an early period of radiation domination, matter came to dominate the composition of the Universe.

Vacuum

The equation of state for the vacuum cannot be derived, as no fundamental theory for its structure exists as of yet. Still, we can make some reasonable assumptions about its behavior. We assume that the energy density is positive and constant in time and space, and therefore $\mathrm{d}\rho_{vac}/\mathrm{d}t = 0$. Then from equation 2.8 we find that $P_{vac} = -\rho_{vac}$, so the vacuum pressure is negative and constant in time and space.

We can incorporate the cosmological constant as a term in the stress-energy tensor by defining

$$T_{\mu\nu,\Lambda} = \frac{\Lambda}{8\pi G} g_{\mu\nu} . \tag{2.10}$$

Then we may interpret the energy density associated with Λ as the 0–0 component of $T_{\mu\nu,\Lambda}$, so that $\rho_\Lambda = \frac{\Lambda}{8\pi G}$. Therefore this cosmological constant introduces a positive energy density that is constant in time and space, and so we identify this with the vacuum energy.

All three examples can be summarized by the equation of state $P = w\rho$ where

$$w = \begin{cases} 0 & \text{Matter} \\ 1/3 & \text{Radiation} \\ -1 & \text{Vacuum } (\Lambda) \end{cases} . \tag{2.11}$$

The first law of thermodynamics in 2.8 can be integrated in general to yield

$$\rho = \rho_0 \left(\frac{R}{R_0}\right)^{-3(1+w)} . \tag{2.12}$$

Entering the form the of the stress-energy tensor in 2.7 into Einstein's equations in 2.5, gives the Friedmann equations, which govern the evolution of the scale factor R. The 0–0

component, after some arduous calculations, yields

$$\frac{\dot{R}^2}{R^2} + \frac{k}{R^2} = \frac{8\pi G}{3}\rho \,, \tag{2.13}$$

where we have incorporated the cosmological constant, Λ, into the total energy density ρ as described above.

Now let us examine some illuminating ways to express this Friedmann equation. First, we will define $\Omega \equiv \rho/\rho_c$, the ratio of the total energy density to the *critical density*:

$$\rho_c = \frac{3H^2}{8\pi G} \,. \tag{2.14}$$

Note that here, we have defined the critical density, ρ_c, as a time depended quantity. With this definition, the Friedmann equation becomes

$$\frac{k}{H^2 R^2} = \Omega - 1 \,. \tag{2.15}$$

From 2.15 we see that if the energy density equals the critical density, at any point in time, then $k = 0$, i.e. the Universe is flat. Indeed, the sign of $\Omega - 1$ determines whether the Universe is open ($\Omega > 1, k = +1$), flat ($\Omega = 1, k = 0$), or closed ($\Omega < 1, k = -1$).

The Friedmann equation suggests that we may interpret the curvature of the Universe as yet another contribution to the total energy density, in a similar manner to the cosmological constant. Let us define this contribution as $\Omega_k = -k/H^2 R^2$. Now the the Friedmann equation reads:

$$\Omega_M + \Omega_R + \Omega_\Lambda + \Omega_k = 1 \,, \tag{2.16}$$

where we have separated the total energy density out into the separate forms discuss above.

To better see how things scale with R, let us pull out the values of the energy densities today. Define the constant $\Omega_{X,0}$ to be the present value of Ω_X, for $X \in \{M, R, \Lambda, k\}$. Based on the discussion above, we know how the various types of energy densities scale with R. Using this knowledge, and keeping in mind that we have defined ρ_c in a time dependent way, we can seperate out the constants $\Omega_{X,0}$ from equation 2.16 to get

$$\left(\frac{H}{H_0}\right)^2 = \Omega_{R,0}\left(\frac{R}{R_0}\right)^{-4} + \Omega_{M,0}\left(\frac{R}{R_0}\right)^{-3} + \Omega_{k,0}\left(\frac{R}{R_0}\right)^{-2} + \Omega_{\Lambda,0} \,. \tag{2.17}$$

From this form of the Firedmann equation we can see the as the Universe expands, the vacuum inevitably dominates the energy density of the Universe. This should not be surprising, since we have assumed that the vacuum energy density is constant, where as all other forms

of energy discussed here get diluted by the expansion of spacetime.

There is one critical assumption that we have made in deriving 2.17 that we should keep in mind. We have assumed that, given our knowledge of the present energy density in a given form, $\Omega_{X,0}$, we can determine the energy density Ω_X at another time simply by taking into account the dilution of energy due to the expansion of the Universe. However, we have failed to take into account the fact that energy can change between radiation and matter. For example, in the very early Universe when temperatures are higher than the mass of every particle species in the thermal bath, every particle is relativistic and therefore counts as radiation. But when the temperature drops below the mass of a particular particle species, that species will behave as non-relativistic matter. On the other hand, some heavy, non-relativistic particle species which is abundant at an early time can decay into very light particles that behave as radiation. Therefore, as the temperature of the Universe changes and particle species interact and decay, energy can shift between matter, radiation, and something in between. For these reasons, we will need to adopt more sophisticated machinery to better model the evolution of the Universe. This will be done in the next section. Equation 2.17 is only a good approximation when energy can be divided neatly into radiation and matter, and there is no changing between the two.

If the Universe is dominated by a single form of energy with the equation of state $p = w\rho$, we can explicitly solve the Friedmann equation 2.13 for $R(t)$

$$R(t) = \begin{cases} R_0 \, (t/t_0)^{\frac{2}{3(1+w)}} & w \neq 1 \\ R_0 e^{\sqrt{\Lambda/3}\,(t-t_0)} & w = 1 \end{cases}. \tag{2.18}$$

As stated before, the Universe will eventually become vacuum dominated if a cosmological constant term is present. Therefore, Λ drives the Universe towards exponential expansion with a constant Hubble rate $H = \sqrt{\Lambda/3}$.

Before moving on, let us make one final comment about the curvature contribution to the energy density Ω_k. The Planck collaboration has used its observations of the cosmic microwave background (CMB) to estimate the deviation of our Universe from a flat one. Measurements of the CMB temperature, polarization, and gravitation lensing potential power spectra, combined with observations of the baryon acoustic oscillation (BAO) measurements, constrain the present value of Ω_k to be

$$\Omega_{k,0} = 0.000 \pm 0.005 \text{ (at 95\% C.L.)} \tag{2.19}$$

[23]. Our Universe appears to be very well described by a flat FRW metric ($k = 0$). Or in other words, the total energy density of the Universe is very close to the critical density.

Furthermore, glancing at equation 2.17, we see that while going back in time, the impact of the curvature term becomes more and more suppressed when compared with matter and radiation. Therefore, our Universe was even closer to being critical in the past. For the remainder of this work we shall set $k = 0$, taking spacetime to be flat.

2.2 Statistical Mechanics in an Expanding Universe

2.2.1 The Boltzmann Equation

The Freidmann equations, derived in the pervious section, tell us that the dynamics of the scale factor R are dictated by the energy content of the Universe. We also saw some simple forms of energy that evolve differently as the Universe expands. However, the simple scaling of energy densities with R cannot capture full dynamics of interacting particles. In order to describe the evolution of matter throughout the history of the Universe, we will take the statistical mechanics approach: deriving the macroscopic quantities of interest (energy density, number density, pressure) from the microscopic behavior of particles.

The fundamental quantity from this perspective is the density function over phase space of a given particle species, $f(x^\mu, p^\nu)$. Its evolution along a geodesic, parameterized by an affine parameter λ, is described by the Liouville operator

$$L[f] \equiv \frac{\mathrm{d}}{\mathrm{d}\lambda} f(x^\mu(\lambda), p^\nu(\lambda)) \,. \tag{2.20}$$

Using the geodesic equation of motion, we may express the Liouville operator as

$$L[f] = \frac{\partial f}{\partial x^\mu} \frac{\mathrm{d}x^\mu}{\mathrm{d}\lambda} + \frac{\partial f}{\partial p^\nu} \frac{\mathrm{d}p^\nu}{\mathrm{d}\lambda} = \frac{\partial f}{\partial x^\mu} p^\mu - \frac{\partial f}{\partial p^\nu} \Gamma^\nu_{\ \rho\sigma} p^\rho p^\sigma \,, \tag{2.21}$$

where $\Gamma^\nu_{\ \rho\sigma}$ are the Christoffel symbols, derived from the background metric.

For the case of interest, a flat FRW metric, we may simplify the Liouville operator considerably. Since this spacetime is homogenous and isotropic, f will be independent of the spacial coordinates x^i, and will only depend on time, t, and the magnitude of the three-momentum $p \equiv (p^i p_i)^{1/2}$. The final result in this case is

$$L[f] = \frac{\partial f(t, p)}{\partial t} - Hp \frac{\partial f(t, p)}{\partial p} \,. \tag{2.22}$$

For a complete and detailed derivation of this form of the Liouville operator, the reader is referred to the monograph by Bernstein [24].

Given a set of non-interacting particles, there will be no variation of f along a geodesic

11

trajectory, hence $L[f] = 0$. For interacting particles, the right-hand-side of this equation is replaced by a collision integral $C[f]$, which gives the rate at which particles enter the volume of phase space with momentum p minus the rate at which particles leave this volume. This equation, $L[f] = C[f]$, is named after its originator, Ludwig Boltzmann (1844 - 1906).

Each type of collision involving the particle species in questions will contribute to the collision term $C[f]$. For example, a scattering process such as $a + b \leftrightarrow c + d$ will influence the phase space density of a particles, f_a. The corresponding collision term will depend on the joint density of a and b particles, f_{ab}. Boltzmann's critical insight was to make the approximation of molecular chaos, or "Stosszahlansatz", which implies that the momentum of a and b particles are statistically independent, so the join distribution may be separated: $f_{ab} = f_a f_b$. This simplification allows us, in principle, to solve the Boltzmann equation for the single particle densities, without running into an infinite hierarchy of multi-particle density functions.

In general, the collision term for a particular phase space density f_X and scattering process $X + i + j + \ldots \leftrightarrow a + b + \ldots$ is given by:

$$C[f_X] = \frac{1}{2E_X} \int \left(\prod_{I=i,j,\ldots} d\Pi_I \right) \left(\prod_{A=a,b,\ldots} d\Pi_A \right) (2\pi)^4 \, \delta^4 \left(\Sigma p \right) |\mathcal{M}|^2 \times \qquad (2.23)$$
$$\times \, \Omega(X + i + j + \ldots \leftrightarrow a + b + \ldots) \, ,$$

where the integration measure is the standard Lorentz invariant phase space measure

$$d\Pi_x = \frac{g_x}{(2\pi)^3} \frac{d^3 p_x}{2E_x} \, , \qquad (2.24)$$

and g_x counts the internal degrees of freedom of particle x. The delta function $\delta^4 \left(\Sigma p \right)$ ensures that energy and momentum are conserved during the scattering process. The factor Ω is the phase space density weight, given by

$$\Omega(X+i+j+\ldots \leftrightarrow a+b+\ldots) = f_i f_j \ldots f_X (1 \pm f_a)(1 \pm f_b) \ldots - f_a f_b \ldots (1 \pm f_i)(1 \pm f_i) \ldots (1 \pm f_X) \, , \qquad (2.25)$$

with + for bosons and - for fermions. $|\mathcal{M}|^2$ is the squared matrix element for the scattering process of interest, averaged over initial and final states, including any symmetry factors. We have implicitly assumed CP invariance here, so that the matrix elements for $X + i + j + \ldots \rightarrow a + b + \ldots$ and the reverse process $a + b + \ldots \rightarrow X + i + j + \ldots$ are equal.

With the phase space density at hand, the macroscopic quantities of interest may be easily determined. For example, the number density n and stress-energy tensor $T^{\mu\nu}$ are

given by

$$n(t) = g \int \frac{\mathrm{d}^3 p}{(2\pi)^3} f(t, p) \,, \tag{2.26}$$

$$T^{\mu\nu} = g \int \frac{\mathrm{d}^3 p}{(2\pi)^3} \frac{p^\mu p^\nu}{E} f(t, p) \,. \tag{2.27}$$

Each of these macroscopic quantities, obtained from a specific kind of integration over phase space, has a corresponding integrated Boltzmann equation. For instance, applying the phase space integration to the Boltzmann equation:

$$g \int \frac{\mathrm{d}^3 p}{(2\pi)^3} \left(L[f] = C[f] \right) \,, \tag{2.28}$$

yields a simple formula for the evolution of number density n:

$$\dot{n} + 3Hn = g \int \frac{\mathrm{d}^3 p}{(2\pi)^3} C[f] \,. \tag{2.29}$$

Therefore, the number density of a non-interacting species (for which $C = 0$) scales as $n \propto R^{-3}$.

When many particle species are interacting, the full set of Boltzmann equations can be rather complicated. The phase space density of a given particle appears in the collision term for every other species with which it interacts. Therefore, these integral-differential equations are coupled, making them difficult to solve in general. Luckily, it is often the case that many of the particles involved will be in thermodynamic equilibrium and their phase space density is already known. This can greatly reduce the complexity of the Boltzmann equations, making it tractable to solve for the density of particle species that are out of equilibrium.

2.2.2 Equilibrium Thermodynamics

Looking back at equation 2.29, we can identify two effects on the evolution of number density: the expansion of the Universe and interactions with other particles. As we have seen above, if the effect of expansion dominates, the number density will simply be diluted. On the other hand, if the interaction rate per particle, Γ, is much larger than the expansion rate, H, then the particle species will reach local thermodynamic equilibrium, just like the familiar case of a non-expanding Universe.

Let us first consider elastic scattering between two particle species: $a + b \leftrightarrow a + b$. If these events occur rapidly (in the sense described above), the two species are in *kinetic*

13

equilibrium. In this case, the rate at which scattering causes particles to enter an infinitesimal volume of phase space will equal the rate at which they leave. Or in other words, $C = 0$ for this scattering process, despite the fact that there are many, many collisions happening[1]. Recalling the definition of the collision term in 2.23, its vanishing implies that $\Omega(a + b \leftrightarrow a + b) = 0$. For simplicity, we will treat the particles classically, dropping the factors of $(1 \pm f)$ everywhere. Therefore, in kinetic equilibrium we have

$$\ln f_a(p) + \ln f_b(p') = \ln f_a(p_1) + \ln f_b(p_2) \tag{2.30}$$

where p, p' are the momenta of the incoming particles and p_1, p_2 are the momenta of the outgoing particles. This represents an additively conserved quantity for the collision. Given that the only conserved quantities are particle number, energy, and momentum, we may conclude that the equilibrium distribution takes the form

$$\ln f_{eq}(p) = \alpha + \beta_\mu p^\mu \,. \tag{2.31}$$

Furthermore, requiring f_{eq} to be isotropic and bounded as p goes to infinity, we have

$$\ln f_{eq}(p) = \alpha - \beta E \,. \tag{2.32}$$

The positive parameter β is denoted as the inverse temperature: $\beta \equiv 1/T$. We see that if the population of a and b particles are in kinetic equilibrium (so equation 2.30 is satisfied), they share a common temperature.

The parameter α is typically expressed as $\alpha \equiv \mu/T$, and we may identify μ as the chemical potential. Now let us consider a more general 2-2 scattering: $a + b \leftrightarrow c + d$. If these scattering processes occur rapidly, the particles are in *chemical equilibrium.* A similar argument to the case above requires $\mu_a + \mu_b = \mu_c + \mu_d$ when these particles are in chemical equilibrium.

We have found that classical particles in kinetic equilibrium share a common temperature, T, and satisfy the Maxwell-Boltzmann distribution[2]

$$f(p, t) = \exp(-(E - \mu)/T) \,. \tag{2.33}$$

---

[1]More formally, the fact that $C = 0$ in equilibrium may be derived from the fact entropy has reached a maximum value and so the entropy current is covariantly conserved. See, for example, the discussions in [24] and [25] about equilibrium states in an FRW background.

[2]We have still not shown that $L[f_{eq}] = 0$. It turns out that in general, this equation cannot be solved for a massive particle species. Therefore, strictly speaking, there are no equilibrium solutions to the Boltzmann equation in an FRW background when $m \neq 0$. However, the distribution we derived is an approximate solution to the Boltzmann equation when $\Gamma \gg H$. For a detailed discussion see [24].

A full quantum mechanical treatment of the equilibrium distribution will result in a small modification, yielding the familiar Fermi-Dirac or Bose-Einstein distribution

$$f(p,t) = \left[\exp((E-\mu)/T) \pm 1\right]^{-1} ,$$

(2.34)

with + for fermions or - for bosons.

With these equilibrium distributions, we may determine macroscopic observables in terms of the temperature. For example the number density, energy density, and pressure take a simple form in the relativistic and non-relativistic limits, with zero chemical potential:

Non-relativistic ($m \gg T$)	Relativistic ($m \ll T$)
$n = g\left(\frac{mT}{2\pi}\right)^{3/2} e^{-m/T}$	$n = \frac{\zeta(3)}{\pi^2} g T^3 \times \begin{cases} 1 & \text{Boson} \\ 3/4 & \text{Fermion} \end{cases}$
$\rho = nm$	$\rho = \frac{\pi^2}{30} g T^4 \times \begin{cases} 1 & \text{Boson} \\ 7/8 & \text{Fermion} \end{cases}$
$P = nT$	$P = \rho/3$

A few comments about these macroscopic quantities are in order. First, we can confirm that the equations of state for radiation and matter used in the previous section are approximately correct. Second, in the non-relativistic case, bosons and fermions behave the same. This is to be expected since the Fermi-Dirac and Bose-Einstein distributions both reduce to the Maxwell-Boltzmann distribution in this limit.

Finally, notice that non-relativistic matter in equilibrium will have an exponentially suppressed abundance. Because of this so-called "Boltzmann suppression", it is common to ignore the contribution of non-relativistic matter when calculating the total energy density of particles in equilibrium, ρ_R, which is typically expressed as

$$\rho_R = \frac{\pi^2}{30} g_* T^4 .$$

(2.35)

Here g_* counts the effective number of relativistic degrees of freedom:

$$g_* = \sum_{i=\text{Rel. Bosons}} g_i \left(\frac{T_i}{T}\right)^4 + \frac{7}{8} \sum_{i=\text{Rel. Fermions}} g_i \left(\frac{T_i}{T}\right)^4 ,$$

(2.36)

where we allow for the possibility that different species have different temperatures. In this

case, and from here on out, T is taken to be the temperature of the photons.

We will conclude this section with a brief discussion of entropy. Recall the thermodynamic definition of entropy, S:

$$TdS = dQ = dU + dW . \tag{2.37}$$

In the expanding Universe with an element of comoving volume $V = R^3$, this becomes

$$TdS = d(\rho V) + PdV . \tag{2.38}$$

From our equilibrium expressions for ρ and P, it is easy to check the relation

$$dP = \frac{\rho + P}{T}dT . \tag{2.39}$$

Combining expressions 2.38 and 2.39, we find that

$$dS = d\left[\frac{(\rho + P)V}{T}\right] \quad \Rightarrow \quad S = \frac{(\rho + P)V}{T} + \text{constant} . \tag{2.40}$$

With this expression for entropy, one can check that entropy is conserved using the first law of thermodynamics (2.8). We also introduce the entropy density $s \equiv S/V$. Using our expressions for ρ and P in equilibrium, we find that

$$s = \frac{2\pi^2}{45}g_{*s}T^3 , \tag{2.41}$$

where, again, we have only included the relativistic particles so that

$$g_{*s} = \sum_{i=\text{Rel. Bosons}} g_i \left(\frac{T_i}{T}\right)^3 + \frac{7}{8} \sum_{i=\text{Rel. Fermions}} g_i \left(\frac{T_i}{T}\right)^3 . \tag{2.42}$$

Now, conservation of entropy provides the very useful relation:

$$g_{*S}T^3R^3 = \text{constant} . \tag{2.43}$$

As long as particles remain relativistic and in equilibrium, $T \propto R^{-1}$. When particles do fall out of equilibrium, they transfer their entropy to the other thermal particles, causing T to fall at a slower rate than R^{-1}.

Chapter 3

Dark Matter Basics

Dark matter is an elusive, yet critical, ingredient of our Universe. It comprises roughly a quarter of the Universe's energy, yet every attempt so far to directly detect its presence has yielded null results. Its minuscule interaction with everyday matter is a clear sign that the SM must be extended to incorporate dark matter. In this chapter, we will review several theories on the origin of dark matter and the ways in which dark matter may have impacted structure formation in our Universe. In later chapters, when building viable models for sterile neutrino dark matter, we will utilize the production mechanisms explored here and find that the observed structures in the Universe provide important constrains on these models.

3.1   Freeze-Out and the WIMP Miracle

In the early Universe, before the electroweak phase transition, every particle in the SM was tightly coupled in a thermal bath of radiation[1]. As time progressed, and the temperature dropped, various species decoupled from the thermal bath. Depending on the details of this decoupling, these thermal relics can have a sizable abundance today. For example, a few seconds after the Big Bang, the rate of weak interactions which kept neutrinos in equilibrium became overwhelmed by the expansion rate of the Universe. These neutrinos decoupled from the thermal photons and electrons, and have been essentially traveling freely until the present day. At the time of their decoupling, the temperature of the thermal bath was around an MeV. Hence, these neutrinos were highly relativistic and constituted a significant fraction of the energy density when they decoupled. What remains today is the cosmic neutrino background. If these relic neutrinos constituted a significant fraction of dark matter today,

---

[1]If the reheat temperature after inflation is high enough ($\gtrsim 10^{16}$ GeV) there would have been a period where the interactions mediated by massless gauge bosons were not strong enough to maintain equilibrium for SM particles.

the large scale structure of the Universe would have turned out very differently. However, dark matter may have been produced in a similar manner to the cosmic neutrino background.

To get an estimate for the energy density of a thermal relic χ, we begin with the integrated Boltzmann equation for number density

$$\dot{n}_\chi + 3Hn_\chi = g_\chi \int \frac{\mathrm{d}^3p}{(2\pi)^3} C[f_\chi] \, . \tag{3.1}$$

Suppose that χ maintains chemical equilibrium with some thermal species ψ through annihilations: $\chi\bar{\chi} \leftrightarrow \psi\bar{\psi}$. Using a Maxwell-Boltzmann distribution for ψ, and invoking energy conservation for each annihilation, the integrated collision term may be expressed as

$$g_\chi \int \frac{\mathrm{d}^3p}{(2\pi)^3} C[f_\chi] = -\langle \sigma_{\chi\bar{\chi}\to\psi\bar{\psi}} |v| \rangle \left(n_\chi^2 - n_{\chi\,\mathrm{eq}}^2 \right) \, , \tag{3.2}$$

where $n_{\chi\,\mathrm{eq}}$ is the number density of χ if it was in thermal equilibrium (with a Maxwell-Boltzmann distribution), and the thermal average of the cross section is defined as

$$\langle \sigma_{\chi\bar{\chi}\to\psi\bar{\psi}} |v| \rangle = n_{\chi\,\mathrm{eq}}^{-2} \int \mathrm{d}\Pi_\chi \, \mathrm{d}\Pi_{\bar{\chi}} \, \mathrm{d}\Pi_\psi \, \mathrm{d}\Pi_{\bar{\psi}} \, (2\pi)^4 \, \delta^4 \left(\Sigma p \right) |\mathcal{M}|^2 \exp\left(-(E_\chi + E_{\bar{\chi}})/T \right) \, . \tag{3.3}$$

Here we have assumed there is no difference in number density between particle and anti-particle, and we have also assumed that the phase space density of χ is proportional to a thermal density. This last assumption is reasonable since scattering ($\chi\psi \leftrightarrow \chi\psi$) typically maintains kinetic equilibrium even after χ falls out of chemical equilibrium.

We may also simplify the left side of the Boltzmann equation by introducing the yield, $Y_\chi \equiv n_\chi/s$, where s is the entropy density. This normalization of the number density removes the effect of the expansion of the Universe, since $s \propto R^3$ (as we saw in section 2.2.2). With this definition, the Boltzmann equation reads

$$\frac{x}{Y_{\chi\,\mathrm{eq}}} \frac{\mathrm{d}Y_\chi}{\mathrm{d}x} = -\frac{\Gamma}{H} \left[\left(\frac{Y_\chi}{Y_{\chi\,\mathrm{eq}}} \right)^2 - 1 \right] \, , \tag{3.4}$$

where $x \equiv m_\chi/T$ and $\Gamma = n_{\chi\,\mathrm{eq}} \langle \sigma|v| \rangle$ is the interaction rate.

In this form, the Boltzmann equation has a simple interpretation. The yield, Y_χ, is rapidly driven to its equilibrium value when $\Gamma \gg H$. As discussed in section 2.2.2, this is precisely the condition to maintain local thermodynamic equilibrium. On the other hand, when $\Gamma \ll H$, the χ population simply evolves as a non-interacting species.

The time when $\Gamma \sim H$ determines the remaining abundance today. Barring changes in the degrees of freedom in the thermal bath (g_{*s}), the equilibrium yield will be constant for

a relativistic species, and for a non-relativistic species: $Y_{\chi\,\mathrm{eq}} \propto \exp(-m_\chi/T)$. Therefore, if χ remains in equilibrium until temperatures well below its mass, its abundance will become highly suppressed by the time it freezes out. Therefore, stronger interactions with thermal particles lead to a smaller relic abundance today. This is illustrated in 3.1 for a particle species with mass and interaction cross section at the weak scale.
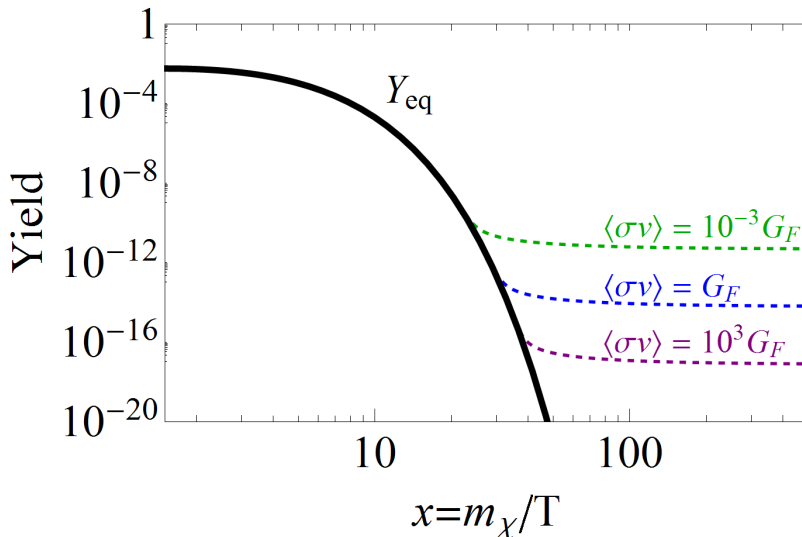

Figure 3.1: Numerical solutions to equation 3.4. Here we have set $m_\chi = 100$ GeV and $\langle \sigma v \rangle = G_F \times \{10^{-3}, 1, 10^3\}$, corresponding to the green, blue, and purple dashed lines, respectively. $G_F = 1.166 \times 10^{-5}$ GeV^{-2} is the Fermi constant. The black line denotes the equilibrium yield. Notice that despite the 6 orders of magnitude in variation of $\langle \sigma v \rangle$, freeze-out always takes place around $x \simeq 20 - 40$.

The "WIMP miracle" is the astonishing fact that a weakly interacting massive particle (WIMP), with its mass and interaction strength set by the weak scale, will freeze out to roughly the observed abundance of dark matter. Of course this WIMP, if it is to be a suitable dark matter candidate, must be stable and electrically neutral. Such particles are generic predictions of supersymmetric extensions of the SM with weak scale superpartners. In these models, there are four neutral superpartners to the gauge bosons, called neutralinos. The lightest neutralino is generally stable and is an excellent candidate for WIMP dark matter. For a review of the motivation and phenomenology behind supersymmetric WIMP dark matter, see [26, 27].

3.2 Freeze-In

Thermal freeze-out is a very useful tool for model builders when trying to explain the origin of dark matter. Since the decoupling process takes place at temperatures slightly lower than the mass of dark matter, we do not need a UV complete model or perfect knowledge of the early Universe to make concrete predictions in this framework. This fact, along with the WIMP miracle, makes thermal freeze-out a favorite model for dark matter. However, we have yet to detect dark matter particles with mass and cross section near the weak scale. It is therefore important to investigate alternative production mechanisms, which might have different experimental signatures and theoretical advantages.

One of the critical assumptions of the freeze-out paradigm is that dark matter interacts with the thermal bath strongly enough to maintain equilibrium. We will now investigate the possibility that dark matter is so weakly interacting (weaker than the weak scale) that it never entered thermal equilibrium. In contrast to freeze-out, we will assume that this decoupled particle species has a negligible abundance in the early Universe. Such a dark matter candidate, often called a FIMP ("Feebly Interacting Massive Particle"), will "freeze in" during the early Universe through its tiny coupling with the thermal radiation [28]. In this case stronger interactions lead to more dark matter production, opposite of what happens in the freeze-out scenario.

As we will soon see, freeze-in proceeds differently depending on whether the interactions are mediated by a renormalizable or non-renormalizable operator. In either case, one must ensure that the interactions are small enough to prevent the dark matter from reaching equilibrium, i.e. $Y_{\rm DM} < Y_{\rm eq}$. For renormalizable operators, this means a small dimensionless coupling is necessary in most circumstances. For example, if scalar dark matter χ freezes in due to interactions with fermionic bath particles ψ mediated by the operator $\lambda \bar{\psi} \psi \chi$, then $\lambda \lesssim 10^{-6} \sqrt{m_\psi / 100 \text{ GeV}}$ to prevent χ from reaching equilibrium [29]. On the other hand, non-renormalizable operators come with a suppression of some power of the cut-off scale, M_*, for the effective theory. In this case, M_* must be high enough to ensure $Y_{\rm DM} < Y_{\rm eq}$. For more details about the constraints on M_* in freeze-in scenarios, see [30].

To better understand the process of freeze-in, and to illustrate the differences between the renormalizable and non-renormalizable cases, let us investigate dark matter production by a general $2 \to 2$ process: $a + b \to c + \chi$. Here, χ is the dark matter candidate and a, b, and c are particles in the thermal bath. Let us suppose that this process is mediated by an operator of dimension $4 + \alpha$. For example if all particles are scalars, then $\alpha = 0$ and this is a renormalizable operator. If there are fermions involved, then $\alpha > 0$ and the non-renormalizable operator comes with a suppression of $1/M_*^\alpha$. In both cases, the production

of dark matter will predominantly occur for temperatures greater than the masses of the particles involved, so we may give a rough estimate for the matrix element

$$|\mathcal{M}|^2 \sim \lambda^2 \frac{s^\alpha}{M_*^{2\alpha}}, \tag{3.5}$$

where $\sqrt{s}$ is the center of mass energy (not to be confused with the entropy density).

We now turn to the integrated Boltzmann equation for the number density of χ, given by 2.29. Since we are assuming that χ has a negligible abundance compared to the bath particles, we will set $f_\chi \to 0$ in the collision integral (therefore ignoring the inverse process $c + \chi \to a + b$). With these approximations, the result is a simple one dimensional integral [28, 30]:

$$\dot{n}_\chi + 3Hn_\chi \simeq \frac{T\lambda^2}{512\pi^5 M_*^{2\alpha}} \int_0^\infty \mathrm{d}s\, s^{\alpha+(1/2)}\, K_1(\sqrt{s}/T) = \frac{\alpha!(\alpha+1)!}{2^{7-2\alpha}\pi^5} \left(\frac{T^{\alpha+2}\lambda}{M_*^\alpha}\right)^2. \tag{3.6}$$

In terms of the yield, Y_χ, we have

$$\frac{\mathrm{d}Y_\chi}{\mathrm{d}T} = -\frac{45\,\alpha!\,(\alpha+1)!\,M_{Pl}}{1.66 \times 2^{8-2\alpha}\,\pi^7\,g_{*s}\sqrt{g_*}} \left(\frac{T^{\alpha-1}\lambda}{M_*^\alpha}\right)^2. \tag{3.7}$$

From this relation, we see that for $\alpha > 0$, χ production is dominated at high temperatures, whereas for $\alpha = 0$ it is dominated at low temperatures. Note that in the latter case, production will stop when $T \simeq m_\chi$, assuming that χ is the heaviest particle involved. Therefore we find that the frozen-in value of the yield is

$$Y_\chi \sim \begin{cases} \lambda^2 \left(\dfrac{M_{Pl}}{m_\chi}\right) & \alpha = 0 \\[3mm] \lambda^2 \left(\dfrac{M_{Pl}\,T_{RH}^{2\alpha-1}}{M_*^{2\alpha}}\right) & \alpha > 0 \end{cases}, \tag{3.8}$$

where T_{RH} is the reheat temperature.

Equations 3.7 and 3.8 reveal a general pattern about the freeze-in mechanism. When dark matter interacts via renormalizable operators, the production is dominated at low temperatures (down to m_χ). This is called *IR freeze-in*, as the process is only sensitive to IR physics at temperatures near the dark matter mass. On the other hand, when dark matter freezes in via non-renormalizable operators. the production takes place primarily at high temperatures, just after reheating. This is called *UV freeze-in* [30], since the process is sensitive to UV physics at high temperatures. Note that the reheat temperature cannot be higher than the cutoff scale, otherwise our effective field theory description breaks down.

Figure 3.2 shows the yield of dark matter for the UV and IR freeze-in scenarios throughout the production process.
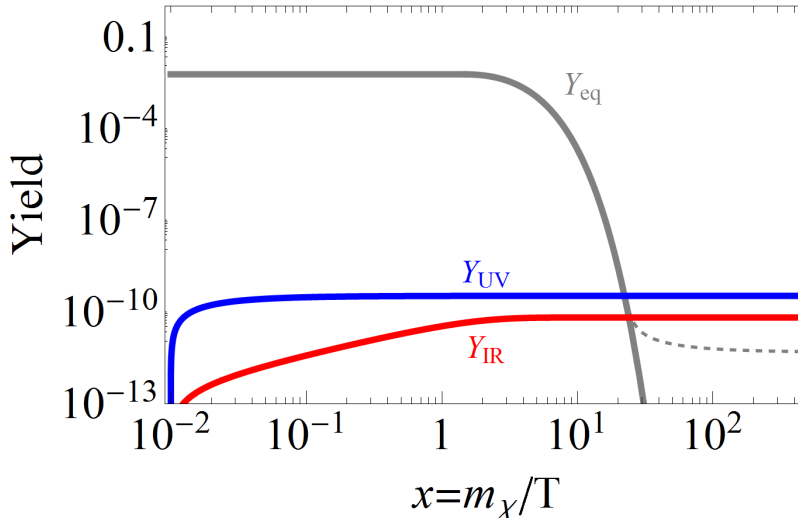

Figure 3.2: Numerical solutions to equation 3.7 for the IR (red) and UV (blue) cases. We have chosen the couplings $\lambda_{\mathrm{UV}} = 1$ and $\lambda_{IR} = 10^{-10}$. We have set $m_\chi = 100$ GeV, $T_{RH} = 10^4$ GeV, and $M_* = 10^{13}$ GeV. For comparison, we also display the equilibrium yield (grey) and freeze-out yield when $\langle \sigma v \rangle = 10^{-3} G_F$ (dashed, grey).

From a model building perspective, both scenarios have their advantages and disadvantages. When describing the IR freeze-in mechanism, we can remain agnostic about UV physics, such as the reheat temperature, which can be anywhere from M_{Pl} to the MeV scale. However, this description typically requires very small dimensionless couplings, which indicates the need for fine-tuning or more complicated model building to justify why $\lambda \ll 1$. UV freeze-in, in contrast, can work quite well with $\mathcal{O}(1)$ couplings. Furthermore, if there are dark or hidden sectors that do not couple with the SM at the renormalizable level, we still expect them to play an important role at high temperatures in the early Universe. As long as our description in terms of an effective field theory is valid, we can invoke the UV freeze-in mechanism to explain how stable particles from these sectors constitute dark matter. Considering that such hidden sectors are a generic prediction of string theory, UV freeze-in is a natural framework for dark matter production.

3.3   Structure Formation

The isotropy of the CMB indicates that the Universe was quite smooth at the time of last scattering. But small density inhomogeneities grew due to gravitational instabilities to form

the galaxies, clusters, and voids we observe today. This growth may have begun as soon as the Universe was mater dominated due to the clustering of dark matter, as in the case of WIMPs. However, pressure from photons prevent inhomogeneities in the baryon density from growing until the matter and radiation decouple. Information about the distribution of matter in the Universe comes from a wide range of observational input, including galaxy maps, gravitational lensing, and the Lyman alpha forest (described in more detail in section 4.2.4)

Perturbations in the matter density, ρ_M, are quantified by their relative deviation from the average density: $\delta\rho_M(\vec{\mathbf{x}})/\bar{\rho}_M$. Often times, these perturbations are characterized by δ_k, the fourier transform of $\delta\rho_M(\vec{\mathbf{x}})/\bar{\rho}_M$, or the power spectrum $|\delta_k|^2$. Note that here, $\vec{\mathbf{x}}$, k, and $\lambda \equiv 2\pi/k$ are comoving coordinates.

In the *linear* regime ($\delta\rho_M/\bar{\rho}_M \lesssim 1$), the physical size of a perturbation grows as the Universe expands: $\lambda_{\text{phys}} = R(t)\lambda$. This size is often characterized by the mass M contained in a sphere of comoving radius $\lambda/2$:

$$M \equiv \frac{\pi}{6}\lambda_{\text{phys}}^3 \bar{\rho}_M \simeq 1.5 \times 10^{11} M_\odot (\Omega_M h^2)\left(\frac{\lambda}{\text{Mpc}}\right)^3 \tag{3.9}$$

[19]. With this definition, the mass of an average galaxy ($\sim 10^{12} M_\odot$) corresponds to a density fluctuation of the size $\lambda_{\text{gal}} \simeq 1.9\,\text{Mpc}\,(\Omega_M h^2)^{-1/3}$; however, the actual size of a galaxy is $\mathcal{O}(\text{kpc})$. This mismatch is caused by the *non-linear* evolution of galactic sized perturbations. Once a fluctuation enters the non-linear regime ($\delta\rho_M/\bar{\rho}_M \gtrsim 1$), it stops expanding with the Universe and becomes a gravitationally bound system.

The evolution of the power spectrum in the linear regime can be well understood analytically. However, solutions for non-linear evolution are difficult to obtain in all but the most symmetric situations. Much progress in this regime has come from N-body simulations of dark matter. Particles in these simulations represent a large group of dark matter particles. They are placed inside a box of comoving dimensions with periodic boundary conditions and evolve according to their gravitational interactions. Their initial distribution is given by the linear power spectrum of a particular cosmological model.

Dark matter candidates are classified by their velocity distribution and *free-streaming length*, the average comoving distance traveled by a dark matter particle. Density perturbations smaller than this free-streaming length are washed out by the particles' motion, and the power spectrum is highly suppressed below this scale. On one extreme, hot dark matter (HDM) has a velocity distribution close to the speed of light and erases structures the size of galaxies. A typical example of HDM are the neutrinos of the SM. On the other extreme, cold dark matter (CDM) is non-relativistic at the time structure formation begins and has a

negligible free-streaming length. Thermally produced WIMPs fall into this category. Warm dark matter (WDM) is somewhere in between hot and cold, with a free-streaming length at the Mpc scale. A sterile neutrino with keV scale mass, produced by oscillations with the SM neutrinos, is an example of WDM and will be explored in greater detail in the next chapter.

In a universe dominated by CDM, structures tend to form hierarchically; small scale perturbations are the first to go non-linear, and cluster to form larger and larger gravitationally bound systems. A universe filled with HDM evolves quite differently. Density fluctuations just larger than the free-streaming length are the first to go non-linear, while all smaller scale perturbations are suppressed. When these large, super-galactic sized structures do go non-linear, they tend to collapse along one dimension and form pancake shaped objects [31]. This type of structure formation is hard to reconcile with the observed density distribution, which significantly restricts the contribution that SM neutrinos make to the matter density of our Universe.

The intermediate case of WDM allows perturbations larger than the free-streaming length to evolve in a similar manner to CDM. The suppression of smaller scale structures has been proposed as a solution for some of the problems matching CDM simulations with observed galaxy clusters. For instance, recent CDM simulations of Milky Way-mass systems predict a large number of massive subhalos that cannot host the observed bright Milky Way satellite galaxies [32, 33]. These massive subhalos have central densities too high, and both maximum circular velocities and infall velocities too large, to host any of the bright Milky Way satellites. The presence of these large subhalos poses a problem for standard CDM models, and is often referred to as the "Too Big to Fail" problem. Using WDM, with a suppressed power spectrum at small scales, the authors of [34] find fewer massive subhalos with large velocity in their N-body simulations, in better agreement with Milky Way satellites.

Chapter 4

Sterile Neutrinos as Dark Matter

Right-handed neutrinos are a well motivated extension of the SM, providing an origin for neutrino masses via the see-saw mechanism. However, unlike every other fermion in the SM, these right-handed chiral states are uncharged under the SU(3)×SU(2)×U(1) gauge group of the SM, and are therefore called *sterile* neutrinos.[1] Their lack of interactions with SM matter makes them a viable dark matter candidate. In this chapter we will explore the possible ways in which sterile neutrinos may be produced in the early Universe, and the associated constraints from astrophysical and cosmological observations. We will see that, unlike the sterile neutrinos of the traditional see-saw mechanism with GUT or Planck scale masses, sterile neutrino dark matter is required to be relatively light (keV-GeV).

4.1 Production Mechanisms

4.1.1 Active-Sterile Oscillations (Dodelson-Widrow Mechanism)

In 1993, Scott Dodelson and Lawrence Widrow demonstrated that oscillations between active and sterile neutrinos can yield a sterile neutrino population abundant enough to comprise all of dark matter [35]. The only interaction at tree level between sterile neutrinos and SM particles is through these oscillations, so, barring any additional physics beyond the SM, such oscillations are generically the primary production mechanism for sterile neutrinos. To model this scenario, Dodelson and Widrow considered a simplified picture where one active neutrino mixes with one sterile neutrino. In this case, the unitary transformation between

---

[1]The term sterile neutrino can be a slight abuse of notation when referring to mass eigenstates. After diagonalizing the neutrino mass matrix, there are mass eigenstates that consist mostly of right-handed neutrinos, but contain a small admixture of the left-handed states. Therefore, these mass eigenstates are *mostly sterile*, but can participate in weak interactions due to this small left-handed component.

the flavor and mass eigenstates is

$$
\begin{aligned}
|\nu_\alpha\rangle &= \cos\theta_m|\nu_1\rangle + \sin\theta_m|\nu_2\rangle \\
|\nu_s\rangle &= -\sin\theta_m|\nu_1\rangle + \cos\theta_m|\nu_2\rangle \,,
\end{aligned}
$$

where $|\nu_\alpha\rangle$ and $|\nu_s\rangle$ are active and sterile flavor eigenstates, respectively, and $|\nu_1\rangle$ and $|\nu_2\rangle$ are mass eigenstates. θ_m is the effective mixing angle, which depends on the matter density and temperature, and is generally different than the vacuum mixing angle θ. When $\theta_m \ll 1$, the mass eigenstate $|\nu_2\rangle$ is mostly sterile and its weak interactions are suppressed by $\sin^2\theta_m$. For the cases of interest here, this suppression is large enough to prevent the sterile neutrino from ever entering thermal equilibrium. Therefore, this production mechanism is quite different than thermal freeze-out. In general, the sterile neutrino population will reach thermal equilibrium if

$$
\sin^4 2\theta\, \Delta m^2 \gtrsim 3 \times 10^{-5}\ \text{eV}^2\,, \tag{4.1}
$$

where Δm^2 is the squared mass difference between the sterile and active neutrino [36].

Dodelson and Widrow analyzed the Boltzmann equations for the sterile neutrino phase space density, while the active neutrinos are in equilibrium ($T \gg \text{MeV}$). They found that production peaks at temperatures $T_{\max} \simeq 133(m_s/\text{keV})^{1/3}$ MeV, where m_s is the mass of the sterile neutrino, and that the distribution of the sterile neutrinos was approximately a thermal one, with an overall suppression. Later, numerical calculations of the sterile neutrino abundance, Ω_s, took into account changes in degrees of freedom during the QCD phase transition, giving roughly

$$
\Omega_s \simeq 0.2 \left(\frac{\sin^2\theta}{3 \times 10^{-9}}\right)\left(\frac{m_s}{3\ \text{keV}}\right)^{1.8} \tag{4.2}
$$

[37, 38, 39, 40, 41]. The Dodelson-Widrow (DW) production mechanism is commonly used in models of sterile neutrino dark matter.

4.1.2 Resonant Oscillations (Shi-Fuller Mechanism)

After Dodelson and Widrow described the oscillations of active to sterile neutrinos, Xiang-dong Shi and George Fuller demonstrated that a lepton asymmetry can induce an MSW resonance[2] in the oscillation $\nu_\alpha \leftrightarrow \nu_s$ ($\alpha = e$, μ or τ) [45]. In this analysis, the authors assume that the lepton asymmetry is almost entirely due to active neutrino asymmetry,

---

[2]Named after L. Wolfenstein, S. P. Mikheev, and A. Smirnov who were the first to point out that neutrino oscillations may undergo a resonance in the presence of matter [42, 43, 44].

and the electron-positron asymmetry is negligible. This lepton asymmetry is quantified as $\mathcal{L} \equiv 2L_{\nu_\alpha} + \sum_{\alpha \neq \beta} L_{\nu_\beta}$, where L_{ν_β} is the asymmetry in the number density of neutrino species ν_β, normalized to the photon density, i.e. $L_{\nu_\beta} \equiv n_{\nu_\beta}/n_\gamma$. The MSW resonance, driven by non-zero $\mathcal{L}$, occurs at a temperature

$$T_{\text{res}} \simeq 9 \left(\frac{m_s}{100 \text{ eV}}\right)^{1/2} \left(\frac{\mathcal{L}}{0.1}\right)^{-1/4} \epsilon^{-1/4} \text{ MeV}, \tag{4.3}$$

where $\epsilon \equiv E/T$. At the same time, the anti-neutrino oscillation $\bar{\nu}_\alpha \leftrightarrow \bar{\nu}_s$ is suppressed. So the overall process sends $\mathcal{L}$ to zero because ν_α is converted to sterile neutrinos, but $\bar{\nu}_\alpha$ is not.

Only active neutrinos that pass adiabatically through this resonance are efficiently converted to sterile ones. From 4.3, we can see that lower energy neutrinos will pass through this resonance first (at higher temperatures), when $\mathcal{L}$ is large. The authors found that these first, low energy neutrinos do satisfy the adiabatic condition, and are resonantly converted to sterile neutrinos. Higher energy neutrinos will pass through resonance later, when $\mathcal{L}$ is suppressed, and the adiabatic condition is no longer satisfied. Therefore the resulting sterile neutrino energy spectrum is non-thermal and colder than in the DW scenario. In this case, the sterile neutrinos will become non-relativistic earlier and have a shorter free streaming length, at or below the dwarf galaxy scale, depending on the lepton asymmetry. This colder dark matter is less restricted by observations of large scale structures, and can avoid the tension between Lyman-α and X-ray bounds (discussed in section 4.2).

The Shi-Fuller mechanism requires a relatively large lepton asymmetry ($\mathcal{L} \sim 10^{-3} - 10^{-1}$) at the time of production compared to the baryon asymmetry ($\sim 10^{-10}$). If such a large lepton asymmetry were produced before the electroweak phase transition, it would be distributed roughly equally between the baryons and leptons by sphaleron processes, which conserve $B - L$ but violate $B + L$. Therefore, the generation of this lepton asymmetry must take place after the electroweak phase transition. For example, oscillations of heavier sterile neutrinos could be the source of the lepton asymmetry driving the resonant production of the lightest sterile neutrino, as is the case in the Neutrino Minimal Standard Model (νMSM) [46, 47, 48].

4.1.3 BSM Alternatives

Introducing new degrees of freedom, beyond the SM, that couple to neutrinos opens up the door for production mechanisms beyond oscillations. Such scenarios do not depend on the mixing with active neutrinos and may easily evade X-ray constraints. Furthermore, it is possible to produce a much colder spectrum and relieve tension with structure formation

constraints. Often, the sterile neutrino is given a feeble coupling to a particle in the thermal bath, and its production proceeds via the freeze-in mechanism (see section 3.2 for a general discussion of this production mechanism). This can be realized in several motivated frameworks; this particle could be the inflaton [49], a heavy higgs in an extended Higgs sector [50, 51, 52, 53, 54, 55, 56], a charged scalar motivated by leptogenesis [57], the radion in warped extra dimension models [58], or pseudo-Dirac neutrinos [59]. For a recent review of various scenarios that admit freeze-in of sterile neutrino dark matter, see Ref. [60]. Chapters 5, 6, and 7 will be devoted to exploring several scenarios where the sterile neutrino is charged under a new symmetry which is broken by a scalar field.

4.2 Astrophysical and Cosmological Constraints

4.2.1 Sterile Neutrino Lifetime

Any candidate for dark matter must be stable on time scales of order the age of the Universe, roughly 13.8 billion years (4.35×10^{17} seconds) [23]. For sterile neutrino dark matter, stability requirements restrict its mass and mixing with the active neutrinos, parameterized by the mixing angle θ. The dominant decay channel for sterile neutrinos lighter than a pion is into three active neutrinos. For heavier sterile neutrinos, two body decay channels into a meson and lepton open up. For a complete list of these decay channels and widths, see the appendix of [61].

The simple requirement that the sterile neutrino live longer than the age of the Universe cuts out a large region of the (m_s, θ) parameter space. The region where these neutrinos decay too quickly is displayed in red in figure 4.1. We also display the relation between the mass and mixing required produce all of dark matter in the DW scenario (no lepton asymmetry) with the black line. Below this line, active-sterile neutrino oscillations produce less than the observed abundance of dark matter. Enhanced production from lepton asymmetry can yield the correct abundance in regions below this line (see, for instance, figure 4 of [62]).

4.2.2 Phase-Space Density

A lower bound on the mass of dark matter particles comes from considering their phase-space densities. A very robust, model independent bound comes from the fact that the average phase-space density of any fermionic system cannot exceed that of a degenerate Fermi gas [63]. Applied to several dwarf spheroidal galaxies, this argument yields the bound

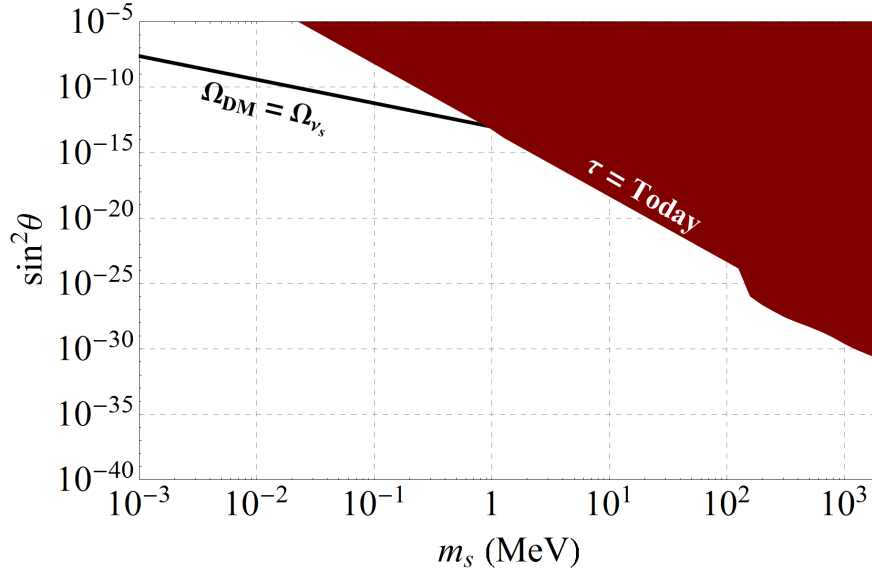$$m_{\mathrm{DM}} > 0.41 \text{ keV} \tag{4.4}$$

Figure 4.1: Lifetime restrictions on the mass and mixing of sterile neutrino dark matter. In the red region, the sterile neutrino lifetime is shorter than the age of the Universe. The black line indicates where all of dark matter is produced by active-sterile oscillation in the DW scenario.

[64]. If the mass individual fermions were smaller, then the pressure from the Pauli exclusion principle would exceed the gravitational force binding the fermions together. More precisely, the maximal Fermi velocity would exceed the escape velocity and the system could not be held together by gravity alone.

For sterile neutrinos produced through the DW mechanism, a tighter bound may be obtained using the fact that these neutrinos have a distribution approximately proportional to a Fermi-Dirac distribution. This yields a bound of

$$m_s \geq 1.77 \text{ keV} \tag{4.5}$$

[64]. Resonant production (Shi-Fuller mechanism) in the presence of lepton asymmetry can weaken this lower bound slightly to about 1 keV.

4.2.3 X-Rays and Gamma-Rays

X-ray and Gamma-ray observations are used to search for the decay lines of dark matter. The keV-10 GeV range has been well measured by several experiments (HEAO-1, INTEGRAL, COMPTEL, EGRET, Fermi LAT). If sterile neutrinos comporise a significant fraction of dark matter, the absence of such a signal constrains the sterile neutrino mass and active-

sterile mixing angle. A sterile neutrino can decay to an active neutrino and photon with width

$$\Gamma_{\nu_s \to \gamma \nu_a} = \frac{9 \, \alpha_{\mathrm{EM}} \, G_F^2}{256 \cdot 4\pi^4} \sin^2(2\theta) m_s^5 \tag{4.6}$$

[65]. Because it is a two body decay and the sterile neutrino decays nearly at rest, we expect $E_\gamma \cong m_s/2$.

Recently, an unidentified X-ray line at approximately 3.5 keV was measured in the stacked X-ray spectra of 73 galaxy clusters by XMM-Newton [16] and in the X-ray spectra of the Andromeda galaxy and the Perseus galaxy cluster [17]. This signal has sparked great excitement in community, as it may be the signature of a decaying sterile neutrino with mass 7 keV. This nature of this signal is still the subject of debate, and is discussed in further detail in chapter 7.

Apart from the possible signal at 3.5 keV, the observed X-ray/Gamma-ray background is well described by active galactic nuclei [66] and there is no detectable deviation in the energy range of sterile neutrino decay. Therefore, the signal from sterile neutrino decay must be on the order of the measurement error. Roughly, this puts an upper bound on the product $\sin^2(2\theta)m_s^5$:

$$\Omega_s \sin^2(2\theta) \left(\frac{m_s}{\mathrm{keV}} \right)^5 < 3 \times 10^{-5}, \tag{4.7}$$

which is independent of the production mechanism and temperature of the dark matter [66].

This approximate bound is displayed in figure 4.2, along with the lifetime bounds discussed in section 4.2.1. The black line displays the relation between the mass and mixing required to produce all of dark matter in the DW scenario (no lepton asymmetry). From this figure, we can see that in the DW scenario, the mass of the sterile neutrino must be less than $\mathcal{O}(10)$ keV.

4.2.4 Lyman-α Forest

The Lyman-α forest is the spectra of absorbtion lines in the radiation from distant ($z \sim 2-4$) quasars due to intervening neutral hydrogen. Analysis of these spectra provides a great deal of information about density fluctuations on scales with comoving wavenumber $k \sim (0.1 - 10)h \, \mathrm{Mpc}^{-1}$, much smaller than the scales that can be probed by CMB analysis [68]. Perturbations in the spectrum opacity indicate fluctuations in neutral hydrogen density, which follow fluctuations in the total matter density. Studying structures of this size is the best way to distinguish between WDM and CDM models. Structure formation evolves in the same way for both theories above a critical scale, typically around a Mpc. At lengths below this critical scale, WDM models suppress the growth of density perturbations.
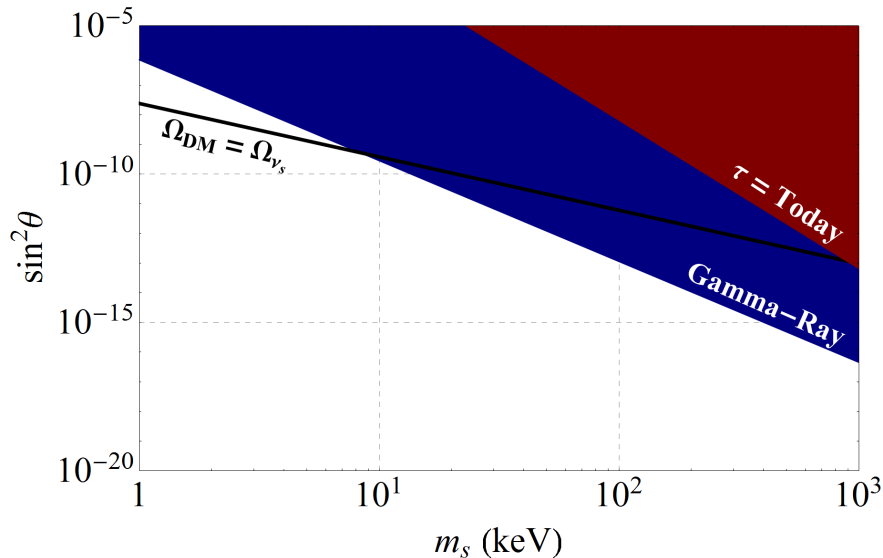
Figure 4.2: Constraints coming from the non-observation of a Gamma/X-ray line. The blue region is ruled out by Gamma/X-ray observation. This is a linear approximation to the bounds presented in [67]. For comparison, we display where the sterile neutrino lifetime is shorter than the age of the Universe in red. The black line indicates where all of dark matter is produced by active-sterile oscillation in the DW scenario.

This scale is given by the free streaming length of the dark matter particles. Lyman-α analysis can put an upper bound on the free streaming length, which corresponds to an upper bound on the average velocity. For a thermal distribution, this upper bound on velocity can be converted to a lower bound on the mass in a straightforward manner, but the non-thermal distribution of sterile neutrinos takes more care.

Using the velocity distribution of non-resonantly produced sterile neutrinos calculated in [38], Seljak et. al. [69] use the power spectrum measured by SDSS to derive a mass bound

$$m_s > 14 \text{ keV at } 95\% \text{ c.l. } (10 \text{ keV at } 99.9\%). \tag{4.8}$$

Looking back at figure 4.2, we can see that this constraint comes into conflict with the upper limits on the mass of the sterile neutrino when it is produced in the DW scenario.

The distribution of resonantly produced sterile neutrinos may be very different than the non-resonant case. In particular, the average velocity can be shifted from the non-resonant and thermal values, which are roughly the same. The lower limit on resonantly produced sterile neutrino mass may be estimated by

$$m_{\text{RP}} \gtrsim \frac{\langle q \rangle_s}{\langle q \rangle_a} m_{\text{NRP}} \tag{4.9}$$

[62], where m_{NRP} is the non-resonant lower mass bound and $\langle q \rangle_a$ and $\langle q \rangle_s$ are the average momenta of the active and sterile neutrinos, respectively. The ratio $\langle q \rangle_s / \langle q \rangle_a$ can be as low as 0.3, and depends on the lepton asymmetry at the time of production (see [62] for details and plots of this ratio for various sterile neutrino masses and lepton asymmetries).

4.2.5 Dark Radiation

For much of its history, the content of the Universe has been dominated by relativistic particles, or radiation. After the QCD phase transition, this radiation consists primarily of photons, neutrinos, and electrons/positrons. Once temperatures drop below the electron mass, annihilation processes like $e^+ + e^- \rightarrow \gamma + \gamma$ still occur rapidly, but the inverse processes which produce electrons/positrons essentially stop, and their number densities become Boltzmann suppressed. After this point, the only relativistic degrees of freedom (in the SM) are photons and neutrinos. Referring back to equation 2.35, and assuming that the neutrinos have a Fermi-Dirac distribution, the radiation energy density is

$$\rho_R = \rho_\gamma \left(1 + \frac{7}{8} \left(\frac{T_\nu}{T} \right)^4 \frac{g_\nu}{g_\gamma} \right) , \tag{4.10}$$

where we have explicitly pulled out the density of the photons, ρ_γ. In the SM, $g_\nu = 6$, accounting for the three active neutrinos. Before electron/positron annihilation, the active neutrinos and photons have the same temperature. However, these neutrinos decouple before the electrons/positrons annihilate. Therefore the photon bath is heated up slightly with respect to the neutrinos after electrons/positrons annihilate, so that

$$\frac{T_\nu}{T} = \left(\frac{4}{11} \right)^{1/3} \quad \text{for } T \ll m_e . \tag{4.11}$$

Any departure from these assumptions above is parameterized by N_{eff}, defined by

$$\rho_R = \rho_\gamma \left(1 + \frac{7}{8} \left(\frac{T_\nu}{T} \right)^4 N_{\mathrm{eff}} \right) . \tag{4.12}$$

This parameter measures the effective number of degrees of freedom that contribute to the radiation energy density, other than photons. It is normalized in such a way that each thermal, relativistic fermion adds 1 to the value of N_{eff}.

The SM predicts a value of $N_{\mathrm{eff}} = 3.046$ after electron/positron annihilation. The small deviation from 3 is due to the fact that the electron/positon annihilation causes a slight shift in the neutrino distribution, so it is not exactly Fermi-Dirac (see [70] for details about this

shift). Any deviation in N_{eff} from this prediction due to physics beyond the SM is denoted ΔN_{eff}.

For historical reasons, N_{eff} is often called the effective number of neutrino species. However, if a heavier particle has a non-thermal distribution, it may contribute to the radiation energy density as well. In particular we will examine the case of an $\mathcal{O}(\text{GeV})$ mass sterile neutrino produced from the late decay of a heavy (PeV scale) scalar. In this case, the sterile neutrino has a significant kinetic energy which can generate a sizable contribution to N_{eff}. In the general case of a massive, non-thermal dark matter candidate, we must be careful to only count the contribution to the radiation energy density, rather than matter. Therefore (following [71]) we subtract away the rest energy when considering such a dark matter candidate so that its contribution to N_{eff} is given by

$$\Delta N_{\text{eff}} = \frac{\rho_{\text{DM}} - n_{\text{DM}} m_{\text{DM}}}{2\rho_{\text{therm}}^{\text{ferm}}}, \tag{4.13}$$

where $\rho_{\text{therm}}^{\text{ferm}}$ is the energy density of a perfectly relativistic fermonic species.

Our knowledge about N_{eff} comes primarily from two important events: Big Bang nucleosynthesis (BBN) and the decoupling of photons to form the CMB. Adding new, relativistic particles to the thermal bath will increase the expansion rate of the Universe, which has observable consequences in both the outcome of BBN and the anisotropies in the CMB.

BBN is the process by which free neutrons and protons bind together to form the nuclei of light elements, primarily ^{2}H, ^{3}He, ^{4}He, ^{7}Li. Before the onset of BBN, the abundance of neutrons and protons is set by equilibrium thermodynamics. The ratio between the neutron and proton abundances is therefore

$$\left(\frac{n}{p}\right) = \exp\left(\frac{-\Delta m}{T}\right), \tag{4.14}$$

while equilibrium is maintained, where $\Delta m = m_n - m_p = 1.29$ MeV. Eventually, weak interactions can no longer keep the neutrons and protons in chemical equilibrium, and this ratio freezes out. Soon after, the photons become cool enough to allow protons and neutrons to bind together to form ^{2}H, which initiates the formation of heavier elements. Most free neutrons that do not decay become bound in ^{4}He, which has the highest binding energy of the light nuclei considered here [19]. Therefore, the final abundance of ^{4}He is quite sensitive to the neutron abundance and hence the temperature at which the neutron to proton ratio freezes out.

Any increase to the Hubble expansion, coming from $\Delta N_{\text{eff}} > 0$, will cause the neutron to proton ratio to freeze out earlier, leader to more neutrons and therefore more ^{4}He. Measure-

ments of the ^{4}He abundance today provide one of the best constraints on ΔN_{eff} at the time of BBN; however, there are still significant systematic and statistical uncertainties in these measurements. Recent estimates of the primordial ^{4}He abundance constrain $\Delta N_{\text{eff}}^{\text{BBN}} < 0.95$ at 95% C.L. [72], while measurements of the ^{2}H abundance restrict $\Delta N_{\text{eff}}^{\text{BBN}} < 0.85$ at 95% C.L. [73].

Measurements of the CMB anisotropies may also be used to constrain N_{eff}. The standard six parameter ΛCDM cosmology may be extended by taking N_{eff} as a free parameter and fitting this model to observations. Changing the radiation energy density at the time of photon decoupling can have a number of different effects on the CMB, some of which may be compensated by adjusting other parameters. The primary impact of raising N_{eff} is to increase the ratio of the Silk damping scale (set by the photon diffusion length) to the sound horizon, which results in a reduction of small scale anisotropies [74]. In their latest release, the Planck collaboration has restricted $\Delta N_{\text{eff}}^{\text{CMB}} < 0.32$ at 95% C.L. [23]. Although this appears to be a more stringent constraint than those derived from BBN, photon decoupling occurs at temperatures of roughly 0.3 eV, much colder than the onset of BBN at around 4 MeV. We find that in every scenario of frozen-in sterile neutrino dark matter (discussed in chapter 6), the constraints from BBN are more restrictive.

4.3 Summary and Discussion

In the chapter, we have examined several ways in which sterile neutrinos may be produced in enough abundance to comprise dark matter. Active-sterile oscillations will always yield some population of sterile neutrinos in the early Universe whenever there is a non-zero mixing between the the two. With a sizable lepton asymmetry, an MSW resonance can amplify the production of sterile neutrinos, and yield a colder momentum distribution than what is expected for a thermal species.

If sterile neutrinos are to comprise dark matter, several astrophysical and cosmological observables restrict their mass and mixing with the active neutrino sector. The non-observation of an X-ray/gamma-ray line, which is expected from the decay of the sterile neutrino, and restrictions on the free-streaming length coming from examinations of the Lyman-α forest now exclude the potential for sterile neutrinos, produced in the DW scenario, to comprise all of dark matter.

If a large enough lepton asymmetry is present at the time of dark matter production, a smaller mixing angle is needed to produce the required abundance of sterile neutrinos, thereby alleviating constraints from X-ray/gamma-ray observations. Furthermore, since the sterile neutrinos are cooler in this case, the lower limit on the mass coming from the Lyman-α
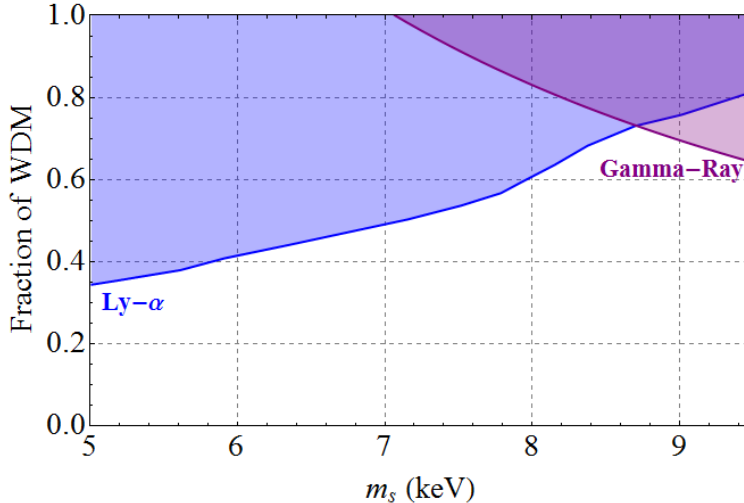
Figure 4.3: X-ray bounds from [66], adjusted for $F_{\mathrm{WDM}} < 1$, and Lyman-α bounds from [68] at the 95% confidence level. The shaded regions are ruled out. The sterile neutrinos are assumed to be produced in the DW scenario.

forest is also reduced (equation 4.9). Indeed, with a large enough lepton asymmetry, active-sterile oscillations may produce all of dark matter, as in the Shi-Fuller scenario. Such a lepton asymmetry can be generated by CP-violating oscillations of the two heavier sterile neutrinos [75, 76]. This self-contained model, often called the Neutrino Minimal Standard Model (νMSM), adds three sterile neutrinos to matter content of the SM. However, to achieve the required lepton asymmetry, a fine-tuning of the order of 1 in 10^{11} in the mass difference between the two heavier sterile neutrinos is required.

Another way to avoid the conflict between X-ray/gamma-ray bounds and considerations from structure formation is to reduce the fraction of dark matter which sterile neutrinos comprise. Taking the remaining fraction of dark matter to be cold can significantly reduce the mass limits from the Lyman-α forest. This case of mixed warm and cold dark matter was examined in [68]. The authors found lower mass limits for sterile neutrinos when they comprise some fraction, F_{WDM} of dark matter. These limits are displayed in figure 4.3, along with the X-ray/gamma-ray constraints (from equation 4.7), re-scaled for $F_{\mathrm{WDM}} < 1$. The unshaded regions indicate where sterile neutrinos, produced in the DW framework, may comprise a fraction of dark matter.

Although sterile neutrinos in the DW scenario may not compose all of dark matter, there are several alternatives that lead to a consistent model. In chapter 6, we will examine the case of a heavy (PeV mass) scalar leading to the freeze-in of sterile neutrinos, and find a range of possibilities that correspond to cold or warm dark matter, that are consistent with all existing constraints.

Chapter 5

Sterile Neutrino Dark Matter from the PeV Scale

In this chapter (based on [13]), we examine whether the active neutrino sector and a sterile neutrino dark matter candidate can emerge naturally from the (supersymmetric) PeV scale. We take the PeV scale to emerge from supersymmetry breaking. There exist compelling arguments for supersymmetry at such high scales from flavor, CP, and unification considerations [9, 10, 11, 12]. High scale SUSY is now further motivated by null results at numerous indirect and direct detection experiments and the first run of the LHC. The measured Higgs boson mass, $m_h = 125$ GeV, also serves an indication of supersymmetry at the PeV scale. The Higgs mass at one loop with no sfermion mixing in the MSSM is

$$m_h^2 \approx m_Z^2 \cos^2 2\beta + \frac{3m_t^4}{4\pi^2 v^2} \ln(m_{\tilde{t}}^2/m_t^2). \tag{5.1}$$

For $\tan\beta \approx \mathcal{O}(1)$, the observed Higgs mass is obtained for sfermion masses at $1-100$ PeV [6, 7, 8]. Since neutrino masses require physics beyond the SM, a common origin of the Higgs mass, dark matter, and neutrino masses is an extremely attractive prospect.

The traditional explanation of active neutrino masses is a see-saw mechanism, involving right-handed, SM-singlet sterile neutrinos N_i that enable the following terms in the Lagrangian

$$\mathcal{L} \supset y_{\alpha i}\bar{L}_\alpha H_u^\dagger N_i + M_i \bar{N}_i^c N_i. \tag{5.2}$$

The first term leads to a Dirac mass between the left- and right-handed neutrinos once H_u obtains a vacuum expectation value (vev), and the second term is a Majorana mass for the sterile neutrinos. If $M \gg y\langle H_u \rangle$, the see-saw mechanism gives active neutrino masses at $(y\langle H_u \rangle)^2/M$. GUT scale see-saw models [77, 78, 79, 80, 81] employ $y \sim \mathcal{O}(1)$

and $M \sim 10^{10} - 10^{15}$ GeV, which can explain the small active neutrino masses but not dark matter. The low energy counterpart, with all masses below the electroweak scale, has been extensively studied in the effective framework of the νMSM [46, 47, 48], where a keV scale sterile neutrino is a viable warm or cold dark matter candidate (see also [82]). However, the keV scale is picked by hand, and producing appropriate active neutrino masses requires $y^2 \lesssim 10^{-13}$. The purpose of this chapter is to explore a modified setup where both active neutrino masses and a dark matter candidate can be realized with predominantly $\mathcal{O}(1)$ couplings and the PeV scale, which is motivated by the Higgs mass measurement as a possible scale for new physics (supersymmetry).

Finally, some recent observational hints add further relevance to this study. A 7 keV sterile neutrino dark matter candidate can explain the recent observation of a monochromatic line signal at 3.5 keV in the X-ray spectrum of galactic clusters [16]. The observation of neutrinos with PeV scale energies at IceCube [83, 47] also hint at a possible connection between the neutrino sector and physics at the PeV scale. These can be accommodated in our framework, but are not necessary ingredients, and therefore will be studied in chapter 7.

5.1 The Model

As in the νMSM, the neutrino sector is extended by three right-handed sterile neutrinos N_i. Our starting point is the observation that although the N_i are uncharged under the SM gauge group, it is unlikely that they are uncharged under all symmetries of nature (as is traditionally assumed in the see-saw mechanism) if they are to be at the keV-GeV scale, otherwise their masses, unprotected by any symmetry, should naturally be at the Planck or GUT scale. Here we invoke a symmetry to suppress the Majorana masses, but it is worth noting that small Majorana masses can also be technically natural if there are no other sources of lepton number violation. For concreteness, assume that the N_i are charged under a $U(1)'$, which are ubiquitous in string-inspired models of nature. This immediately forbids the terms in equation 5.2, and the traditional see-saw mechanism does not work. Higher dimensional operators involving the SM and N_i fields can be obtained by coupling the N_i to other fields charged under the $U(1)'$. We introduce an exotic field ϕ that carries the opposite charge under $U(1)'$.

As motivated in the previous section, we are interested in a supersymmetric framework, motivated by a possible common origin of the supersymmetry breaking scale and the mass scale that sets the neutrino masses (however, this connection to supersymmetry is by no means necessary). We thus introduce three chiral supermultiplets $\mathcal{N}_i$ for the sterile neutrinos and a chiral supermultiplet Φ, whose spin $(0, 1/2)$ components are labeled $(\tilde{N}_i, N_i)$ and (ϕ, ψ_ϕ)

respectively. With these fields and charge assignments, one is allowed the following higher dimensional operators in the superpotential:

$$W \supset \frac{y}{M_*} L H_u \mathcal{N} \Phi + \frac{x}{M_*} \mathcal{N} \mathcal{N} \Phi \Phi. \tag{5.3}$$

Here x and y are dimensionless $\mathcal{O}(1)$ couplings (neglecting possible flavor structure for now), and M_* is the scale at which this effective theory needs to be UV completed with new physics, such as the scale of grand unification M_{GUT} or the Planck scale M_P. Here we have ignored the $(LH_u)^2/M_*$ term, which is of the same dimension, as it is not large enough to produce all active neutrino masses, but we note that it can provide the dominant contribution to the lightest active neutrino mass.

If the scalar ϕ obtains a vev at the PeV scale, presumably from the same mechanism that breaks supersymmetry, this breaks the $U(1)'$ and (after H_u also acquires a vev) leads to the following active-sterile Dirac mass and sterile Majorana mass scales

$$m_D = \frac{y \langle \phi \rangle \langle H_u^0 \rangle}{M_*}, \qquad m_M = \frac{x \langle \phi \rangle^2}{M_*}. \tag{5.4}$$

This results in a modified see-saw mechanism, arising entirely from higher dimensional operators. Below the electroweak scale, the effective theory maps onto the νMSM with the following sterile and active neutrino mass scales:

$$\begin{aligned} m_s &= m_M = \frac{x \langle \phi \rangle^2}{M_*}, \\ m_a &= \frac{m_D^2}{m_M} = \frac{y^2 \langle H_u^0 \rangle^2}{x M_*}. \end{aligned} \tag{5.5}$$

Note that the two scales are related as

$$m_s = \frac{1}{m_a} \left(\frac{y \langle \phi \rangle \langle H_u^0 \rangle}{M_*} \right)^2. \tag{5.6}$$

Fixing the parameters of the theory also determines the mixing angle between the active and sterile sectors:

$$\theta \approx \sqrt{\frac{m_a}{m_s}} = \frac{y \langle H_u^0 \rangle}{x \langle \phi \rangle}. \tag{5.7}$$

Figure 5.1 shows possible active-sterile mass scale combinations that result from this framework with $M_* = M_{GUT} (= 10^{16} \, \text{GeV})$, $\tan \beta = 2$ (corresponding to $\langle H_u^0 \rangle = 155.6$ GeV), and $0.001 < x < 2$ for various values of $y \langle \phi \rangle$. This exercise suggests that both an active neutrino mass scale of $\sqrt{2.3 \times 10^{-3} \, \text{eV}^2} \sim 0.05$ eV, necessary for consistency with
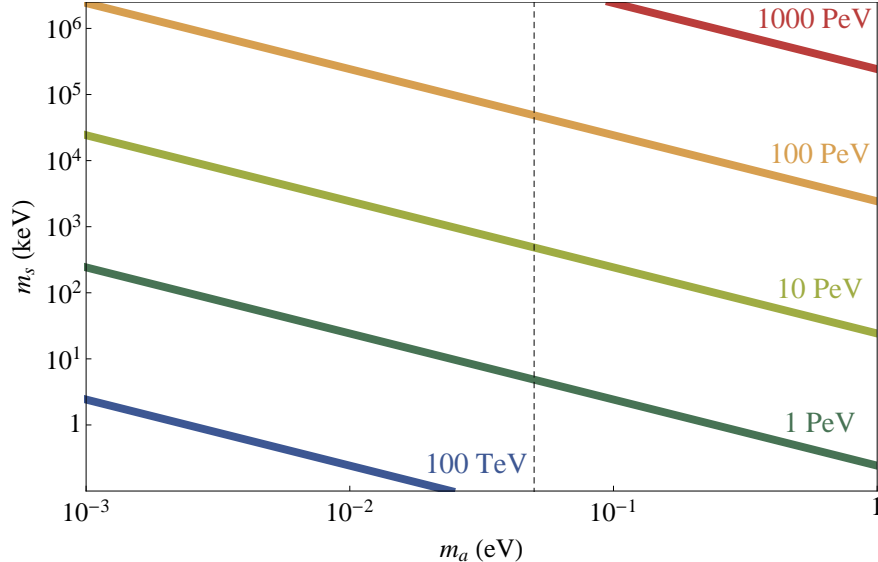
Figure 5.1: Active and sterile neutrino mass scales for various choices of $y\langle\phi\rangle$, with $M_* = M_{GUT}$, $\tan\beta = 2$ ($\langle H_u^0\rangle = 155.6$ GeV), and $0.001 < x < 2$. The dashed vertical line at $m_a = 0.05$ eV is the active neutrino mass scale necessary for consistency with atmospheric oscillation data $\Delta m_{atm}^2 = 2.3 \times 10^{-3}$ eV^2.

atmospheric oscillation data $\Delta m_{atm}^2 = 2.3 \times 10^{-3}$ eV^2, and a sterile neutrino mass scale of $\mathcal{O}$(keV-GeV), necessary for consistency with dark matter and cosmological observations, can emerge naturally in this framework (see [84, 85] for similar frameworks that lead to weak scale sterile neutrinos and sneutrino dark matter, see also [86]).

5.2 Production of Dark Matter

We denote the sterile neutrino dark matter candidate by N_1. As N_1 couples extremely weakly to the SM fields and is never in thermal equilibrium in the early Universe (we have assumed that possible additional interactions due to the $U(1)'$ are negligible), its relic abundance is not set by thermal freeze-out. Under various conditions, our framework allows multiple production mechanisms for N_1.

Sterile neutrino dark matter is constrained by several cosmological and direct observations, which require careful treatment. This section includes a brief overview of these constraints to demonstrate the viability of this dark matter candidate. Details of the relevant astrophysical and cosmological constraints are reviewed in chapter 4, and examined in more detail for this particular framework in chapter 6.

5.2.1 Active-sterile mixing

Production through active-sterile oscillation at low temperatures, known as the DW mechanism [35], is an inevitable consequence of mixing with the active neutrinos, and is known to produce warm dark matter with relic density approximately [35, 37, 38, 39, 40, 41]

$$\Omega_{N_i} \sim 0.2 \left(\frac{\sin^2\theta}{3 \times 10^{-9}} \right) \left(\frac{m_s}{3 \text{ keV}} \right)^{1.8}. \tag{5.8}$$

For further details of this production mechanism, see 4.1.1.

Compared to WIMP-motivated cold dark matter (CDM) models, a warm dark matter component might be favorable for a resolution of recent puzzles such as the core vs. cusp problem and the "too big to fail" problem [33, 34]. See section 3.3 for an extended discussion of warm dark matter and its impact on structure formation in the Universe.

The most stringent constraint on sterile neutrinos comes from X-ray measurements (see section 4.2.3), since a sterile neutrino can decay into an active neutrino and a photon. The decay width for this process is

$$\Gamma(\nu_s \to \gamma\nu_a) = \frac{9\alpha_{EM}G_F^2}{1024\pi^4} \sin^2(2\theta)m_s^5. \tag{5.9}$$

A combination of X-ray bounds [66, 87, 88, 89, 90] and Lyman-alpha forest data [41, 68, 69] now rule out the prospect of all of dark matter consisting of N_1 produced in this manner. However, as discussed in section 4.3, N_1 produced through the DW mechanism can still constitute a significant fraction of the dark matter abundance. For instance, an analysis in [68] showed that $m_s \geq 5$ keV warm component constituting $\leq 60\%$ of the total dark matter abundance is consistent with all existing constraints [91]. A follow-up study by the same authors [92] and a more recent study [93] are also in approximate agreement with these numbers.

5.2.2 Freeze-In from ϕ

If the scalar ϕ has additional interactions (with the Higgs or supersymmetric sector, for example) that keep it in equilibrium with the thermal bath at high temperatures, additional freeze-in production mechanisms can contribute to the present abundance of N_1. Here we present an overview of these production modes. We emphasize that the formulae below for IR and UV freeze-in are only approximate, and several $\mathcal{O}(1)$ effects have been ignored. For instance, the dilution of N_1 abundance due to entropy production from the decay of other sterile neutrinos [48] has not been accounted for. A more detailed study of these cases will

be presented in chapter 6.

IR Freeze-In

Once the scalar field obtains a vev $\langle\phi\rangle$, the decay channels $\phi \to N_1 N_1$ and $H_u \to N_1\nu_a$ open up with effective couplings $x_1 = \frac{2x\langle\phi\rangle}{M_*}$ and $y_1 = \frac{y\langle\phi\rangle}{M_*}$ respectively, resulting in the accumulation of N_1 through the freeze-in mechanism [28, 51, 54] until the temperature drops below the mass of the parent particle(s). Assuming $y < x$, the abundance due to $\phi \to N_1 N_1$ is [51, 50]

$$\Omega_{N_1} h^2 \sim 0.1 \left(\frac{x_1}{1.4 \times 10^{-8}}\right)^3 \left(\frac{\langle\phi\rangle}{m_\phi}\right). \tag{5.10}$$

For $\langle\phi\rangle/m_\phi \sim \mathcal{O}(1)$, $x \sim 1$, and $\langle\phi\rangle \sim 1 - 100$ PeV, this can be a significant contribution to the dark matter abundance. Indeed, IR freeze-in through decay of heavy particles is a widely used production mechanism for sterile neutrino dark matter [49, 50, 51, 54, 56, 57, 59, 71, 94, 95, 96].

UV Freeze-In

High temperatures in the early Universe can also overcome the $1/M_*$ suppression of non-renormalizable interactions from the terms in equation 5.3. Dark matter can then be produced through the annihilation processes $\phi\phi \to N_1 N_1$, $\phi H_u \to \nu_a N_1$, $\phi\nu_a \to H_u N_1$, and $H_u\nu_a \to \phi N_1$. Assuming $x > y$, so that $\phi\phi \to N_1 N_1$ gives the dominant contribution, the dark matter yield and relic density are approximately [30, 97, 98, 99, 100]

$$Y_{N_1} \quad \sim \quad 5 \times 10^{-7} x^2 \left(\frac{T_{RH} M_P}{M_*^2}\right), \tag{5.11}$$

$$\Omega_{N_1} h^2 \quad \simeq \quad 0.1\, x^2 \left(\frac{m_s}{10\,\text{GeV}}\right) \left(\frac{T_{RH} M_P}{M_*^2}\right). \tag{5.12}$$

If the reheat temperature T_{RH} is sufficiently high, this contribution can also be significant. This UV freeze-in contribution is generally not considered in the νMSM or its singlet extensions and is a novel feature of our use of non-renormalizable operators.

ϕ Out of Equilibrium

So far, we have relied on a thermal abundance of ϕ from which to produce dark matter, which we took to be a plausible scenario. However, even when ϕ has no additional interactions that keep it in equilibrium with the thermal bath, so that there is no initial abundance of ϕ, freeze-in can still provide the desired dark matter abundance.

This can occur provided an abundance of ϕ gradually builds up from the annihilation process $H_u \nu_i \to \phi N_j$ if the temperature in the early Universe is sufficiently high to overcome the $1/M_*$ suppression. Note that this process cannot directly produce a large abundance of the dark matter candidate N_1 since the y_{i1} couplings corresponding to $H_u \nu_i \to \phi N_1$ are required to be extremely small in order to prevent large mixing between N_1 and the active neutrinos (which would make N_1 short-lived). However, y_{i2}, y_{i3} can be $\mathcal{O}(1)$, so an abundance of ϕ can be built up. The crucial difference here compared to the equilibrium case is that, given the absence of significant couplings to the particles in the thermal bath, ϕ decays dominantly into sterile neutrinos. Hence the entire ϕ abundance is converted into sterile neutrinos, with branching fractions proportional to the sterile neutrino masses. The relic abundance of N_1 that results from this process is estimated to be

$$\Omega_{N_1} h^2 \sim 0.1 \sum_{i,j} y_{ij}^2 \left(\frac{m_s}{\text{GeV}}\right) \left(\frac{1000\, T_{RH}\, M_P}{M_*^2}\right) Br(\phi \to N_1 N_1) \tag{5.13}$$

Hence, with a high enough reheat temperature T_{RH}, one can obtain the correct dark matter abundance even when ϕ does not have any significant additional interactions. In chapter 6 we will study the details of this scenario in both supersymmetric and non-supersymmetric frameworks.

5.2.3 Parameter Space of N_1

Figure 5.2 explores the various masses and mixing angles for N_1 for which the correct relic density can be obtained (resonant production has been ignored, and T_{RH} is assumed to be sufficiently low that UV freeze-in is negligible). The light blue shaded regions represent parameter space where $10^{-3} \leq \Omega h^2 \leq 0.12$; two distinct regions occur, corresponding to two distinct production mechanisms. In the top left region, dark matter is produced through the DW mechanism thanks to significant active sterile mixing $\sin^2\theta \sim 10^{-10}$ for $m_s \sim 1-10\,\text{keV}$. In the bottom right region (plotted for $\langle\phi\rangle = m_\phi = 100\,\text{PeV}$), N_1 is produced via IR freeze-in of ϕ, where the extremely small mixing angle $\sin^2\theta \sim 10^{-38}$ prevents N_1 from decaying into SM fields and keeps it safe from gamma-ray constraints [67].

We note parenthetically that since the connection to the PeV scale was inspired by considerations of a supersymmetric sector, a stable or sufficiently long-lived superpartner can also account for an $\mathcal{O}(1)$ (cold) fraction of dark matter, as could axions.
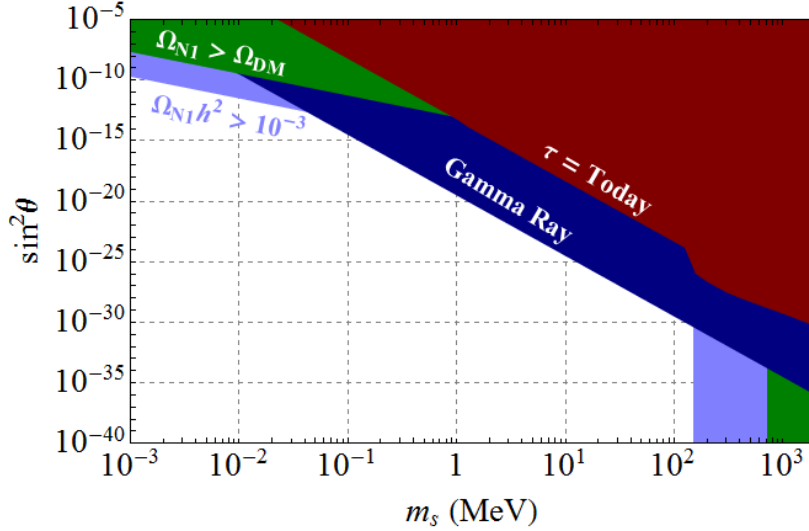
Figure 5.2: Sterile neutrino dark matter parameter space. In the red region, the lifetime, calculated using several decay channels following [101], is shorter than the age of the Universe. Dark matter overcloses the Universe in the green region. Dark blue denotes the approximate region ruled out by X-ray and gamma-ray constraints, assuming that N_1 composes all of dark matter. The light blue shaded regions consist of parameter space where $10^{-3} \leq \Omega h^2 \leq 0.12$: the top left region corresponds to DW production, while the bottom right corresponds to IR freeze-in ($M_* = M_{GUT} = 10^{16}$ GeV and $\langle \phi \rangle = m_\phi = 100$ PeV everywhere in the plot).

5.3 Heavier Sterile Neutrinos $N_{2,3}$

The neutrino sector of the theory also contains two other sterile neutrinos N_2 and N_3. As in the νMSM, these mix with the two heavier active neutrinos to produce their masses. In contrast, the dark matter candidate N_1 cannot fully participate in the see-saw as various constraints (see figure 5.2) force a suppression of its mixing with the active neutrinos, leaving the lightest active neutrino essentially massless. These generic features of the νMSM are also present in our framework.

The decays of N_2, N_3 are constrained by several recombination era observables [37, 102, 103, 103], hence they are generally required to decay before BBN, which forces $\tau_{N2,N3} \lesssim 1$s and consequently $m_{N2,N3} \gtrsim \mathcal{O}(100)$ MeV.

Several direct searches for heavy neutral leptons with significant mixing with the SM also place bounds on their lifetimes. These experiments look for sterile neutrino production in the decay of charged mesons by detecting additional peaks in the charged lepton spectrum or the charged decay products of the sterile neutrinos [104, 105, 106, 107, 108, 109].

These BBN and direct search constrained regions are shown in Figure 5.3 as red and cyan regions respectively. To be consistent with direct searches and decay before the onset
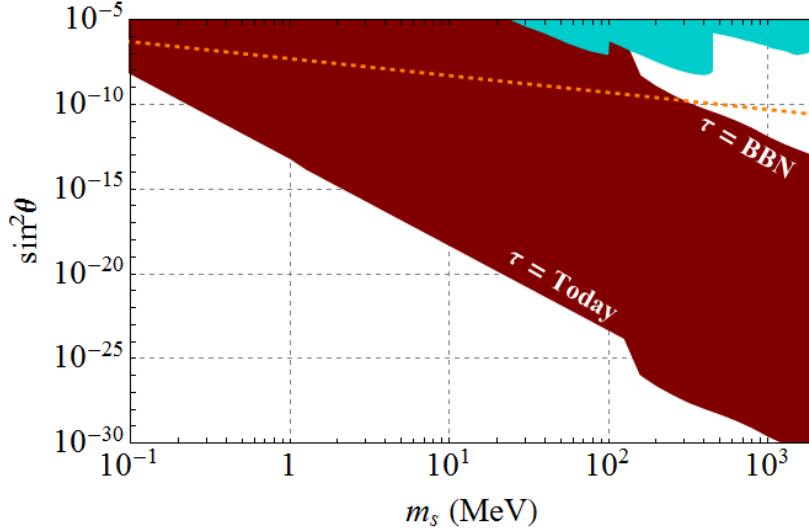
Figure 5.3: Parameter space for the heavier sterile neutrinos $N_{2,3}$. The orange dotted line denotes the combination that yields $m_a \sim 0.05$ eV. In the red region, the lifetime, calculated using several decay channels following [101], is shorter than the age of the Universe but longer than $\tau_{BBN} = 1\,\mathrm{s}$. Cyan regions in top right are constraints from direct searches for heavy neutral leptons.

of BBN, the heavier sterile neutrinos must live in white region on the upper right. The see-saw mechanism imposes a relationship between the mass and mixing of these sterile neutrinos if they are to produce the correct mass scale for the active neutrinos, denoted by the orange dashed line. For the direct search bounds, the two bumps on the left are derived from results from the PS191 experiment [106], while the third bump is derived from results from the NuTeV experiment [109], and we have simply replotted the bounds on mixing angles from plots in the corresponding papers.

5.4 Benchmark Scenarios

As proof of principle, this section presents two benchmark scenarios in our framework that produce active neutrino masses as well as a sterile neutrino dark matter candidate. We have used the Casas-Ibarra parameterization [110] with a normal hierarchy of active neutrino masses to verify that the measured mass differences and mixing angles of the PMNS matrix can be reproduced.

Restoring the full flavor structure, the neutrino mass matrix is a 6×6 entity, with x and y in equation 5.3 now promoted to 3×3 matrices $\mathbf{X}$ and $\mathbf{Y}$. The neutrino mass matrix reads

$$M_\nu = \begin{pmatrix} 0 & \frac{\langle\phi\rangle\langle H_u^0\rangle}{M_*}\mathbf{Y} \\ \frac{\langle\phi\rangle\langle H_u^0\rangle}{M_*}\mathbf{Y}^\dagger & \frac{\langle\phi\rangle^2}{M_*}\mathbf{X} \end{pmatrix}. \tag{5.14}$$

The N_i basis can be chosen such that $\mathbf{X}$ is diagonal. Both benchmarks use $M_* = M_{GUT} = 10^{16}$ GeV and $\tan\beta = 2$, corresponding to $\langle H_u^0\rangle = 155.63$ GeV.

5.4.1 Benchmark A

$\langle\phi\rangle$	$\mathbf{Y}$			diag $(\mathbf{X})$	m_a (eV)	m_s	$\Omega_s h^2$
79.4 PeV	-1.70	-0.20	9×10^{-5}	1.91	0.049	1.2 GeV	
	1.49	-3.96	-3×10^{-5}	1.58	0.0087	1.0 GeV	0.058
	3.91	-2.21	5×10^{-5}	1.3×10^{-5}	2.4×10^{-6}	8.5 keV	

Table 5.1: Parameters for benchmark A

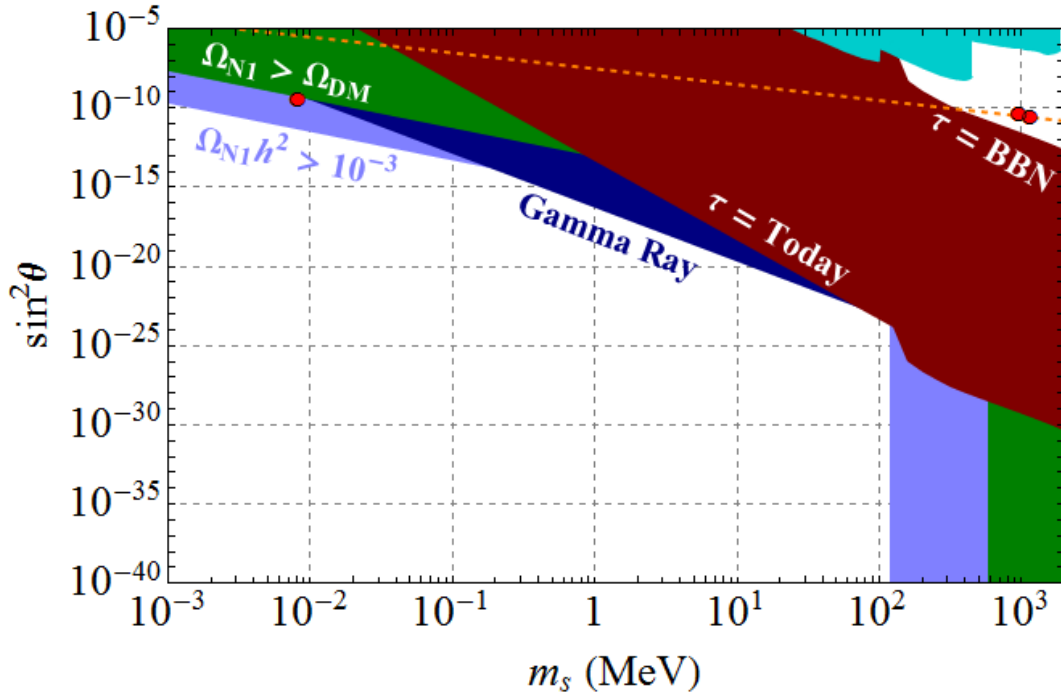Figure 5.4: Red dots correspond to the sterile neutrinos in benchmark A. The various constrains are the same as those in Figures 5.2 and 5.3, except that the gamma-ray bounds here assume that the abundance of N_1 is set by the DW mechanism.

This scenario has a warm dark matter candidate with mass 8.5 keV, with DW production giving 53% of the observed dark matter abundance. Note that since $x \approx 10^{-5}$, both IR and

UV freeze-in are ineffective, but a particle from the supersymmetric sector or the axion could account for the remaining dark matter abundance. The two heavier steriles are at 1 GeV and decay before BBN; the three steriles are plotted as red dots in Figure 5.4. The hierarchy of five orders of magnitude in the entries of $\mathbf{X}$ is necessitated by the hierarchy between the keV mass of the dark matter candidate and the GeV scale mass of the heavier steriles, which need to be heavy enough to decay before BBN. The entries of $\mathbf{Y}$ contain a similar hierarchy to ensure that the dark matter candidate does not mix excessively with the active sector. While a coupling of $\mathcal{O}(10^{-5})$ appears unnatural, such a small coupling already appears in nature in the form of the electron Yukawa, and is therefore perhaps not unrealistic. The lightest active neutrino is essentially massless, as is characteristic in the νMSM with a keV scale sterile neutrino dark matter candidate.

5.4.2   Benchmark B

$\langle \phi \rangle$	$\mathbf{Y}$			$\mathrm{diag}\,(\,\mathbf{X}\,)$	m_a (eV)	m_s	$\Omega_s h^2$
85.1 PeV	$\begin{pmatrix} -1.31 & 0.73 & \sim 0 \\ -1.25 & -3.71 & \sim 0 \\ 1.45 & -3.65 & \sim 0 \end{pmatrix}$			1.46 1.38 0.85	0.049 0.0087 ~ 0	1.1 GeV 1.0 GeV 617 MeV	0.11

Table 5.2: Parameters for benchmark B

This scenario allows for the scalar ϕ to be either in or out of equilibrium with the thermal bath; we consider both cases, and the parameters listed in the table above apply to both. If ϕ has additional interactions that keep it in equilibrium with the thermal bath in the early Universe, the dark matter relic density is insensitive to the temperature of the early Universe (as long as it is high enough to produce ϕ) and is achieved through (IR) freeze-in. Otherwise, an abundance of ϕ has to be built up from UV freeze-in as discussed in the previous section, which requires a high reheat temperature, and its decays produce an abundance of N_1. In this case, once the remaining parameters are specified, the temperature T_{RH} can be appropriately chosen to yield the correct abundance of dark matter. For the parameters listed for Benchmark B, the temperature required is $T_{RH} \approx 10^9$ GeV.

In contrast to Benchmark A, all entries in $\mathbf{X}$ are $\mathcal{O}(1)$, and all sterile neutrinos have ~ 1 GeV mass (represented by blue squares in Figure 5.5). In order to make the dark matter candidate sufficiently long-lived and evade gamma-ray constraints [67], its mixing with the active neutrinos must be suppressed to essentially zero, reflected in the third column of $\mathbf{Y}$.
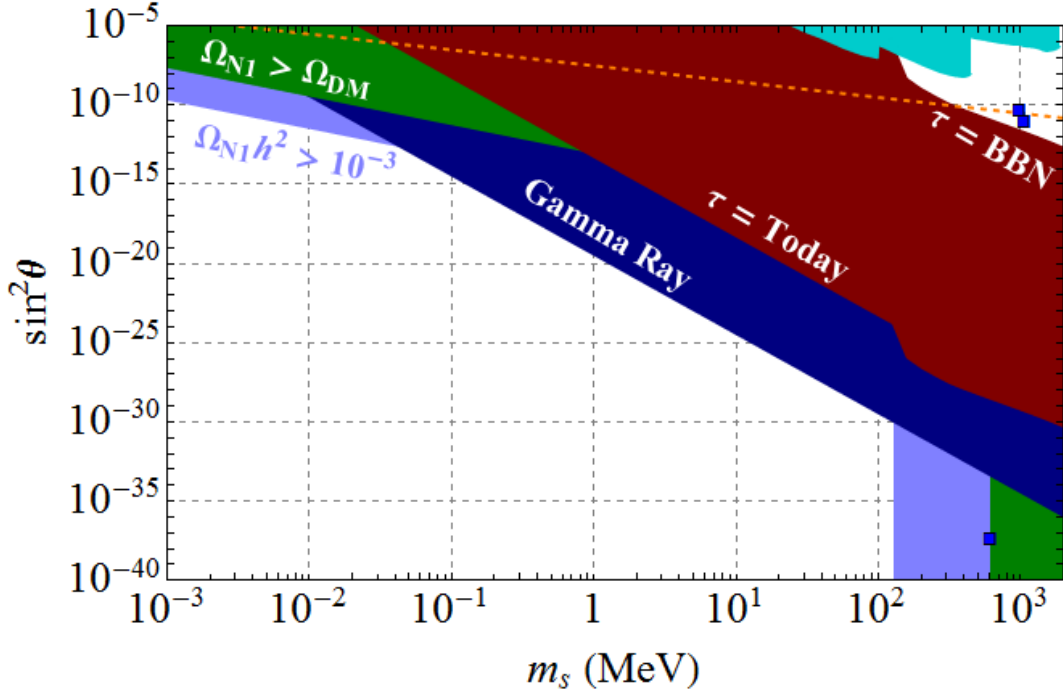
Figure 5.5: Blue squares correspond to the sterile neutrinos in benchmark B. The various constrains are the same as those in Figures 5.2 and 5.3.

While this appears unnatural, note that it is admissible to set these numbers to exactly zero, hence this structure could be invoked due to an underlying symmetry, rendering it technically natural. Such considerations are only necessary if we insist on promoting N_1 to a long-lived dark matter candidate; otherwise, $\mathcal{O}(1)$ couplings are allowed.

5.5 Summary

We have presented a new framework that constitutes a realistic description of active neutrino masses and keV-GeV scale sterile neutrino dark matter emerging naturally from new physics at the PeV scale, which maps on to the widely studied νMSM at low energies. Depending on the parameters chosen, we find two general possibilities for our dark matter candidate N_1 (which are represented by two benchmark cases):

Case	Benchmark A	Benchmark B
Features	$\mathcal{O}(10)$ keV sterile neutrino	$\mathcal{O}(1)$ GeV sterile neutrino
	Produced by active-sterile mixing	Produced by ϕ decay
	Warm DM	Cold or Warm DM
	$\lesssim 60\%$ of DM	100% of DM
		No mixing with active neutrinos

In the case represented by benchmark A, constraints on this type of sterile neutrino dark matter have been well studied (see section 4.2 for a review and the references therein). In chapter 6 we examine the details of the case represented by benchmark B, taking extra care to examine the impact on structure formation and the energy density of the Universe.

Chapter 6

Cosmological Imprints of Frozen-In Sterile Neutrinos

A sterile neutrino is a well-motivated and widely studied dark matter candidate. The traditional candidate, studied within the νMSM [46, 47, 41], has a keV scale mass, where its mixing with the active neutrinos is appropriate for both producing the correct (warm) dark matter relic abundance through the DW mechanism [35] and making it sufficiently long lived. However, this nonzero mixing also results in decays producing a monochromatic gamma ray line, which is constrained by X-ray measurements [87, 88, 66, 89, 90], while the warm nature of dark matter from DW production disrupts small scale structure formation, which is constrained by Lyman-α measurements [69, 41, 68]. The combination of these two constraints now rule out DW as a viable production mechanism for sterile neutrino dark matter (see, e.g. [111] for a recent summary).

Several alternate production mechanisms that circumvent these bounds to various degrees exist in the literature [45, 92, 112, 48, 41, 113, 114, 94, 99, 95, 115, 116]. The Shi-Fuller mechanism [45] produces a colder population but requires fine-tuned parameters to ensure resonant production in the νMSM, and might still be incompatible with structure formation [117, 118]. Thermal freeze-out with additional interactions, followed by appropriate entropy dilution, can result in the correct relic abundance [113, 112, 114], but faces strong constraints from BBN [119]. One mechanism that is particularly successful and employed widely is sterile neutrino dark matter production through the freeze-in mechanism [120, 28] via a feeble coupling to some particle beyond the SM present in the early Universe. This can be realized in several motivated frameworks: this particle could be the inflaton [49], a heavy higgs in an extended Higgs sector [50, 51, 52, 53, 54, 55, 56], a scalar that breaks a symmetry that the sterile neutrinos might be charged under [13, 15], a charged scalar motivated by leptogenesis [57], the radion in warped extra dimension models [58], or pseudo-Dirac neutrinos [59]; for

a recent review of various scenarios that admit freeze-in of sterile neutrino dark matter, see Ref. [60]. Such scenarios carry the dual virtues of a colder sterile neutrino population compared to DW as well as not relying on any mixing with the active neutrinos for production, thereby alleviating the tension with Lyman-α and X-ray measurements.

The phenomenological signatures of sterile neutrino dark matter from such freeze-in scenarios are in stark contrast to those from DW production. In the latter framework, the "smoking gun" signature is a monochromatic X-ray line from the loop level decay into an active neutrino and a single photon, induced by the mixing between active and sterile neutrinos required for DW production. In the freeze-in scenario, this mixing angle can be arbitrarily small, and there is essentially no direct coupling between the sterile neutrino dark matter candidate and the SM particles; hence no signals arising from such active-sterile mixing that characterize sterile neutrino dark matter from DW, such as astrophysical signatures in gamma rays or direct production in searches for neutral leptons in laboratory experiments [104, 105, 106, 107, 108, 109], are expected. The most promising observable imprints are instead of a cosmological nature: the phase space distribution of sterile neutrinos from freeze-in is distinct from that arising from DW, and can lead to possible deviations in free-streaming lengths of warm dark matter or the dark radiation content of the Universe during BBN or CMB decoupling. Although the exact properties depend on the details of the underlying model, given that such cosmological imprints offer the most direct probes of sterile neutrino dark matter from freeze-in, it is worth studying such features in greater detail in a broad framework.

In this chapter (based on [14]), we will investigate such potentially observable cosmological aspects of sterile neutrino dark matter. We focus on the framework presented in chapter 5, which admits many cosmologically interesting variations: production can occur via annihilation processes from higher dimensional operators that are active at the highest temperatures (referred to as ultraviolet (UV) freeze-in), or from decays of a scalar, which occur at lower temperatures (infrared (IR) freeze-in); the scalar producing the dark matter population can be taken to be in or out of equilibrium with the thermal bath; moreover, both supersymmetric and non-supersymmetric setups can be considered. The framework therefore covers a diverse range of possibilities, allowing us to both extract generic properties and highlight features unique to particular variations. Similar studies have been performed in previous work in the literature [71, 50], but in a more constrained framework of a keV scale sterile neutrino with IR production only in a non-supersymmetric setup.

6.1 Theoretical Framework and Scenarios

We begin by outlining the theoretical framework for this study, based on the model presented in chapter 5. The SM is extended by three right-handed sterile neutrinos $N_{1,2,3}$, which are assumed to be charged under a new symmetry $U(1)'$. This symmetry is broken by the vacuum expectation value (vev) of a scalar ϕ, which carries a $U(1)'$ charge opposite to that of the N_i, such that $N_i\phi$ is a $U(1)'$ and SM singlet. These charge assignments lead to no new renormalizable interactions, and the following terms appear at leading order (dimension five):

$$\mathcal{L} \supset \frac{y_{ij}}{M_*} L_i H N_j \phi + \frac{x_i}{M_*} \phi\,\phi N_i N_i \,, \tag{6.1}$$

where M_* is the UV-cutoff for this theory (which we take to be the GUT scale $M_* = 10^{16}$ GeV), L_i is the SM lepton doublet of flavor i, H is the SM Higgs doublet, and the N_i are chosen to be in a basis where x_i is diagonal. With vev insertions of both ϕ and the SM Higgs, these terms lead to the familiar Majorana and Dirac masses that give rise to the see-saw mechanism. In the above setup, the following masses for the active and sterile neutrino eigenstates and mixing between the two sectors are generated (indices have been suppressed):

$$m_{N_i} = \frac{x_i \langle \phi \rangle^2}{M_*}, \quad m_a = \frac{y^2 \langle H \rangle^2}{x M_*}, \quad \sin\theta \approx \frac{y \langle H \rangle}{x \langle \phi \rangle}. \tag{6.2}$$

This setup is appealing since phenomenologically interesting (keV-GeV) masses for the sterile neutrinos are realized with $\mathcal{O}(1)$ values for the dimensionless couplings x and y and a high scale of new physics corresponding to $\langle \phi \rangle \sim 1 - 100$ PeV (see chapter 5 for details). The parameters are constrained by the see-saw requirement and cannot be completely arbitrary. We pick N_1 to be the sterile neutrino dark matter candidate. In this chapter, the parameters are constrained as follows:

- m_ϕ and $\langle \phi \rangle$ are taken to be free parameters.

- Fixing the sterile neutrino masses fixes $x_i = M_* m_{N_i}/\langle \phi \rangle^2$. Cosmological constraints require $N_{2,3}$ to decay before BBN [47, 48, 37, 102, 103], constraining them to GeV scale or heavier masses. We fix $m_{2,3} =$(1.0 GeV, 1.1 GeV), which fixes x_2, x_3, unless specified otherwise. We leave m_{N_1} (hence x_1) as a free parameter.

- For fixed sterile neutrino masses, the y_{ij} couplings are fixed by constraints on the active-sterile mixing angles. For the dark matter candidate N_1, its mixing with the active neutrinos needs to be heavily suppressed in order for it to be long-lived, which is accomplished by making the corresponding couplings arbitrarily small, essentially $y_{i1} \sim 0$ (which also renders the lightest active neutrino essentially massless). While

such small couplings appear fine-tuned, the limit in which they vanish is technically natural since this enhances the framework by a $\mathbb{Z}_2$ symmetry for N_1. The remaining y_{ij} are fixed by the requirements of matching the neutrino oscillation data (for $m_{2,3} =$ (1.0 GeV, 1.1 GeV) and $\langle\phi\rangle$ at the PeV scale, these couplings are $\mathcal{O}(1)$; see [13]).

6.1.1 Dark Matter Production Channels

While the above formalism was implemented to naturally explain neutrino masses and light sterile neutrinos, it also opens possibilities for N_1 production in the early Universe.

The first term in equation 6.1 leads to ϕ production via $L\,H \rightarrow N_{2,3}\,\phi$ (note that no N_1 is produced since $y_{i1} \sim 0$), and the second term leads to $\phi \rightarrow N_i N_i$ decays after ϕ obtains a vev. The relic abundance of N_1 produced in this manner is approximately [13]

$$\Omega_{N_1} h^2 \sim 0.1 \sum_{i,j} y_{ij}^2 \left(\frac{m_{N_1}}{\text{GeV}}\right) \left(\frac{1000\,T_{RH}\,M_P}{M_*^2}\right) Br(\phi \rightarrow N_1 N_1) \tag{6.3}$$

which is sensitive to the reheat temperature T_{RH}, at which ϕ production via $L\,H \rightarrow N_{2,3}\,\phi$ is assumed to begin.

If ϕ has additional interactions that are strong enough to keep it in equilibrium with the thermal bath in the early Universe (these can, for instance, arise from the interaction terms that lead to ϕ obtaining a vev), two distinct production mechanisms are possible for N_1. At high temperatures, $\phi\phi \rightarrow N_1 N_1$ (termed ultraviolet (UV) freeze-in) results in the approximate N_1 abundance [13]

$$\Omega_{N_1} h^2 \sim 0.1\, x_1^2 \left(\frac{m_{N_1}}{\text{GeV}}\right) \left(\frac{1000\,T_R\,M_{Pl}}{M_*^2}\right). \tag{6.4}$$

Once ϕ obtains a vev, the decay process $\phi \rightarrow N_1 N_1$ also occurs (termed infrared (IR) freeze-in) with an effective coupling $x_{1\,\text{eff}} = \frac{2\,x_1\,\langle\phi\rangle}{M_*}$, giving an approximate abundance [13]

$$\Omega_{N_1} h^2 \sim 0.1 \left(\frac{x_{1\,\text{eff}}}{1.4 \times 10^{-8}}\right)^3 \left(\frac{\langle\phi\rangle}{m_\phi}\right). \tag{6.5}$$

In this case, we have assumed that the additional interactions cause ϕ to rapidly decay into SM radiation once it goes out of equilibrium, so that N_1 production occurs only while ϕ is in equilibrium.

6.1.2 Supersymmetric Extension

The above setup requires new physics that breaks the $U(1)'$ via a ϕ vev at high scales. Given that supersymmetry is well-motivated yet there are no signs of supersymmetry close to the weak scale, one can entertain the possibility that supersymmetry exists at a higher scale and the breaking of $U(1)'$ is tied to supersymmetry breaking. This consideration motivates a supersymmetric extension of the Lagrangian above. We introduce a chiral supermultiplet Φ with spin $(0, 1/2)$ components (ϕ, ψ) and three chiral supermultiplets $\mathcal{N}_i$ with components $(\tilde{N}_i, N_i)$, leading to the superpotential

$$\mathcal{W} \supset \frac{\xi_{ij}}{M_*} \mathcal{L}_i \mathcal{H}_u \mathcal{N}_j \Phi + \frac{\eta_i}{M_*} \mathcal{N}_i \mathcal{N}_i \Phi \Phi \,. \tag{6.6}$$

This gives rise to the Lagrangian terms listed in equation 6.1 along with some other terms. In addition, the following soft terms that can appear in the Lagrangian after supersymmetry breaking are important for our discussion:

$$\mathcal{L} \supset \xi_{ij} \frac{A_{\xi_{ij}}}{M_*} \tilde{L}_i h_u \tilde{N}_j \phi + \eta_i \frac{A_{\eta_i}}{M_*} \tilde{N}_i \tilde{N}_i \phi \phi \,, \tag{6.7}$$

The first term leads to mixing between the sterile and standard sneutrinos, whereas the second term gives rise to the decay process $\phi \to \tilde{N}_j \tilde{N}_j$ if $m_\phi > 2m_{\tilde{N}_j}$. For simplicity, we assume R-parity and take a sub-TeV Higgsino to be the LSP, which will thus account for a small fraction of dark matter.

In this supersymmetric extension, additional production channels and constraints come into play due to the presence of new interactions and superpartners, leading to qualitative differences from the non-supersymmetric setup. Of primary relevance are the fermion ψ and the sterile sneutrinos $\tilde{N}_i$, which are assumed to have masses of the same scale as ϕ as they are all assumed to originate from supersymmetry breaking. The sterile sneutrinos decay via $\tilde{N}_{2,3} \to \tilde{H}\nu$ (with a ϕ vev insertion) or via their mixing with the standard sneutrinos induced by the soft term proportional to A_ξ in equation 6.7. The decay mechanism for the sterile sneutrino $\tilde{N}_1$ is more pertinent. If it has significant mixing with other sneutrinos, it decays through the standard sneutrino channels; however, if this mixing is significantly suppressed (this would be technically natural, corresponding to the same $\mathbb{Z}_2$ symmetry that makes N_1 long-lived), its decay must originate from the $\mathcal{N}_i \mathcal{N}_i \Phi \Phi$ term in the superpotential. We assume $m_{\tilde{N}_1} > m_\psi$, so that $\tilde{N}_1$ decays via $\tilde{N}_1 \to \psi N_1$ (with a ϕ vev insertion), such that each $\tilde{N}_1$ decay produces one N_1 particle, while ψ decays as $\psi \to \nu \tilde{H} N_{2,3}$. To avoid non-thermal production of the LSP at late times, we require these decays to occur before LSP decoupling (a sub-TeV $m_{\tilde{H}}$ can generally be picked to satisfy this constraint, unless extreme

values of the parameters are chosen). The other choice $m_\psi > m_{\tilde{N}_1}$ requires $\tilde{N}_1$ to decay via an off-shell ψ and generally has an extremely long lifetime that leads to inconsistencies, hence we do not consider it further.

6.1.3 Four Scenarios

Based on the above possibilities, we will divide our study into the following scenarios:

- Scenario I: ϕ in equilibrium, no supersymmetry

- Scenario II: ϕ freezes in, no supersymmetry

- Scenario III: ϕ in equilibrium, supersymmetry

- Scenario IV: ϕ freezes in, supersymmetry

We will consider each scenario in detail in turn in Section 6.3. Before that, we turn to a discussion of the formalism we employ to perform our studies.

6.2 Formalism

All the information relevant for calculating various quantities of interest is contained in the phase space distribution of the sterile neutrinos. In this section, we describe our formalism for tracking this phase space distribution from when these particles are produced to the present era, and the subsequent calculation of the various observables of interest.

6.2.1 Boltzmann Equations

The evolution of the phase space density of particles is given by the Boltzmann equations. These take the form $L[f] = C[f]$, where the Liouville operator L is

$$L = \frac{\partial}{\partial t} - Hp\frac{\partial}{\partial p} \tag{6.8}$$

with H the Hubble parameter, and $C[f]$ is a sum of collision terms, each corresponding to an interaction. Here $f = f(\mathbf{p}, T)$ is the phase space density of a particle species, whose distribution is assumed to be homogenous and isotropic. We use the photon temperature T to track the evolution of the phase space density. The Universe is generally radiation dominated throughout the period of interest, so that

$$H(T) = \frac{T^2}{M_0} \ , \ \text{with } M_0 = \left(\frac{45M_{Pl}^2}{4\pi^3 g_*}\right)^{1/2} \ , \tag{6.9}$$

where g_* is the number of degrees of freedom in the bath. In some scenarios, there are heavy long-lived particles that introduce a period of matter domination, modifying the above relation; we account for such effects where necessary.

Following [71], we work with the coordinates $x_i = p_i/T$, $r = m_\phi/T$ (where i denotes the particle species of interest), which leads to a simplification of the Liouville operator

$$L = Hr\frac{\partial}{\partial r} \tag{6.10}$$

assuming g_* is constant, which is a good approximation for various stages of sterile neutrino production we study in this chapter.

The collision term for a particular phase space density f_X and scattering process $X + i + j + \ldots \leftrightarrow a + b + \ldots$ is given by:

$$C[f_X] = \frac{1}{2E_X}\int\left(\prod_{I=i,j,\ldots}\mathrm{d}\Pi_I\right)\left(\prod_{A=a,b,\ldots}\mathrm{d}\Pi_A\right)(2\pi)^4\,\delta^4\left(\Sigma p\right)|\mathcal{M}|^2\,\Omega(X+i+j+\ldots \leftrightarrow a+b+\ldots),$$
$$\tag{6.11}$$

with

$$\mathrm{d}\Pi_x = \frac{g_x}{(2\pi)^3}\frac{\mathrm{d}^3 p_x}{2E_x}, \tag{6.12}$$

where g_x counts the internal degrees of freedom of particle x. The factor Ω is the phase space density weight, given by

$$\Omega(X+i+j+\ldots \leftrightarrow a+b+\ldots) = f_i f_j \ldots f_X(1\pm f_a)(1\pm f_b)\ldots - f_a f_b \ldots (1\pm f_i)(1\pm f_i)\ldots(1\pm f_X),$$
$$\tag{6.13}$$

with $+$ for bosons and $-$ for fermions. $|\mathcal{M}|^2$ is the squared matrix element for the scattering process of interest, averaged over initial and final states, including any symmetry factors.

Details of the Boltzmann equations and collision terms for each scenario are presented in appendix A. For a detailed discussion of several subtle factors in solving the Boltzmann equations for the freeze-in of sterile neutrinos, we refer the interested reader to Ref. [121].

6.2.2 Degrees of Freedom and Entropy Dilution

An important aspect of calculating the abundance and momentum distribution of sterile neutrino dark matter is taking into account any changes in the effective number of degrees of freedom, g_*, and entropy, S, between dark matter production and the present epoch. Since N_1 is out of equilibrium from the moment of production, such changes in S and g_* will heat up the thermal bath without introducing any energy into the dark sector, therefore redshifting its momentum relative to the visible sector as well as diluting its abundance.

There are several such major transitions:

1. Reduction of the supersymmetric degrees of freedom, around $T \sim \langle \phi \rangle$. Before super-partners decouple, $g_{*\mathrm{SUSY}} \sim 300$ [1], which drops to $g_{*\mathrm{SM}} \approx 100$.

2. Reduction of the SM degrees of freedom. This reduces $g_{*\mathrm{SM}} \approx 100$ above electroweak temperatures to $g_{*0} = 3.91$ at present.

3. Decay of the additional sterile neutrinos $N_{2,3}$.

4. Decay of the sterile sneutrino $\tilde{N}_1$. This needs to be treated separate from the rest of the supersymmetric spectrum as $\tilde{N}_1$ is long-lived and can lead to a period of matter domination before it decays.

For simplicity, we assume that dark matter production, as well as ϕ, ψ, and $\tilde{N}_i$ production, take place during epochs of constant g_*. A change in the number of degrees of freedom or entropy affect the expansion rate of the Universe and hence the momentum distribution of a particle species. However, this effect is different for particles in equilibrium with the photons and for decoupled particles.

For a species X in equilibrium with the photons, the number density n_X simply scales as T^3, where T is the temperature of the photons. The temperature T may be found using the definition of entropy $S = g_{*s} T^3 R^3$. Therefore, a change in entropy or the degrees of freedom will affect the temperature of the photons and hence the number density of X, in a predictable way.

Now consider a particle species Y that is decoupled from the thermal bath. If Y is a thermal relic, one might define a temperature T_Y for this species that scales differently than the photon temperature. In this case, the number density n_Y simply scales like T_Y^3, and T_Y scales as R^{-1}. So the abundance of a decoupled species will simply dilute due to the expanding Universe. Another way to see this is that because Y is decoupled, the total number of Y particles in a given comoving volume should be constant, i.e. $n_Y R^3$ is constant. In this sense, changes in entropy or degrees of freedom do not affect the evolution of Y, given the scale factor R. For an example of this type of calculation, see the treatment of neutrino decoupling in [19].

However this approach to studying the evolution of a decoupled species is not always applicable, particularly when Y was never in equilibrium and there is no clear way to define a temperature for the species. Instead, we can relate the evolution of Y to the temperature

---

[1] Since the theory contains ϕ, ψ, and possibly additional fields involved with $U(1)'$ breaking, the field content is presumably much larger than the MSSM, and we use $g_{*\mathrm{SUSY}} \sim 300$ as a representative value; our final results are not very sensitive to the exact choice for this number.

of the photons, and in doing so we will see some dependance on S and g_{*s}. First, consider a decoupled particle with initial momentum p_i. Its momentum will simply redshift as $p = \frac{R_i}{R}p_i$ while the Universe expands. Therefore, if a particle has momentum p_f after some process that changes the total entropy S or degrees of freedom g_{*s}, it must have had momentum $p_i = \frac{R_f}{R_i}p_f$ before the process. The ratio of scale factors can be expressed as

$$\frac{R_f}{R_i} = \left(\frac{S_f}{S_i}\right)^{1/3}\left(\frac{g_{*si}}{g_{*sf}}\right)^{1/3}\frac{T_i}{T_f}. \tag{6.14}$$

This means that we can relate the momentum distribution of species Y after the process, at time t_f, to the distribution before the process, at time t_i:

$$f_Y(p, t_f) = f_Y\left(\left(\frac{S_f}{S_i}\right)^{1/3}\left(\frac{g_{*si}}{g_{*sf}}\right)^{1/3}\frac{T_i}{T_f}p, t_i\right). \tag{6.15}$$

From this it is straightforward to find how the number density changes after such a process:

$$n_Y(t_f) = \frac{g}{(2\pi)^3}\int f(p, t_f)d^3p \tag{6.16}$$

$$= \frac{S_i}{S_f}\frac{g_{*sf}}{g_{*si}}\left(\frac{T_f}{T_i}\right)^3\frac{g}{(2\pi)^3}\int f(p, t_i)d^3p \tag{6.17}$$

$$= \frac{S_i}{S_f}\frac{g_{*sf}}{g_{*si}}\left(\frac{T_f}{T_i}\right)^3 n_Y(t_i). \tag{6.18}$$

Dividing out the $T^3 g_{*s}$ dependance of the number density, we find that the yield, Y_Y, simply scales as

$$Y_Y(t_f) = \frac{S_i}{S_f}Y_Y(t_i). \tag{6.19}$$

Calculating the entropy dilution from the decay of the heavier (GeV scale) sterile neutrinos $N_{2,3}$ is slightly involved as they thermalize, decouple while still relativistic around $\mathcal{O}(20)$ GeV [48], and decay late (just before BBN). The ratio of entropy from $N_{2,3}$ decays to the entropy in the remainder of the system, which provides the suppression factor for the dark matter relic density, is calculated to be [122, 113, 48]

$$S_{N23} \approx \left(1 + \sum_{i=2,3} 2.95 \left(\frac{2\pi^2\bar{g}_*}{45}\right)^{1/3}\left(\frac{Y_{N_i}^2 m_{N_i}^2}{M_{Pl}\Gamma_{N_i}}\right)^{2/3}\right)^{3/4}, \tag{6.20}$$

where Γ_{N_i} is the decay width of the sterile neutrino N_i, $\bar{g}_*$ is the average effective number of degrees of freedom during $N_{2,3}$ decay, and Y_{N_i} is the yield abundance when N_i decouples, given by [122, 113]

$$Y_{N_i} = \frac{135\,\zeta(3)}{4\pi^4 g_*}, \tag{6.21}$$

where g_* represents the number of degrees of freedom when N_i decouples. The numerical value of S_{N23} can thus be estimated by calculating the decay widths Γ_{N_i} [113] and using the information that $N_{2,3}$ decouple around $\mathcal{O}(20)$ GeV [48]. For GeV scale or heavier $N_{2,3}$, this results in $S_{N23} \lesssim 30$.

If the sterile sneutrino $\tilde{N}_1$ is sufficiently long-lived and abundant that its energy density grows to be comparable to or larger than the total energy density in the thermal bath, its decays lead to a significant entropy dump into the thermal bath, significantly raising its temperature. In this scenario, the amount of entropy released from $\tilde{N}_1$ decay relative to the entropy present in the bath, and the temperature the bath is heated to from such decays, can be calculated as [19]:

$$\frac{S_f}{S_i} \approx 1.83\, g_*^{1/4}\, \frac{m_{\tilde{N}_1} Y_{\tilde{N}_1} \tau_{\tilde{N}_1}^{1/2}}{M_{Pl}^{1/2}}, \tag{6.22}$$

$$T_{decay} \approx 0.55\, g_*^{-1/4}\, (M_{Pl}/\tau_{\tilde{N}_1})^{1/2}, \tag{6.23}$$

where $\tau_{\tilde{N}_1}$ is the lifetime of the sterile sneutrino.

6.2.3 Observables

The phase space distribution calculated from the above prescription can be used to calculate several observables of interest. The ones we study in this chapter are as follows:

Relic Density

The relic density, Ω_{N_1}, can be expressed in terms of the distribution $f_{N_1}(x, T)$ as:

$$\Omega_{N_1} = \frac{n_{N_1} m_{N_1}}{\rho_c} = \frac{g_{N_1} m_{N_1} T^3}{2\pi^2 \rho_c} \int_0^\infty \mathrm{d}x\ x^2 f_{N_1}(x, T), \tag{6.24}$$

where ρ_c is the critical density.

Effective Number of Relativistic Degrees of Freedom

$\Delta N_{\text{eff}}(\text{BBN})$, the contribution to the effective number of relativistic degrees of freedom during BBN, can be estimated as

$$\Delta N_{\text{eff}}(\text{BBN}) = \frac{\rho - n m_{N_1}}{2\rho_{\text{therm}}^{\text{ferm}}}$$

$$= \frac{60}{7\pi^4} \frac{m_{N_1}}{T_{BBN}} \int_0^\infty dx \, x^2 \left(\sqrt{1 + \left(\frac{x}{m_{N_1}/T_{BBN}} \right)^2} - 1 \right) f_{N_1}(x, T_{BBN}), \quad (6.25)$$

[71] which compares the kinetic part of the sterile neutrino energy density with $\rho_{\text{therm}}^{\text{ferm}}$, the energy density of a perfectly relativistic fermionic species in equilibrium at the same temperature. As in [71], we take $T_{BBN} = 4$ MeV. Current measurements bound this contribution at the level of $\Delta N_{\text{eff}}(\text{BBN}) \lesssim 0.5$ [123], and $\mathcal{O}(0.1)$ values might be probed by future measurements. There exist stronger bounds on ΔN_{eff} from the era of CMB decoupling; however, these are generally less stringent for sterile neutrino dark matter as it tends to redshift and become nonrelativistic by this time [71]. Therefore, we only consider bounds from the BBN era here.

Free-Streaming Length

The free-streaming length, Λ_{FS}, is calculated as the average comoving distance traveled by a dark matter particle since the time of production:

$$\Lambda_{FS} = \int_{T_p}^{T_0} \frac{\langle v(T) \rangle}{a(T)} \frac{dt}{dT} \, dT \, . \tag{6.26}$$

The average velocity of a dark matter particle is calculated using the phase space distribution function as

$$\langle v(T) \rangle = \frac{\int_0^\infty dx \, \frac{x^3}{\sqrt{x^2 + (m_{N_1}/T)^2}} f_{N_1}(x, T)}{\int_0^\infty dx \, x^2 f_{N_1}(x, T)} \, . \tag{6.27}$$

The relationship between time and temperature (which enters here as dt/dT) takes a different form during radiation and matter dominated eras. We assume that the Universe is dominated by radiation until $T_{\text{eq}} = 1.48$ eV, at which point matter domination begins. In supersymmetric scenarios, we also take into account an early period of matter domination coming from a sizable $\tilde{N}_1$ abundance. We find that the current era of vacuum domination contributes negligibly to the free-streaming length since the sterile neutrinos are very cold and by the time of vacuum dominance.

As a rough guide, we take the regimes for cold, warm, and hot dark matter to be approximately $\Lambda_{FS} \lesssim 0.01$ Mpc, $0.01 \lesssim \Lambda_{FS} \lesssim 0.1$ Mpc, and 0.1 Mpc $\lesssim \Lambda_{FS}$ respectively [71].

6.3 Results

Having established our framework and formalism, in this section we present our results for each of the four scenarios of interest. For all scenarios, we assume that N_i has negligible initial abundance, so that $f_{N_i} \ll 1$ in the early Universe; any interaction involving N_i in the initial state can then be neglected, resulting in a simplification of the Boltzmann equations. The same also applies to ϕ abundance in scenarios where it also freezes in (Scenarios II and IV). In scenarios where ϕ is in equilibrium with the SM thermal bath (Scenarios I and III), we assume that the equilibrium abundance is maintained down to some critical decoupling temperature T_d, below which it rapidly decays to SM radiation:

$$f_\phi(p_\phi, T) \approx \begin{cases} e^{-E_\phi/T} & T > T_d \\ 0 & T < T_d \end{cases} \tag{6.28}$$

We assume $T_d \approx m_\phi/20$, analogous to WIMP decoupling scenarios. Specific details of the Boltzmann equation and collision terms for each scenario are presented in appendix A.

In all cases we study, we verify that the conditions for N_1 to freeze-in and not reach equilibrium abundance [28] are satisfied; for N_1 freezing in when ϕ is in equilibrium, for instance, this condition is

$$4 \frac{M_{\rm Pl}}{m_\phi} \left(\frac{m_{N_1}}{\langle \phi \rangle} \right)^2 < 1. \tag{6.29}$$

6.3.1 Scenario I: ϕ in equilibrium, no supersymmetry

In this scenario, the relevant processes for N_1 production are the UV interactions $\phi\phi \leftrightarrow N_1 N_1$ and the decay process $\phi \to N_i N_i$ (note that the contributions from $L_i H \leftrightarrow N_1 \phi$, including all permutations, and Higgs decay $H \to L N_1$ are irrelevant because the corresponding Yukawa coupling y_{i1} is vanishingly small). It is then interesting to see the interplay between these two contributions. Recall that the UV production rate is sensitive to the reheat temperature T_{RH}, and higher reheat temperatures correspond to greater N_1 production (see equation 6.4). The left panel of figure 6.1 shows how the ϕ and N_1 abundances evolve during the early Universe for two different cases, corresponding to reheat temperatures of
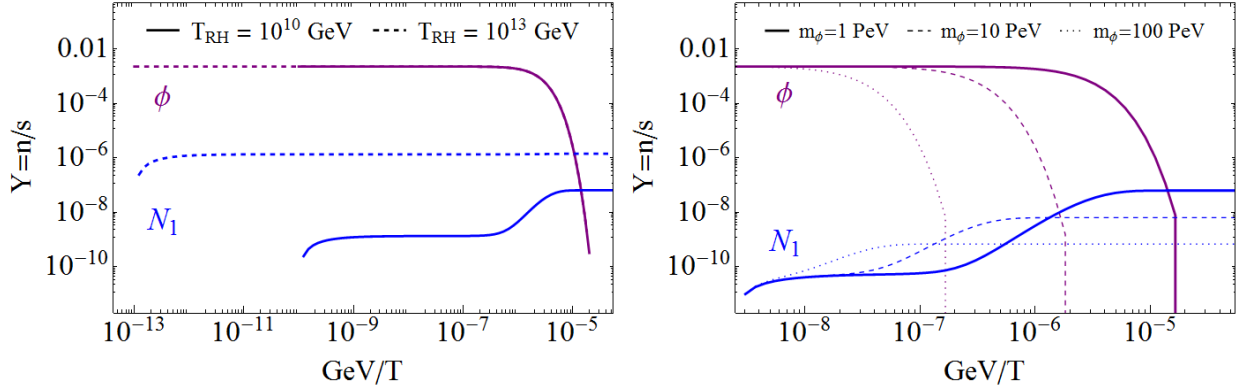
Figure 6.1: Evolution of the abundances of ϕ (purple) and N_1 (blue). Left panel: Two different reheat temperatures 10^{10} GeV (solid lines) and 10^{13} GeV (dashed lines), showing IR and UV dominated production of dark matter. Here $m_\phi = 1$ PeV. Right panel: Three different values of m_ϕ (1 PeV, 10 PeV, 100 PeV). Here $T_{RH} = 400$ PeV. For both plots, $\langle\phi\rangle = 100$ PeV and $m_{N_1} = 1$ GeV.

10^{10} GeV (solid curves) and 10^{13} GeV (dashed curves) [2]. In the former case, only a small fraction of N_1 comes from UV freeze-in, and most of it is produced from IR freeze-in, which only turns on later, as evident from the large second bump on the solid blue curve. In the latter case with the higher reheat temperature, UV production accounts for all of the dark matter abundance, as seen in the dotted blue curve, which flattens very early. For both cases, ϕ tracks a thermal distribution, decouples, and then decays away (equation 6.28). The effect of varying m_ϕ is illustrated in the right panel of figure 6.1, where we see the increasing m_ϕ leads to a reduced abundance of N_1: although the decay rate grows as $\Gamma_\phi \propto m_\phi$, the time available for such decays to occur drops as $t \propto m_\phi^{-2}$.

In figure 6.2, we show the ratio of UV to IR contributions to the final dark matter abundance for different values of the scalar mass m_ϕ and reheat temperature T_{RH}. Depending on the choice of parameters, we see that either UV or IR freeze-in can be the dominant source of N_1 abundance. In the UV dominated regime, the relic density should be independent of m_ϕ as long as $m_\phi \ll T_{RH}$, since production is dominant at higher temperatures, where ϕ is effectively massless. This is visible in the dotted line, which represents the contour for the correct relic density with $x_1 = 0.1$, and indeed does not show any m_ϕ dependence. On the other hand, we see that the abundance from IR production is sensitive to m_ϕ, and decreases for larger m_ϕ (which is also illustrated in the right panel of figure 6.1). This behavior is captured in the solid curve, which represents the contour for the correct relic density with $x_1 = 1$; as m_ϕ increases, this switches from being IR dominated and insensitive to T_{RH}

---

[2]Plots in figure 6.1 are primarily intended to show the effect of T_{RH} and m_ϕ on dark matter production, and do not not have the correct relic density everywhere.
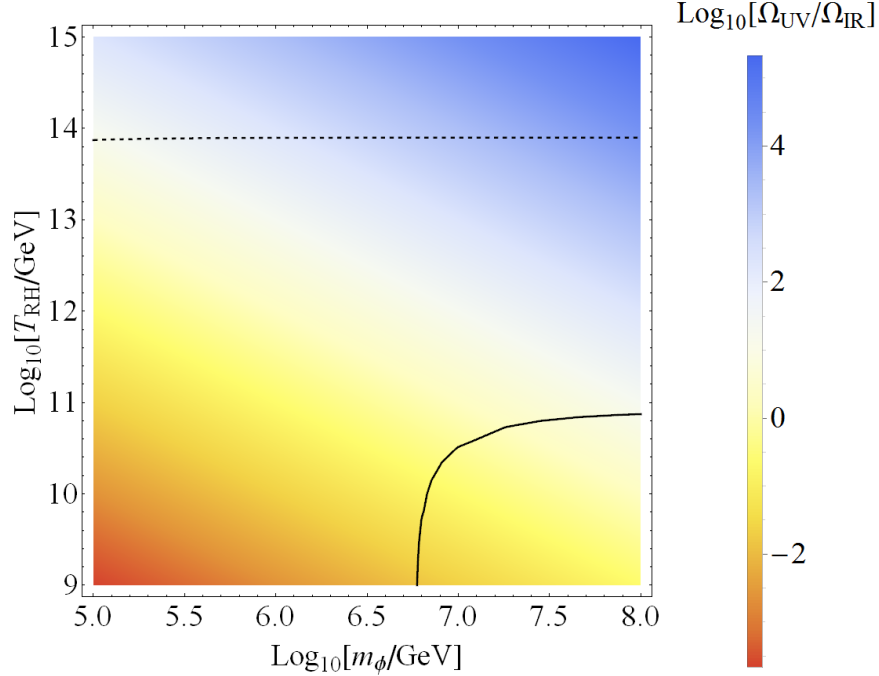
Figure 6.2: The ratio of N_1 abundances produced from UV and IR processes. The solid and dashed lines denote where the correct dark matter abundance is achieved for $x_1 = 1, 0.1$ ($m_N = 1, 0.1$ GeV) respectively. For this plot we set $\langle \phi \rangle = 100$ PeV

(vertical part) to UV dominated and insensitive to m_ϕ. (horizontal part).

Next, we examine the parameter space where the correct relic abundance to account for all of the observed dark matter can be obtained. This is shown in figure 6.3 as a function of the coupling x_1 and the scalar vev $\langle \phi \rangle$; for this plot, the reheat temperature is taken to be sufficiently low that only IR production is relevant. The correct relic abundance can be obtained by varying the scalar mass m_ϕ, and the black lines show contours of various choices of m_ϕ for which this is achieved. For a fixed $\langle \phi \rangle$, larger m_ϕ lead to lowered N_1 abundances, as discussed in the previous paragraph; this therefore needs to be compensated by larger couplings x_1, leading to a larger decay width into N_1 to maintain the correct abundance, as seen in the figure. These parameters also fix the mass of the dark matter particle N_1; in the plot, we denote contours of various m_{N_1} values by colored dashed lines. This plot demonstrates that for m_ϕ and $\langle \phi \rangle$ at the PeV scale, the correct dark matter abundance is obtained for N_1 at or below GeV scale masses.

Next, we study the various observables related to the dark matter phase space distribution. figure 6.4 shows the present distribution arising from the two production mechanisms, UV and IR freeze-in, in blue and red respectively. Despite the two production mechanisms being very different, we see from the plot that the two corresponding distributions are very
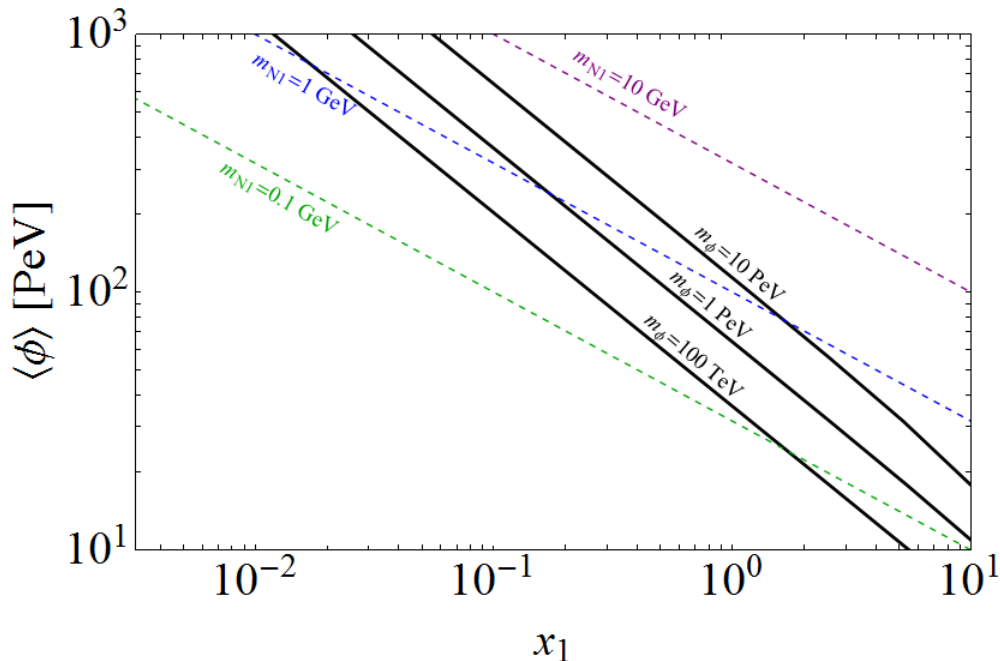
Figure 6.3: Parameter combinations that yield the correct relic density. For each point on the plot, the correct relic density can be obtained for an appropriate choice of m_ϕ; contours of some representative values are shown as black lines. The parameters also fix the dark matter mass; contours of various m_{N_1} are shown as dotted, colored lines. Here, the reheat temperature is fixed to $T_{RH} = 10^{10}$ GeV, hence UV production is negligible.

similar. This similarity arises because in both mechanisms N_1 is produced from particles that are in equilibrium with the thermal bath, hence the characteristic energy scale at the time of production in both instances is $E_{N_1} \approx p_{N_1} \approx T$, the temperature of the bath. The UV component is slightly warmer since the annihilation rate is proportional to the center of mass energy of the process, hence dark matter is preferentially produced from interactions involving particles from the higher energy end of the equilibrium distribution. As the universe cools, the dark matter population redshifts along with the SM bath, such that $p_{N_1} \approx T$ is maintained; however, as degrees of freedom decouple, their decay products heat up the SM thermal bath but not the dark matter population, resulting in the final dark matter distribution peaking at $p_{N_1}/T < 1$. Thus, in this scenario, the dark matter population is generally colder than the SM thermal bath.

Figure 6.5 displays the free streaming length, Λ_{FS}, and change in the effective number of relativistic degrees of freedom at the time of BBN, ΔN_{eff}. Here we have chosen a low reheat temperature, $T_{RH} = 10^9$ GeV, so that N_1 is produced primarily through IR freeze-in. Black lines denote where N_1 composes all of dark matter; to the left of these lines, N_1 is underabundant, and can be compensated for by turning on UV production. In this scenario,
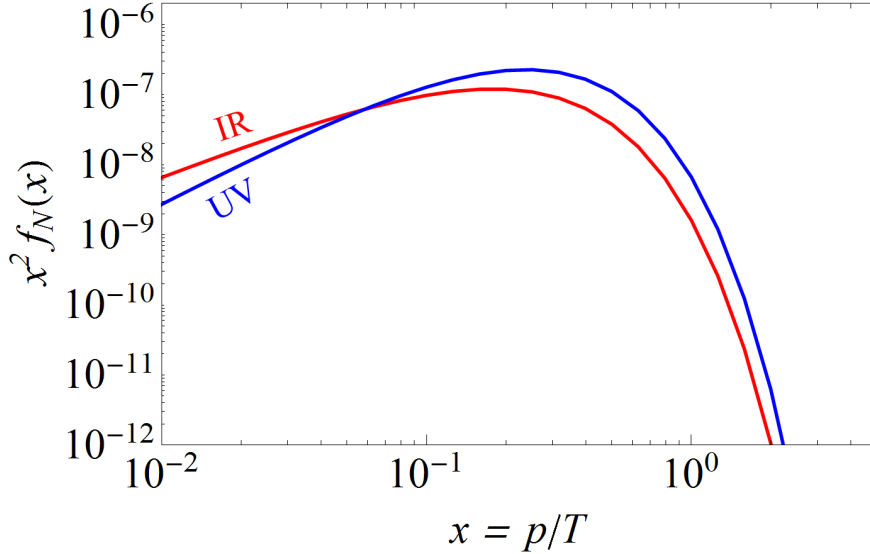
Figure 6.4: The dark matter phase space distribution from UV (blue) and IR (red) freeze-in, for $\langle \phi \rangle = 100$ PeV, $m_\phi = 1$ PeV, $m_{N_1} = 1$ GeV, $T_{RH} = 10^{12}$ GeV.

for these parameters, it is clear that dark matter is very cold, with $\Lambda_{FS} \sim 10^{-6} - 10^{-8}$ Mpc, and contributes negligibly to ΔN_{eff} at BBN. We have checked that these statements continue to hold in UV dominated scenarios, as is expected from the similarity in the phase space distributions for IR and UV production.

To summarize, in this scenario, we find that dark matter can be produced with the desired relic density through a combination of UV and IR freeze-in processes, and is generally cold, so it satisfies all constraints comfortably while not showing any significant deviations from cold dark matter.

6.3.2 Scenario II: ϕ freezes in, no supersymmetry

This scenario assumes that ϕ does not have any significant additional interactions, and the interactions listed in equation 6.1 are therefore the ones governing its dynamics. Thus ϕ does not enter into equilibrium with the thermal bath in the early Universe, and its abundance is instead produced from freeze-in, via the UV process $L_i H \rightarrow N_{2,3} \phi$ (note that permutations of this process with $N_{2,3}$ in the initial state are absent since the heavier sterile neutrinos $N_{2,3}$ are absent in the early Universe). Thus $f_\phi \ll 1$, and its abundance needs to be tracked using the Boltzmann equations. This frozen-in population of ϕ then decays entirely into sterile neutrinos once ϕ obtains a vev, as there are no competing decays into SM particles, thereby producing dark matter via $\phi \rightarrow N_1 N_1$. Note that the UV freeze-in process $\phi\phi \rightarrow N_1 N_1$ is inactive here due to the suppressed abundance of ϕ at high temperatures. Details of the
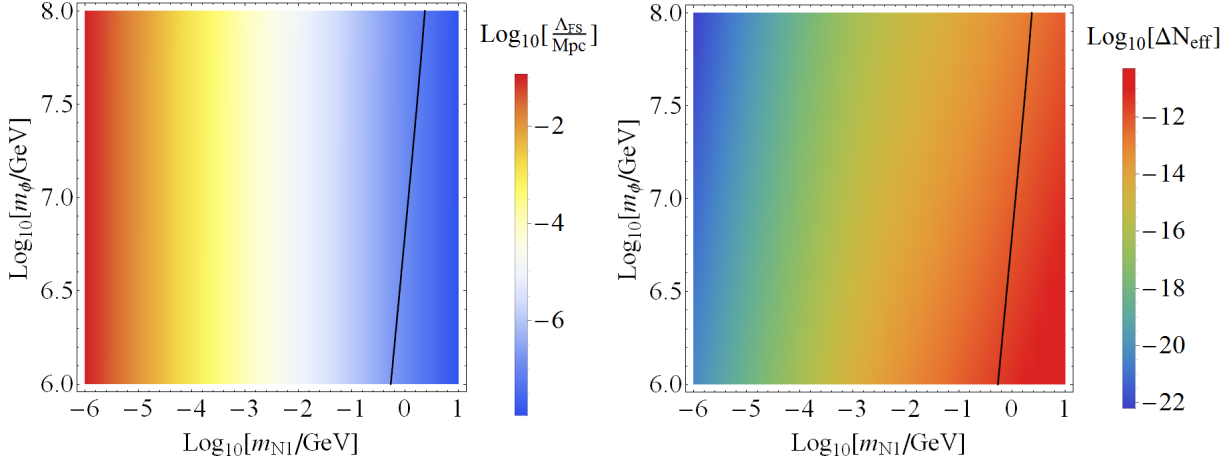
Figure 6.5: The observables, Λ_{FS} (left) and ΔN_{eff} (right) as a function of m_ϕ and m_{N_1}, for $\langle\phi\rangle = 100$ PeV and a low reheat temperature, $T_{RH} = 10^9$ GeV, corresponding to IR dominated production. The black lines denote where N_1 comprises all of dark matter.

Boltzmann equations and collision terms are again presented in appendix A.2.

This freeze-in of ϕ and subsequent decay to N_1 is illustrated in figure 6.6. We illustrate this process for two different choices of the coupling x_1, which controls the branching fraction into $\phi \to N_1 N_1$ and therefore the final dark matter abundance. The plot shows two distinct features as the coupling gets larger: (i) a larger abundance of N_1, consistent with $\text{Br}(\phi \to N_1 N_1) \propto x_1^2$, and (ii) a more rapid depletion of ϕ, since a larger x_1 also results in a larger ϕ decay width. Thus, the final dark matter abundance is set by the freeze-in abundance of ϕ, which depends on T_{RH}, and the branching fraction $\phi \to N_1 N_1$, which depends on the x_1 coupling, with a larger value of either parameter resulting in a larger abundance [3]. This behavior is also illustrated in figure 6.7, which shows how the dark matter relic abundance depends on the values of these parameters. The black curve denotes the combinations that result in the correct relic abundance $\Omega_{N_1} h^2 = 0.12$; the curve changes slope around $x_1 = 1$ as ϕ switches from decaying dominantly into $N_{2,3}$ at lower values of x_1 to decaying primarily into N_1 at higher values. Thus, we see that even when both ϕ and N_1 are absent in the early Universe, the desired dark matter abundance can be built up with a sufficiently high reheat temperature to produce ϕ from freeze-in and an appropriate coupling x_1 to convert a fraction of the ϕ population into N_1. Analytical results for the frozen-in abundance of N_1 are presented in appendix A.2.3

In this scenario, ϕ is fairly long-lived since its decay width is suppressed due to the small effective couplings $\sim 2x_i\langle\phi\rangle/M_*$ to the sterile neutrinos. Thus, its decay produces

---

[3]Note that neither the UV freeze-in of ϕ nor the branching fraction into N_1 is sensitive to m_ϕ as long as $m_\phi \gg m_{N_i}$, hence the exact value of this parameter is irrelevant.
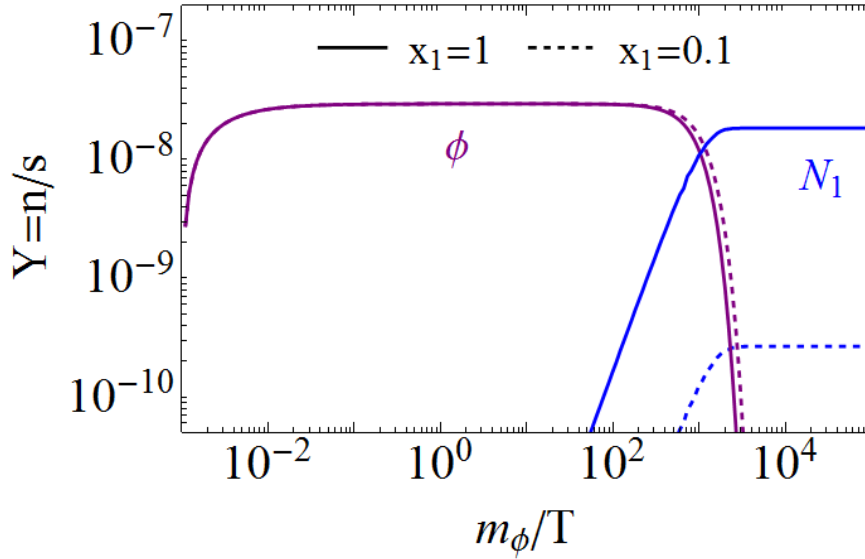
Figure 6.6: Evolution of the yields of ϕ and N_1 in the early Universe, for some fixed m_ϕ. Here we have fixed $T_{RH} = 10^{10}$ GeV and $\langle\phi\rangle = 100$ PeV, and show the evolution for two different values of x_1.

N_1 particles with energies of order m_ϕ at late times, when the temperature of the ambient bath is significantly lower. This behavior is already visible in the left panel of figure 6.7, where we see that $E_{N_1} \sim p_{N_1} \sim m_\phi \gg T$ at the time of production (*i.e.* where the ϕ yield drops). The ϕ lifetime can be extended by suppressing these effective couplings, which can be accomplished by lowering either $\langle\phi\rangle$ or x_i, which results in warmer dark matter. In figure 6.8, we plot the free streaming length Λ_{FS} and the contribution to the effective number of relativistic degrees of freedom $\Delta N_{\text{eff}}(\text{BBN})$ for these parameters. On both plots, we set the relic density to the correct value by appropriately choosing T_{RH}; some contours of the required T_{RH} values are shown on the plots as solid lines. Both plots show that dark matter becomes hotter as these parameters are lowered; however, in the shaded region, the correct relic density cannot be achieved without reheating above the GUT scale, where our theory needs to be UV completed, hence the "hot" regions in the bottom left corners of the plots are not accessible. In the allowed region, we see that it is possible for dark matter produced in this scenario to be warm, and $\Delta N_{\text{eff}} \lesssim 10^{-4}$.

6.3.3 Scenario III: ϕ in equilibrium, supersymmetry

This supersymmetric extension of Scenario I introduces new particles and interactions that can contribute to the production of N_1. Here, we assume that ψ (the fermionic superpartner
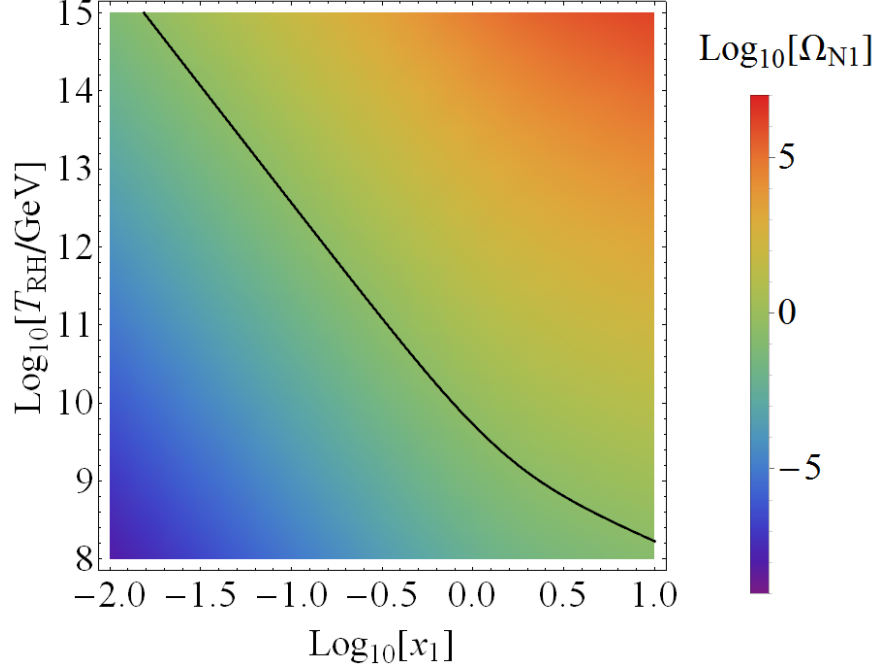
Figure 6.7: The dark matter relic abundance Ω_{N_1} as a function of the coupling x_1 and the reheat temperature T_{RH}; the black curve denotes the combinations that result in the correct relic abundance $\Omega_{N_1} h^2 = 0.12$. Here, we have set $\langle \phi \rangle = 100$ PeV.

of ϕ) is in equilibrium in the early Universe via the supersymmetric counterparts of the interactions that keep ϕ in equilibrium, and decay away rapidly once out of equilibrium. Overall, the processes that contribute to dark matter production in this scenario are

$$\text{UV:} \quad \phi\phi \to N_1 N_1, \quad \phi\psi \to \tilde{N}_1 N_1, \quad \psi\psi \to \tilde{N}_1 \tilde{N}_1$$
$$\text{IR:} \quad \phi \to N_1 N_1, \quad \phi \to \tilde{N}_1 \tilde{N}_1, \quad \tilde{N}_1 \to \psi N_1. \tag{6.30}$$

Note that we do not consider the UV process $\phi\phi \to \tilde{N}_1 \tilde{N}_1$ that arises from the soft term proportional to A_η from equation 6.7 as it only turns on at relatively low temperatures (after supersymmetry is broken), whereas we do consider its IR counterpart $\phi \to \tilde{N}_1 \tilde{N}_1$, which can be important if A_η is comparable to or larger than m_ϕ. The relevant Boltzmann equations and collision terms are presented in appendix A.3.

In this scenario, ϕ and ψ are in equilibrium, whereas N_1 and $\tilde{N}_1$ freeze-in. ϕ and $\tilde{N}_1$ both decay (in and out of equilibrium respectively), leading to a period of IR freeze-in for N_1. This process is illustrated in figure 6.9, where we plot the evolution of the yields of N_1 and $\tilde{N}_1$. Note that three distinct phases of N_1 production are clearly visible in the plot. An early UV freeze-in phase occurs at $m_\phi/T \leq 10^{-4}$; here, the N_1 and $\tilde{N}_1$ production mechanisms are identical, hence their abundances trace the same curve. Next, a second
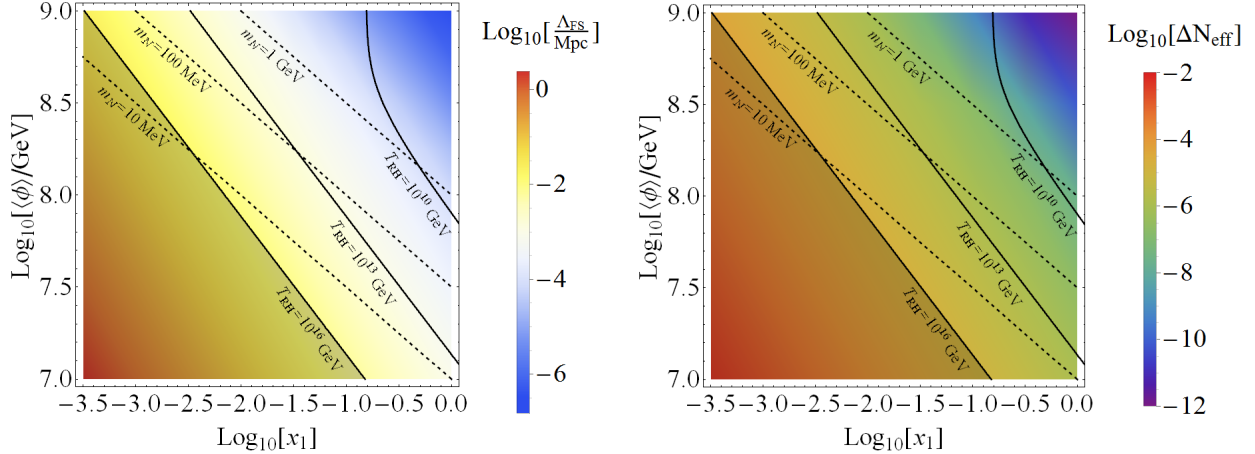
Figure 6.8: The free streaming length Λ_{FS} (left panel) and the contribution to the effective number of relativistic degrees of freedom at BBN (right panel). The dashed lines show contours of m_{N_1}. In these plots, the correct relic density is achieved by appropriately choosing T_{RH}; some contours of the required T_{RH} are shown as solid curves. The shaded regions are not accessible since the required T_{RH} here is greater than the GUT scale, requiring the theory studied here to be UV completed.

bump in N_1 abundance occurs around $m_\phi/T \sim 1$ from ϕ decay. Finally, there is another bump corresponding to contributions from $\tilde{N}_1$ decay at late times, around $m_\phi/T \sim 10^4$, reflecting the relatively long lifetime of $\tilde{N}_1$. Depending on the choice of parameters, these three different production mechanisms can contribute different amounts of dark matter. UV production is dominant when T_{RH} is large; in this case, equal amounts of N_1 and $\tilde{N}_1$ are produced, resulting in dark matter made up equally of N_1 from UV freeze-in and $\tilde{N}_1$ decay. If T_{RH} is low, IR production is dominant; in this case, N_1 can be produced directly from ϕ decay or from the decay of $\tilde{N}_1$ produced via $\phi \to \tilde{N}_1 \tilde{N}_1$. For these two decay widths, $\Gamma(\phi \to N_1 N_1) \propto \eta^2_{1eff} m_\phi$ and $\Gamma(\phi \to \tilde{N}_1 \tilde{N}_1) \propto \eta^2_{1eff} A^2_{\eta_1}/m_\phi$, hence the former (latter) contribution dominates for $m_\phi > A_{\eta_1}$ ($m_\phi < A_{\eta_1}$). In the latter case, it is therefore possible for the entire dark matter abundance to originate from $\tilde{N}_1$ decay.

While the free-streaming length and ΔN_{eff} contribution from UV production and ϕ decay follow the same patterns as in Scenario I, the presence of a new production channel in the form of $\tilde{N}_1$ decay opens additional possibilities. Because $\tilde{N}_1 \to \psi N_1$ is the *only* available decay channel, suppressing the corresponding coupling can make $\tilde{N}_1$ extremely long-lived and the subsequently produced N_1 extremely hot (note that this is not possible with ϕ, since its lifetime is determined by other decay channels such as $\phi \to N_{2,3} N_{2,3}$). To illustrate this, we plot the free-streaming length as a function of N_1 and $\tilde{N}_1$ masses in figure 6.10. The solid (dotted) line denotes combinations resulting in N_1 making up 100%(10%) of the total dark matter abundance (for $\langle \phi \rangle = 100$ PeV, $T_{RH} = 10^{15}$ GeV). The figure shows that the
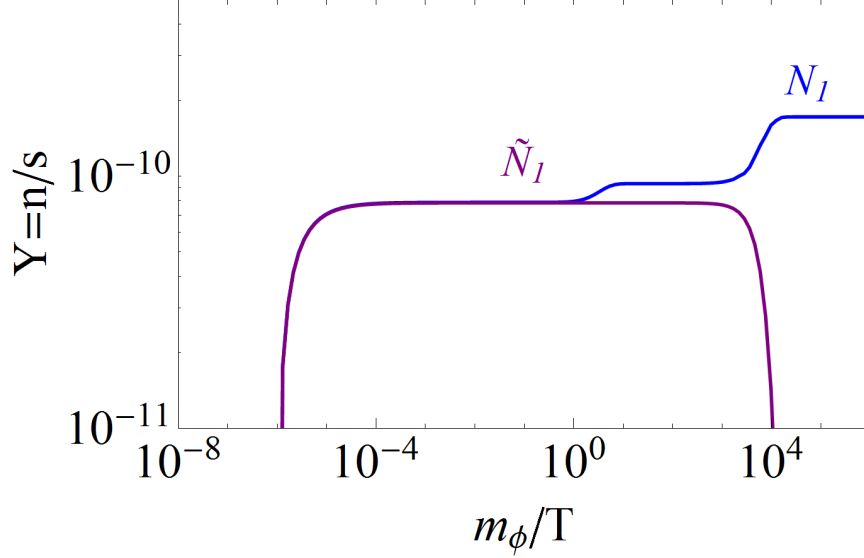
Figure 6.9: The yields of N_1 (blue) and $\tilde{N}_1$ (purple) during freeze-in. Three distinct dark matter production phases are visible: an early UV freeze-in of both N_1 and $\tilde{N}_1$, ϕ decay, and $\tilde{N}_1$ decay. Here we have set $T_{RH} = 10^{12}$ GeV, $m_\phi = 1$ PeV, $m_{\tilde{N}_1} = 16$ PeV, $\langle \phi \rangle = 100$ PeV, and $m_{N_1} = 40$ MeV. For this plot we have assumed that A_{η_1} is negligible, so that there is no appreciable production of $\tilde{N}_1$ from $\phi \to \tilde{N}_1 \tilde{N}_1$.

parameter space allows for hot (inconsistent with structure formation), warm, or cold dark matter. Constraining $\Lambda_{FS} \lesssim 0.1$ Mpc, we find $\Delta N_{\text{eff}} \lesssim 10^{-4}$ if N_1 comprises all of dark matter; this is consistent with Scenario II above and with results in [71], which found that large ΔN_{eff} during BBN is inconsistent with free-streaming length constraints.

An interesting possibility worth entertaining is the case where late decays of $\tilde{N}_1$ result in only a tiny fraction ($< 1\%$; see $e.g.$ [124]) of (extremely hot) dark matter, while the rest of the dark matter (either Higgsino or N_1 from ϕ decay) is cold. In this case, this subdominant population of N_1 from $\tilde{N}_1$ decays is not subject to any free-streaming constraints (since the bulk of dark matter is cold), but can still provide a large contribution to ΔN_{eff} if $\tilde{N}_1$ is sufficiently heavy and long-lived (but decays before LSP decoupling). We find that these conditions are satisfied for a heavy $\tilde{N}_1$ and an extremely light N_1. However, a heavy $\tilde{N}_1$ requires an even heavier ϕ (if $\tilde{N}_1$ is to be produced via $\phi \to \tilde{N}_1 \tilde{N}_1$), which does not allow enough time for sufficient IR freeze-in of $\tilde{N}_1$, as this process ends once ϕ goes out of equilibrium. Alternatively, one can consider dominantly UV production of $\tilde{N}_1$ via $\psi \psi \to \tilde{N}_1 \tilde{N}_1$; however, this goes through the coupling η_1, which is proportional to m_{N_1}, hence raising η_1 to increase $\tilde{N}_1$ production also raises m_{N_1}, reducing ΔN_{eff}. Therefore, while this idea is in principle feasible, we find that the relations between various parameters imposed by our
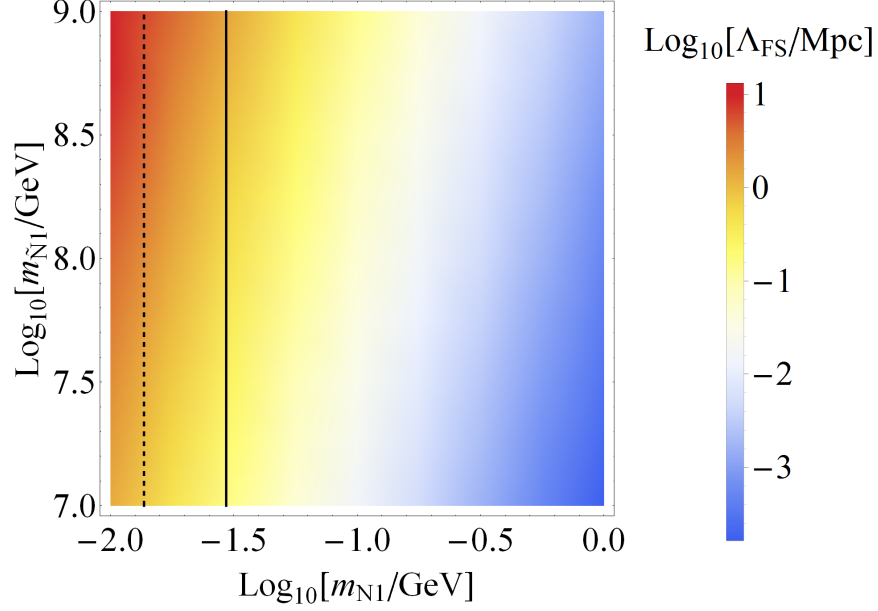
Figure 6.10: Free streaming length Λ_{FS} . The solid (dotted) line denotes where N_1 makes up 100% (10%) of the total dark matter abundance (for $\langle\phi\rangle = 100$ PeV, $T_{RH} = 10^{15}$ GeV). Cold, warm, and hot dark matter are all viable options in this scenario.

framework do not allow us to fully realize this attractive possibility, and we obtain at most $\Delta N_{\text{eff}} \sim 10^{-3}$ in this scenario in our framework.

6.3.4 Scenario IV: ϕ freezes in, supersymmetry

In this section, we will assume that the heavier sterile neutrinos N_2, N_3 are sufficiently heavy that the entropy dilution from their decay is negligible. This scenario is a supersymmetric extension of Scenario II, and therefore shares many of the features from Scenarios II and III above. For the freeze-in of ϕ, compared to Scenario II we have the following additional interactions:

$$\tilde{L}_i\, H \to \tilde{N}_{2,3}\, \phi\,, \qquad L_i\, \tilde{H} \to \tilde{N}_{2,3}\, \phi\,, \qquad \tilde{L}_i\, \tilde{H} \to N_{2,3}\, \phi\,,$$

since the charged and neutral Higgsinos and sleptons are also present in the thermal bath. Similar processes also lead to UV production of ψ, which subsequently decay as $\psi \to \tilde{L}_i\, H\, N_{2,3}$ or $\psi \to \tilde{N}_{2,3}\, N_{2,3}$. Again, one must ensure that the decays of all supersymmetric particles occur before Higgsino decoupling. As ϕ and ψ are absent in the early Universe, there is no direct UV production of N_1 or $\tilde{N}_1$, and dark matter is produced via the decay processes

$$\phi \to N_1\, N_1\,; \quad \phi \to \tilde{N}_1\, \tilde{N}_1\,, \quad \tilde{N}_1 \to \psi\, N_1\,. \tag{6.31}$$
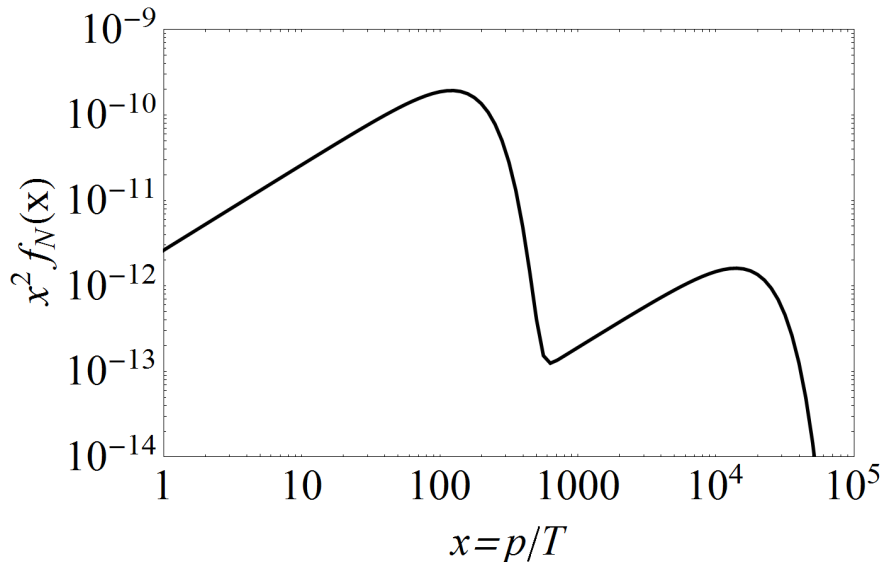
70

Figure 6.11: Phase space distribution for a case with comparable scalar and sterile sneutrino decay contributions. In this plot, the parameters are: $m_N = 1$ GeV, $m_{\tilde{N}_1} = 10^8$ GeV, $m_\phi = 10^9$ GeV, $m_\psi = 10^7$ GeV, $A_{\eta 1} = 10^9$ GeV, $\langle \phi \rangle = 10^9$ GeV.

The full set of Boltzmann equations and collision terms are presented in appendix A.4.

Here, ϕ does not have any other significant interactions and therefore decays primarily to N_i and $\tilde{N}_i$, while the presence of N_i allows for late decays into extremely energetic N_1. The phase space distribution of N_1 produced in this manner is shown in figure 6.11, with the parameter choices as described in the plot caption. We see that there are two distinct bumps in this particular distribution: the lower momentum one corresponds to N_1 produced directly from ϕ decays, while the higher momentum bump corresponds to the contribution from $\tilde{N}_1$ decays. The two bumps peak at $x \sim 100$ and $x \sim 10^4$, reflecting that both arise from late decays where the mass of the decaying particle is several orders of magnitude higher than the temperature of the ambient thermal bath. In such scenarios, we therefore see that we can get extremely nontrivial phase space distributions of warm/hot dark matter, which might prove to be of interest for various considerations.

As in the previous scenarios, the correct relic density can be obtained with appropriate choices of the various parameters, combining the multiple production mechanisms for dark matter; since the patterns are mostly the same as in Scenarios II and III, we do not repeat those details again. Given the energetic nature of the dark matter particles produced from out of equilibrium decays, it is more interesting to study the observational properties of such a population. As in Scenario III, cold, warm, and hot dark matter are all possible in this scenario. In addition, we find that contributions to $\Delta N_{\rm eff}$ at BBN with a subdominant (1%) fraction of dark matter, as discussed in the final paragraph in Scenario III, has better
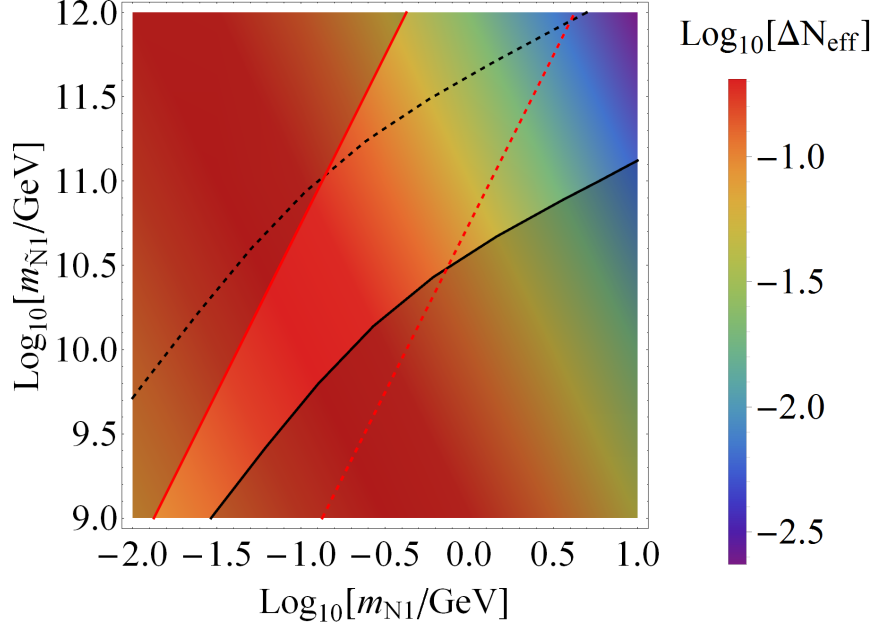
Figure 6.12: Relic density and $\Delta N_{\rm eff}$ (BBN) for $T_{RH} = 10^{15}$ GeV and $\langle\phi\rangle = 0.1 m_{\tilde{N}_1}$. In this plot, ϕ decays dominantly to $\tilde{N}_1$, and the decays of $\tilde{N}_1$ populate N_1. Solid (dashed) black curves denote where N_1 accounts for 100%(1%) of dark matter; the solid (dashed) red lines denote where the decay occurs at the decoupling temperature of a Higgsino of mass 200 (2000) GeV. Shaded regions are disallowed because of overclosure (bottom right) or N_1 decaying after a 200 GeV Higgsino freezes out (top left).

prospects in this scenario as ϕ can decay to N_1 and $\tilde{N}_1$ out of equilibrium. For a proof of concept, we focus on the case where $A_{\eta_1} \gg A_{\eta_{2,3}}$, m_ϕ, so that the entire population of ϕ that freezes in decays into $\tilde{N}_1$. In this case, the entire population of N_1 is produced from $\tilde{N}_1$ decays. The remainder (dominant fraction) of dark matter should then be accounted for by some other component, $e.g.$ the Higgsino. We plot the $\Delta N_{\rm eff}$ and relic density obtained with these approximations in figure 6.12. The color coding denotes the size of $\Delta N_{\rm eff}$; the black curves and red lines denote contours of relic density and decoupling temperature respectively, as explained in the caption. Shaded regions are disallowed because of overclosure (bottom right) or N_1 decaying after a 200 GeV Higgsino freezes out (top left). In the allowed (non-shaded) region, even imposing that N_1 make up less than 1% of dark matter ($i.e.$ region above the dashed black curve), we see that it is possible to get $\Delta N_{\rm eff} \approx 0.1$, which is an extremely interesting feature that can potentially be probed by future measurements.

6.4 Summary

In this chapter, we have investigated cosmological aspects of light ($\lesssim$ GeV scale) sterile neutrino dark matter produced from the freeze-in mechanism. Given that such a dark matter candidate interacts feebly with the SM and thus has no promising indirect or direct search strategies, such cosmological aspects represent the most phenomenologically interesting features of such a candidate. We perform this study in a comprehensive framework that includes many interesting variations: production from a scalar in or out of equilibrium with the thermal bath in the early Universe, via UV or IR freeze-in, and with or without supersymmetry. Under this broad approach, we find many novel features. Our findings can be summarized as follows:

- Relic density: The relic abundance required to explain all of dark matter can be achieved in all scenarios considered. Production can occur dominantly through UV freeze-in, IR freeze-in from decays of the scalar ϕ in or out of equilibrium with the SM bath, or through decays of a sterile sneutrino in supersymmetric setups; more generally, any combination of these processes can also result in the observed relic density.

- Free-streaming length: We find that sterile neutrino dark matter produced via freeze-in can be cold, warm, or hot, depending on the dominant production mechanism and choice of parameters. Dark matter from UV production or decay of ϕ in equilibrium with the thermal bath is generally cold (Scenario I), while late out of equilibrium decay of ϕ or the sterile sneutrino $\tilde{N}_1$ can result in warm or hot dark matter (Scenarios II, III, IV). Such scenarios can be of great interest from the point of view of structure formation.

- Phase space distribution: Given the interplay of multiple production mechanisms for dark matter, its momentum distribution can be extremely varied and nontrivial. UV and IR freeze-in produce dark matter with slightly different momentum distributions (figure 6.4); likewise, dark matter produced from decays of ϕ (in or out of equilibrium) and $\tilde{N}_1$ can have significantly different distributions if the times and energy scales of decay are very different (see figure 6.11). Note that such distributions are possible only because the N_1 abundance freezes in and only has feeble SM and self interactions, hence different components produced from different mechanisms do not mix but maintain their individual phase space distributions. Such features are not present in the traditionally studied dark matter candidates that freeze out of equilibrium.

- Contributions to ΔN_{eff} during BBN: Extremely energetic dark matter particles in the early Universe can mimic dark radiation, contributing to the effective number of

73

relativistic degrees of freedom ΔN_{eff}. For GeV scale sterile neutrinos, we find that such contributions are more likely at BBN than CMB since they redshift and become non-relativistic at later times. We find that ΔN_{eff} is generally restricted to negligible values ($\lesssim 10^{-4}$) by free-streaming length constraints if N_1 makes up all of dark matter (*e.g.* figure 6.8). However, free-streaming constraints can be circumvented if N_1 makes up only a subdominant fraction ($\lesssim 1\%$) of dark matter, and in this case we find that $\Delta N_{\text{eff}} \sim \mathcal{O}(0.1)$ can indeed be realized consistent with all other constraints (see figure 6.12).

Finally, while we performed the above study in a specific framework, so that many of the quantitative results are model-dependent, we emphasize that the general features discussed here represent the most observable aspects of frozen-in sterile neutrinos, and are more broadly applicable to any framework that has such a dark matter candidate.

Chapter 7

Experimental Hints

Astrophysical signatures of dark matter interactions, coupled with theoretical and observational input from other areas of particle physics, can provide crucial insights into the nature of physics beyond the SM. However, while the existence and macroscopic properties of dark matter in our Universe have been well established, its microscopic properties continue to remain elusive. Compelling theoretical arguments dictate that dark matter is most likely composed of weakly interacting massive particles (WIMPs), predicting a GeV-TeV mass scale for dark matter, although supporting observational evidence has so far failed to materialize. Interestingly, some recent observations hint at dark matter beyond this narrow GeV-TeV window, indicating that the structure of dark matter and BSM physics might be very different from what was envisioned.

One such observation is the IceCube neutrino observatory's detection of 37 neutrino events in the energy range from 30 GeV to 2 PeV, disfavoring a purely atmospheric explanation at 5.7σ [18]. In particular, IceCube has reported 3 neutrino events above 1 PeV. Strongly incompatible with traditional astrophysical processes, these have been shown to be compatible with the decay of heavy, long lived particles with lifetimes of about 10^{27} seconds that constitute some or all of dark matter [125, 126, 127, 128, 129, 130, 131, 132, 133, 134, 135]. A dark matter interpretation of these events, however, poses several theoretical inconveniences: Why should we expect new physics at the PeV scale? Why should a PeV scale particle be so long-lived? What sets its relic density? Why should it show up in neutrinos? Given the dearth of beyond the SM candidates at the PeV scale, a theoretically motivated framework that also fits into the broader particle physics picture would be extremely appealing.

Another observation, made independently by two groups, is the discovery of an unidentified X-ray line at $E_\gamma \approx 3.5$ keV in the stacked X-ray spectra of 73 galaxy clusters measured by XMM-Newton [16] and in the X-ray spectra of the Andromeda galaxy and the Perseus galaxy cluster [17]. A dark matter interpretation of these observations is plagued by many

unresolved questions, such as possible contamination from potassium lines [136, 137, 138] as well as inconsistency with stacked observations of dwarf spheroidals [139] and galaxy spectra [140] (although greater compatibility is reported with observations of the Milky Way [141, 142]). Despite these concerns, we entertain the possibility that these observations can be explained by a monochromatic line from the decay of a 7 keV dark matter particle. Unlike the IceCube PeV neutrinos, there exists an extremely well-motivated keV scale dark matter candidate in the form of a sterile neutrino, whose decay into an active neutrino and an X-ray photon with energy equal to half its mass has long been heralded as its smoking gun signature. Sterile neutrinos are essential ingredients of see-saw models of neutrino masses, and while their masses could, a-priori from theory, lie anywhere from the eV to the GUT scale, forming a significant fraction of dark matter while remaining consistent with X-ray and Lyman-alpha measurements constrains them to be at the keV scale.

In this chapter (based on [15]), we show that one or both of these signals can naturally arise from an extended supersymmetric neutrino sector. The framework is a simple extension of the model presented in chapter 5, where it was shown that if the right-handed neutrinos are charged under some new symmetry $U(1)'$, broken by the PeV scale vacuum expectation value (vev) of a scalar field, active neutrino masses consistent with data and keV-GeV mass sterile neutrinos that can form part or all of dark matter can be realized without the need for any unnaturally small parameters in the theory.

The realization of the 3.5 keV line from a sterile neutrino component of dark matter in this framework is straightforward. In addition, we will see that a straightforward extension of the neutrino sector using the same $U(1)'$ symmetry and structure employed for neutrino masses can result in a PeV scale dark matter candidate whose decays are compatible with the high energy neutrino events at IceCube. It is interesting to note that a mixture of cold and warm dark matter components might also be favorable for solving some of the small scale problems in cosmology [33, 34].

Here, we do not aim to build a complete model of PeV scale supersymmetry – this would bring in model-dependent details and complexities that are irrelevant to the task at hand. We simply intend to demonstrate that our framework can naturally accommodate the IceCube PeV neutrinos and the 3.5 keV X-ray line; for this reason, we also do not pursue detailed scans over parameters, and the benchmark values presented here should not be interpreted as the "best-fit" ones. The greatest virtue of this exercise lies not in obtaining best fits or building a complete model but in placing the two signals in perspective within a broader particle physics framework, where they are not isolated observational curiosities but are connected to outstanding issues in the neutrino and Higgs sectors. Finally, although unifying such disparate scales as the keV and PeV into a single simple framework appears

Supermultiplet	spin 0, 1/2	$U(1)'$	Remarks
$\mathcal{N}_i$	$\tilde{N}_i, N_i$	+1	N_i sterile neutrinos
Φ	ϕ, ψ_ϕ	-1	$\langle\phi\rangle \sim$PeV, breaks $U(1)'$
$\mathcal{X}$	X, ψ_X	+5	$m_X \sim$PeV, dark matter
$\mathcal{Y}$	Y, ψ_Y	-5	$U(1)'$ partner of $\mathcal{X}$

Table 7.1: Field content, notation, and $U(1)'$ charge assignments for the new multiplets introduced in the neutrino sector of the model. These lead to the higher-dimensional operators in the superpotential in equation 7.1.

extremely appealing, it should be kept in mind that these two signals are by no means necessary ingredients in the theory; indeed, both, one, or neither of them can be realized in the model with appropriate choices of fields and parameters.

7.1 The Model

In this section we present our model of the supersymmetric neutrino sector, which aims to realize active neutrino masses consistent with oscillation data, a keV sterile neutrino dark matter candidate, and a PeV scale dark matter candidate without any unnaturally small parameters in the theory. This is an extension of the model in chapter 5. As previously motivated, we take the scale of supersymmetry breaking to be around $\mathcal{O}(1-100)$ PeV. This means that all dimensionful parameters obtained after supersymmetry breaking, such as masses and vevs, are expected to be at this scale.

In order to obtain neutrino masses, three SM-singlet sterile neutrinos N_i are introduced. Although the N_i are singlets under the SM gauge group, they are unlikely to be singlets under all symmetries of nature, as this would naturally place their masses at the Planck scale or the GUT scale, contrary to what is phenomenologically desirable. We therefore posit that the N_i are charged under some new symmetry of nature (for concreteness, a $U(1)'$). The N_i are coupled to a single exotic field ϕ of equal and opposite $U(1)'$ charge to form $U(1)'$ singlets, which can then be coupled to SM fields.

With the IceCube PeV neutrinos in mind, we also introduce a new field X, a SM singlet scalar with a PeV scale mass and appropriately charged under the $U(1)'$ to be sufficiently long-lived to form a component of dark matter. It is likewise coupled to another field Y (which carries lepton number) to form a $U(1)'$ singlet. Given the new symmetry $U(1)'$, this is the most straightforward extension of the model to incorporate additional fields.

Since the theory is supersymmetric, each of these fields resides in a chiral supermultiplet;

the field content and notation are summarized in Table 7.1. With the additional assumption of R-parity conservation[1], these lead to the following non-renormalizable terms in the superpotential that are relevant to our study:

$$\mathcal{W} \supset \quad \frac{\xi_{ij}}{M_*} L_i H_u \mathcal{N}_j \Phi + \frac{\alpha_i}{M_*} L_i H_u \mathcal{X} \mathcal{Y} + \frac{\eta_i}{M_*} \mathcal{N}_i \mathcal{N}_i \Phi \Phi + \frac{\lambda_1}{M_*} \mathcal{X} \mathcal{X} \mathcal{Y} \mathcal{Y} + \frac{\beta_i}{M_*} \mathcal{N}_i \Phi \mathcal{X} \mathcal{Y}$$
$$+ \frac{1}{5!} \frac{\lambda_2}{M_*^3} \mathcal{X} \Phi^5 + \frac{1}{5!} \frac{\lambda_3}{M_*^3} \mathcal{Y} \mathcal{N}_i^5. \tag{7.1}$$

All couplings are written as dimensionless numbers and expected to be $\mathcal{O}(1)$. The N_i basis is chosen such that the third term in equation 7.1 is diagonal. M_* is the scale at which this effective theory of non-renormalizable operators needs to be UV completed with new physics, such as the scale of grand unification M_{GUT} or the Planck scale M_P.

Obtaining Dirac and Majorana masses for the sterile neutrinos N_i in order to recover the see-saw mechanism requires the scalar component ϕ of Φ to obtain a vev, thereby breaking the $U(1)'$ symmetry. We assume that ϕ obtains a PeV scale vev from the supersymmetry breaking sector (without delving into details of how exactly this might be realized, which is tangential to our main purpose). In addition, we also assume that the fields in the $\mathcal{X}, \mathcal{Y}$ and Φ multiplets all get PeV scale masses. This setup has the following phenomenological consequences:

7.1.1 Neutrino Masses

With ϕ obtaining a vev at the PeV scale and H_u acquiring a vev from electroweak symmetry breaking, the first and third terms in the superpotential in equation 7.1 lead to the following active-sterile Dirac masses and sterile Majorana masses in the neutrino sector (flavor indices suppressed for simplicity):

$$m_D = \frac{\xi \langle \phi \rangle \langle H_u^0 \rangle}{M_*}, \qquad m_M = \frac{\eta \langle \phi \rangle^2}{M_*}. \tag{7.2}$$

The see-saw mechanism then gives the following sterile and active neutrino mass scales:

$$m_s = m_M = \frac{\eta \langle \phi \rangle^2}{M_*}, \quad m_a = \frac{m_D^2}{m_M} = \frac{\xi^2 \langle H_u^0 \rangle^2}{\eta M_*}, \tag{7.3}$$

---

[1]Because both $\mathcal{N}_i$ and $\mathcal{Y}$ carry lepton number, R-parity conservation forbids terms like $\mathcal{N}_i \Phi$ and $\mathcal{X} \mathcal{Y}$ in the superpotential, just like $L_i H_u$.

which also determines the mixing angle between the active and sterile sectors:

$$\theta \approx \sqrt{\frac{m_a}{m_s}} = \frac{\xi \langle H_u^0 \rangle}{\eta \langle \phi \rangle}. \tag{7.4}$$

With $\langle \phi \rangle \sim 1-100\,\mathrm{PeV}$, $M_* = M_{GUT} = 10^{16}\,\mathrm{GeV}$, $\tan\beta = 2\,(\langle H_u^0 \rangle = 155.6\,\mathrm{GeV})$, and $\mathcal{O}(1)$ values of ξ and η, this framework produces active neutrino masses that fit oscillation data and sterile neutrinos with $\mathcal{O}(\mathrm{keV\text{-}GeV})$ masses, which are compatible with dark matter and cosmological observations (see 5 for more details).

7.1.2 Sterile Neutrinos and Dark Matter

The three sterile neutrinos N_i naturally have masses at the keV-GeV scale in this framework. We require the lightest one, N_1, to be a dark matter candidate with a keV scale mass in order to explain the 3.5 keV X-ray signal. However, several recombination era observables [37, 102, 103, 103] constrain the two heavier sterile neutrinos N_2, N_3 to decay before BBN, forcing $\tau_{N2,N3} \lesssim 1\mathrm{s}$ and consequently $m_{N2,N3} \gtrsim \mathcal{O}(100)$ MeV. This mass hierarchy between m_{N1} and $m_{N2,3}$ requires a similar hierarchy between ξ_{ij} and η_i values, necessitating some tuning of parameters. This is illustrated in benchmark A (section 5.4.1) of chapter 5.

As N_1 couples extremely weakly to the SM fields and is never in thermal equilibrium in the early Universe, its relic abundance is not set by thermal freeze-out. It is produced instead through active-sterile oscillation at low temperatures, (DW mechanism). A combination of X-ray bounds and Lyman-alpha forest data now rule out the prospect of all of dark matter consisting of N_1 produced via the DW mechanism; however, it can still constitute a significant fraction of the dark matter abundance (this will be further discussed in Section 7.2.2). This is desirable for us, since the remaining dark matter can come from the PeV sector.

7.1.3 PeV Scale Dark Matter

Our PeV dark matter candidate is a SM singlet scalar X that carries a $U(1)'$ charge (see Table 7.1). In general, a PeV scale dark matter candidate presents two caveats. First, obtaining the correct relic density through the well-known thermal freeze-out mechanism requires a large annihilation cross-section that comes into conflict with unitarity limits [143], so that freeze out of a PeV scale particle overcloses the Universe. Hence one has to ensure that the candidate is never in thermal equilibrium and build up its abundance through some other mechanism. Second, since the decay rate of a particle is in general proportional to its mass, an unstable PeV scale particle is generically far too short-lived to be a dark matter candidate, and appropriate measures need to be put in place to stabilize it against rapid

decay. We will see that the new $U(1)'$ symmetry in our theory can be used to address both of these issues.

In light of the unitarity bound mentioned above, some further assumptions need to be made about the superpartners that freeze out of the thermal bath, as we take supersymmetry to be at the PeV scale. One possibility is to make the lightest supersymmetric particle (LSP) sufficiently light that the thermal freeze-out abundance does not overclose the Universe. Another is to have all superpartners decay into SM states through R-parity violating (RPV) interactions. In the model presented here, we choose the former option despite the clear need to tune parameters in order to achieve this, as the latter would involve the introduction of several RPV operators in our model, which require careful treatment beyond the scope of this work. To this end, the LSP is chosen to be a Higgsino at $\sim 800\,\text{GeV}$, which would make up about half of the dark matter abundance.

Production of X

Since X is charged under the $U(1)'$, there are no renormalizable terms in the superpotential that connect it with SM fields. The lowest dimension term allowed, which must be both a SM singlet and a $U(1)'$ singlet, is the term $\frac{\alpha_i}{M_*} L_i H_u \mathcal{X} \mathcal{Y}$ (see equation 7.1); this leads to the following production processes for X from the thermal bath:

$$l\, h \to X\, \psi_Y, \quad l\, \tilde{H} \to X\, Y, \quad \tilde{l}\, \tilde{H} \to X\, \psi_Y. \tag{7.5}$$

Here l denotes both charged leptons and neutrinos, and h denotes both neutral and charged higgses, and likewise for their superpartners $\tilde{l}$ and $\tilde{H}$. The above processes are suppressed by M_* and therefore not strong enough to bring X into equilibrium. Rather, since these interactions are extremely feeble, the abundance of X gradually builds up via the process of freeze-in [28] as long as the processes remain kinematically feasible. Given the nonrenormalizable operators that leads to these interactions, the interaction cross sections scale as $\sim s/M_*^2$, where s is the center of mass energy of the annihilation process, and the production rate is proportional to the temperature of the Universe, being the greatest at the earliest times.

The same processes also result in freeze-in abundances of Y, ψ_X, and ψ_Y. Assuming $m_{\psi_X} > m_Y > m_{\tilde{H}}, m_X$ and $m_{\psi_Y} > m_X$, these particles then decay via

$$\psi_X \to Y\, l\, h, \quad Y \to X\, l\, \tilde{H}, \quad \psi_Y \to X\, l\, h, \tag{7.6}$$

converting the abundances of Y, ψ_Y, and ϕ_X into X abundance. Taking all these contribu-

tions into account, we calculate the relic abundance of X to be approximately (in agreement with previously derived results in [30, 97, 98, 99])

$$\Omega_X h^2 \sim 0.12 \left(\frac{m_X}{10 \text{ PeV}}\right)\left(\frac{\alpha}{10^{-4}}\right)^2 \left(\frac{T_{RH}}{1.5 \times 10^{10} \text{ GeV}}\right)\left(\frac{10^{16} \text{ GeV}}{M_*}\right)^2 \tag{7.7}$$

where we have taken $\alpha = \alpha_i$ for simplicity. Therefore, with a sufficiently high reheat temperature T_{RH} and appropriate values of α, the PeV scale particle X could compose a significant fraction of dark matter.

Decay of X

Next, we must ensure that X has a lifetime much longer than the age of the Universe and the correct decay rate and channels to produce the neutrinos observed at IceCube. We have already chosen $m_{\psi Y}, m_Y > m_X$, hence the only term in the superpotential equation 7.1 that can cause X to decay is $\frac{1}{5!}\frac{\lambda_2}{M_*^3}\mathcal{X}\Phi^5$. Assuming $\langle\phi\rangle > m_\phi$, the leading decay process is $X \to \psi_\phi\psi_\phi$, coming from the Lagrangian term

$$\mathcal{L} \supset -\frac{\lambda_2}{12}\left(\frac{\langle\phi\rangle}{M_*}\right)^3 X\,\psi_\phi\,\psi_\phi\,. \tag{7.8}$$

Here we assume, for simplicity, that the decay $X \to \phi\phi$ or the decays from mixing with ϕ induced by the corresponding soft term $\frac{A_X}{M_*^3}X\phi^5$ that appears after supersymmetry breaking are subdominant (however, we have checked that these channels also give similar neutrino spectra to that from $X \to \psi_\phi\psi_\phi$). Assuming $m_{\psi_\phi}/m_X \ll 1$, this decay process has a lifetime

$$\tau_X \approx 10^{27} \text{ s} \left(\frac{1.5 \times 10^{-3}}{\lambda_2}\right)^2 \left(\frac{M_*}{10^{16} \text{ GeV}}\right)^6 \left(\frac{100 \text{ PeV}}{\langle\phi\rangle}\right)^6 \left(\frac{\text{PeV}}{m_X}\right). \tag{7.9}$$

The ψ_ϕ further decays as $\psi_\phi \to N\tilde{H}\nu$, $\psi_\phi \to N\tilde{H}^\pm l^\mp$ through an off-shell sterile sneutrino as a consequence of the $L_i H_u \mathcal{N}_j \Phi$ and $\mathcal{N}_i \mathcal{N}_i \Phi\Phi$ terms in the superpotential. The sterile neutrinos N then further decay through the standard sterile neutrino decay channels to produce additional active neutrinos.

As the decay lifetime required to fit the IceCube data is $\tau \sim 10^{27}$ s, equation 7.9 suggests that one can obtain the necessary lifetime for reasonable choices of parameters in the model (see section 7.2.1 below). Note the role of the $1/M_*^3$ suppression in obtaining such a long lifetime; this was the motivation behind the choice of the $U(1)'$ charge of $+5$ for $\mathcal{X}$. In appendix B we examine the lifetime of X for different couplings with ϕ and ψ, coming from different choices of $U(1)'$ charge. We find that $+5$ is the minimal charge required while still having an $\mathcal{O}(1)$ dimensionless coupling constant.

Couplings

$\underline{\xi_{ij}}$			$\underline{\eta_i}$	
3.53	-2.28	-1.19×10^{-5}	5.82×10^{-6}	$\alpha = 0.007$
1.02	-3.54	-1.99×10^{-5}	1.26	$\lambda_2 = 0.0002$
-0.65	-1.28	3.38×10^{-5}	1.67	

Masses

$\underline{m_a \ (\text{eV})}$	$\underline{m_s}$	
7.75×10^{-7}	7.00 keV	$m_X = 7$ PeV
0.0087	1.50 GeV	$m_{\psi_\phi} = 2$ PeV
0.049	2.00 GeV	$m_{\tilde{H}^0, \tilde{H}^\pm} = 800$ GeV

Dark Matter Properties

$m_{N_1} = 7$ keV	$m_X = 7$ PeV	$m_{\tilde{H}^0} = 800$ GeV
$\Omega_{N_1} h^2 = 0.03 \ (= 25\%)$	$\Omega_X h^2 = 0.03 \ (= 25\%)$	$\Omega_{\tilde{H}^0} h^2 = 0.06 \ (= 50\%)$
	$\tau_X = 3 \times 10^{27}$ s	

Table 7.2: Our choice of couplings in the superpotential (defined in Eq 7.1) and the resulting neutrino masses and dark matter properties. m_a and m_s denote the three active and sterile neutrino masses respectively. Along with these choices, we have set $\langle\phi\rangle = 110$ PeV, $M_* = M_{\text{GUT}} \ (= 10^{16}$ GeV$)$, $\tan\beta = 2$, and $T_{RH} = 10^{10}$ GeV.

7.2 Compatibility with Signals

In this section we demonstrate the compatibility of the IceCube neutrino and 3.5 keV X-ray line signals with the framework described in the previous section. As mentioned in the introduction of this chapter, one could incorporate neither, one, or both of these into the model with appropriate parameter choices. In this section we choose to include both, as a proof of principle that both can be incorporated simultaneously into the framework. To demonstrate this, we work with a specific choice of parameters, which are listed in Table 7.2; the active and sterile neutrino masses and relic abundances of various dark matter components that result from these choices are also listed. As stressed in the introduction, these are not best-fit points resulting from some scan but simply a judicious choice of parameters to achieve the desired results.

The choice $\tan\beta = 2$ is compatible with the measured Higgs mass $m_h = 125$ GeV with PeV scale superpartners. The cutoff scale M_* is chosen to be the scale of grand unification

M_{GUT} ($= 10^{16}$ GeV), so the framework is expected to be embedded in a grand unified theory. With $\langle \phi \rangle = 110$ PeV, the specified values of ξ_{ij} and η_i set the masses of sterile and active neutrinos (m_s and m_a respectively) via the see-saw mechanism. It can be seen that the entries are mostly $\mathcal{O}(1)$, except for the third column of ξ_{ij} and the first entry in η_i, which are $\mathcal{O}(10^{-5})$; as mentioned in Section 7.1.2, this hierarchy is made inevitable by the need for N_1 to be at the keV scale and $N_{2,3}$ to be at the GeV scale for consistency with cosmology. It is worth noting that although $\mathcal{O}(10^{-5})$ seems unnaturally small, such a small number is already realized in nature in the form of the electron Yukawa coupling. With these choices, the lightest sterile neutrino N_1 has a mixing angle of $\sin^2(2\theta) \sim 4 \times 10^{-10}$ and accounts for $\sim 25\%$ of the dark matter abundance.

As mentioned earlier, the Higgsino is chosen to be the LSP. We take its mass to be 800 GeV, so that it makes up about half of the dark matter. The scalar X with mass 7 PeV makes up the remaining fraction. Its abundance is controlled by the parameter α (for simplicity, we have taken a universal value $\alpha_i = \alpha$) and the reheat temperature T_{RH} (which we have set to 10^{10} GeV). Likewise, its decay rate is controlled by the parameter λ_2. We see that the correct relic density and decay rate can be obtained for fairly reasonable values of these couplings.

The spectrum of masses of various particles in this model are plotted in Figure 7.1, with particles that contribute to dark matter highlighted in blue. We have an interesting scenario where dark matter is a mix of three components at very different scales: a 7 keV sterile neutrino, a stable 800 GeV Higgsino, and a 7 PeV long-lived scalar. For the dark matter distribution we adopt the Navarro-Frenk-White (NFW) profile [144], which was also found to be compatible with models of warm [145] and mixed [93] dark matter, as well as the 3.5 keV line [17].

With these parameter choices, we now examine, in turn, the two signals of interest.

7.2.1 PeV Neutrinos at IceCube

In this section we study the spectrum of neutrinos at IceCube from the decay of X with the parameter choices above. For decaying dark matter, both galactic and extragalactic contributions are important. The galactic contribution to the neutrino flux $d\Phi_\alpha/dE_{\nu_\alpha}$, where α denotes the neutrino flavor, is given by [125] [2]

$$\left(\frac{d\Phi_\alpha}{dE_{\nu_\alpha}} \right)_{\text{gal}} = \kappa \left(\frac{1.5 \times 10^{-13}}{\text{cm}^2 \text{ sr s}} \right) \left(\frac{10^{28} \text{ s}}{\tau_X} \right) \left(\frac{\text{PeV}}{m_X} \right) \frac{1}{N} \frac{dN_\alpha}{dE_{\nu_\alpha}}, \tag{7.10}$$

[2]The coefficient in the first parenthesis differs from that in [125] since we use an NFW profile instead of an Einasto profile.
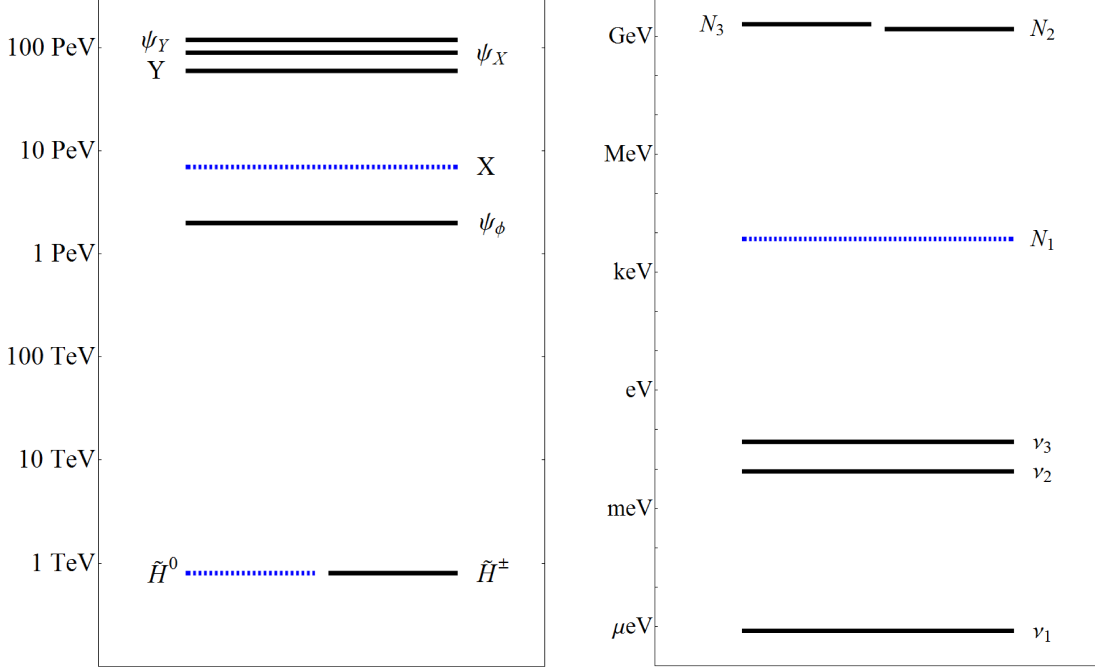
Figure 7.1: The mass spectrum of our model. The left box displays the heavy PeV scale states as well as the TeV scale Higgsinos. The right box shows the active and sterile neutrino mass eigenstates. Particles that form some fraction of dark matter are denoted by dashed blue lines.

where $\kappa = 0.25$ is the fraction of dark matter made up by X, $1/N(dN_\alpha/dE_{\nu_\alpha})$ is the normalized neutrino energy spectrum from X decay, and τ_X and m_X are, respectively, the lifetime and mass of X. Likewise, the extragalactic contribution is [125, 146]

$$\left(\frac{d\Phi_\alpha}{dE_{\nu_\alpha}}\right)_{\text{ex-gal}} = \kappa \left(\frac{2.5 \times 10^{-13}}{\text{cm}^2 \, \text{sr s}}\right) \left(\frac{10^{28} \, \text{s}}{\tau_X}\right) \left(\frac{\text{PeV}}{m_X}\right) \int_1^\infty dy \frac{dN_\alpha}{N \, d(E_{\nu_\alpha} y)} \frac{y^{-3/2}}{\sqrt{1 + (\Omega_\Lambda/\Omega_M) \, y^{-3}}} \, ,$$

(7.11)

where $\Omega_M = 0.315$, $\Omega_\Lambda = 0.685$, and $y = 1 + z$, where z is the redshift. The expected number of neutrino events at IceCube in the energy bin between E_1 and E_2 is given by

$$N(E_1, E_2) = 4\pi \, T \sum_\alpha \int_{E_1}^{E_2} dE_{\nu_\alpha} \, A_{\text{eff}}^\alpha(E_\nu) \left(\frac{d\Phi_\alpha}{dE_{\nu_\alpha}}\right)_{\text{gal} + \text{ex-gal}} \, ,$$

(7.12)

where $T = 988$ days is the total exposure time [18] and $A_{\text{eff}}^\alpha(E_\nu)$ is the IceCube effective area for neutrino flavor α, taken from [83].

We entered the model described in Section 7.1 into PYTHIA 8.2 [147] and generated the neutrino spectrum, $dN_\alpha/dE_{\nu_\alpha}$ from X decay following the decay chain specified in Section 7.1.3. The various decay channels and rates for the $\mathcal{O}(\text{keV-GeV})$ mass sterile neutrinos
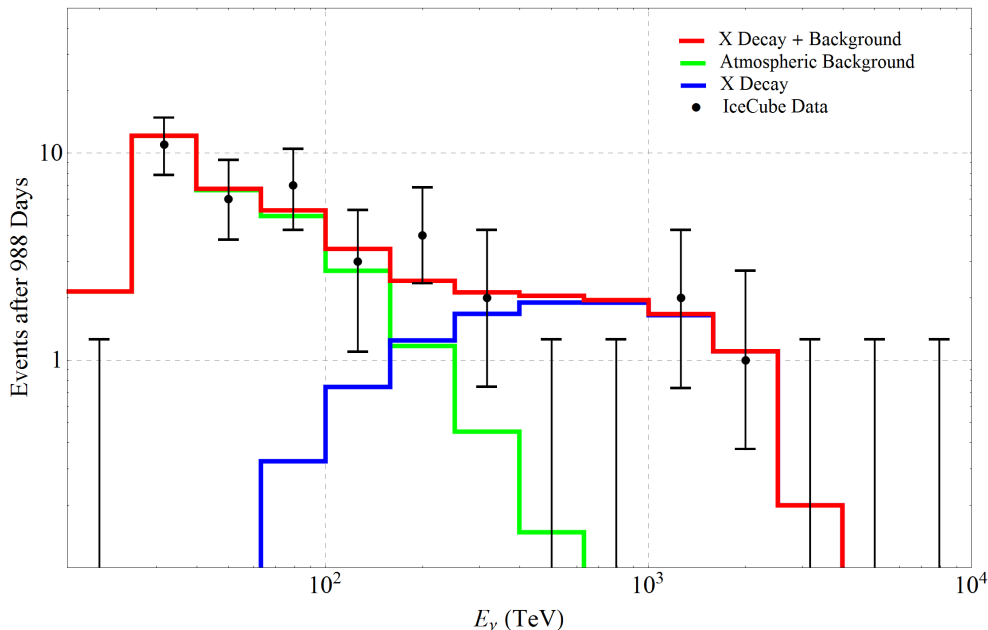
Figure 7.2: The expected number of neutrino events at IceCube from the decay of X (blue), together with IceCube data points and error bars (black) and atmospheric background (green) from [18], and the total number of signal + background events (red).

are listed in the appendix of [61]. The number of neutrino events in each IceCube bin thus predicted following the above procedure is shown in Figure 7.2 in blue. The IceCube data points (black dots), error bars, and background (green) are taken from [18]. The background events come from cosmic ray air showers, which produce π/K, and expected charmed mesons, which decay to muons and neutrinos; the background reported here is the sum of the average background from atmospheric muons and neutrinos, plus the 90% confidence level upper limit for neutrinos from charmed decays [18]. The total number of events expected (signal+background) for the reported exposure is shown in red.

From the plot, it is clear that the measurements in the lower energy bins are completely consistent with atmospheric background, whereas the higher energy bins (200 TeV and above) show a clear deviation from what is expected from background only, indicating an excess of neutrino events that requires some explanation. This excess has four salient features:

(i) an excess in two bins at $200 - 400$ TeV,

(ii) no events in the two bins covering 500 TeV - 1 PeV (see [148] for related discussions),

(iii) three PeV scale events, two at 1 PeV and one at 2 PeV, and

(iv) no events above 2 PeV.

An additional astrophysical power-law contribution could address (i), but clearly cannot

explain the three neutrinos with PeV energies (iii) [125].

Models of PeV dark matter in the literature claim to be able to explain these features by employing a two-body decay channel that includes a neutrino to give (iii) as well as a secondary decay channel that gives softer neutrinos to explain (i) [125, 126, 127, 128, 129, 130, 131, 132, 133, 134, 135]. In contrast, our model does not have a direct two-body decay channel into neutrinos, hence there is no sharp feature that peaks at PeV energies. Instead, since neutrinos are produced via two- or three- step decay chains, each involving multiple decay products, the neutrino spectrum is essentially flat, with a dropoff at approximately half the dark matter mass (blue curve in Figure 7.2). The flat spectrum allows us to generate a signal contribution that satisfactorily addresses both (i) and (iii), but at the cost of disagreeing with (ii). However, since less than 2 events are predicted in each of the two bins in (ii), the disagreement is not too fatal and can be attributed to a possible downward fluctuation of the signal. Hence the model predicts that events should appear in these bins when more data is collected. Finally, although the dark matter mass is chosen to have the spectrum drop off after the 2 PeV bin, hence explaining (iv), we note that somewhat heavier masses would still predict less than 1 event in each of the bins higher than 2 PeV and hence could remain compatible with the current data. Consequently, possible future measurements of events at energies higher than 2 PeV need not necessarily be incompatible with a dark matter explanation.

Additional Constraints

In addition to neutrinos, the dark matter decay products can also give visible signatures in other channels. The most important of these is gamma rays. The $e^{\pm}$ from dark matter decays produce energetic photons due to inverse Compton scattering and synchrotron radiation. Likewise, since the Universe is opaque to gamma rays with energies above a TeV, high energy gamma rays produce $e^{\pm}$ pairs through interactions with the interstellar radiation field. Such cascades from high energy products from dark matter decay therefore produce a population of gamma rays between $\mathcal{O}(1)$ GeV and $\mathcal{O}(100)$ GeV [149]. Following [130], we verify the compatibility of the dark matter decay process with gamma-ray bounds from the Fermi-LAT measurement of the isotropic diffuse gamma-ray background [150] by considering the integrated energy density ω_{γ} measured by the Fermi-LAT between $E_1 \sim \mathcal{O}(1)$ GeV and $E_2 \sim \mathcal{O}(100)$ GeV [130]

$$\omega_{\gamma} = \frac{4\pi}{c} \int_{E_1}^{E_2} E_{\gamma} \frac{d\Phi_{\gamma}}{dE_{\gamma}} dE_{\gamma} \approx 4.4 \times 10^{-7} \, \text{eV/cm}^3 \,. \tag{7.13}$$

The total energy density in photons and $e^{\pm}$ from the decay of X, using the output from PYTHIA, is calculated to be $\sim 4 \times 10^{-9}$ eV/cm^3. This can be interpreted as the maximum amount of energy that can be deposited in the diffuse gamma-ray background; since this is well below the energy density measured by Fermi quoted above, we conclude that the dark matter decay process is not in tension with gamma-ray measurements [3]. Likewise, we note that since the dark matter decays exclusively to leptons, it is unlikely to be in tension with the recent Ams-02 measurements of the $\bar{p}/p$ ratio [153] (from extrapolating Figure 5 of [154], which shows the bound on the lifetime of a dark matter particle decaying to $b\bar{b}$ from antiproton constraints, to $\mathcal{O}(10)$ PeV, it can be seen that even a hadronically decaying particle with a lifetime of $\sim 10^{27}$s would be well within the antiproton limits).

7.2.2 3.5 keV X-ray Signal

Several papers have interpreted this signal as the decay of a ~ 7 keV sterile neutrino dark matter component [55, 57, 59, 16, 17, 93, 155, 156, 157, 158, 159, 160, 161, 162, 163, 164, 165, 166, 167]. A keV scale sterile neutrino can be produced through the DW mechanism [35] with an approximate relic abundance

$$\Omega h^2 \sim 0.07 \left(\frac{\sin^2 2\theta}{10^{-9}} \right) \left(\frac{m_s}{7 \text{ keV}} \right)^2. \tag{7.14}$$

This is a consequence of non-resonant oscillation due to the mixing between the active and sterile sectors. However, sterile neutrinos produced through the DW mechanism accounting for all of dark matter has now been robustly ruled out for all masses based on constraints from X-ray bounds and Lyman-alpha data; see 5 for a summary.

This problem can be evaded in several ways. A lepton asymmetry in the early Universe can lead to resonant production of sterile neutrinos, resulting in a colder distribution that can evade Lyman-alpha bounds; this is known as the Shi-Fuller mechanism [45]. Another approach is to consider sterile neutrino production from the decays of a heavy scalar [51, 50, 54, 71], which can produce all of dark matter from the freeze-in mechanism [28] (for a discussion in the context of the 3.5 keV line, see [156]).

Likewise, the constraints are avoided if sterile neutrinos make up only a fraction of dark matter. While it is trivial to rescale the X-ray constraints to account for a smaller fraction of dark matter, a reinterpretation of the Lyman-alpha constraint is not straightforward and requires numerical simulations. An analysis in [68], for instance, showed that $m_s \geq 5$ keV warm component constituting $\leq 60\%$ of the total dark matter abundance, where the rest of

---

[3]See [151] for more stringent (but model-dependent) constraints from analyzing the spectrum rather than the integrated energy, and [152] for a discussion of prospects with extensive air shower (EAS) detectors.

the dark matter is made up of a cold component, is consistent with all constraints [91]; a follow-up study [92] found similar results. In a warm plus cold dark matter setup, [93] found that the 3.5 keV X-ray signal could be explained with a 7 keV sterile neutrino produced from DW that made up $10 - 60\%$ of dark matter. We construct our theory to map on to one of the benchmark points in [93], which were shown to satisfy the relevant constraints. In [93], the signal was found to be compatible with a non-resonantly produced 7 keV sterile neutrino with mixing angle $\sin^2(2\theta) \sim 4 \times 10^{-10}$, making up $\sim 25\%$ of dark matter; we reproduce these values with our choice of parameters in Table 7.2, thereby incorporating the 3.5 keV X-ray line in our framework.

A mixture of warm and cold components for dark matter offers several advantages. Ref. [93] found that this scenario was still compatible with an NFW profile and could resolve the missing satellite problem [168, 169]. In addition, we note that the larger free-streaming length of the non-resonantly produced sterile neutrino, which is a warm dark matter component, could result in it being underabundant in dwarf galaxies (which would be made up mostly of the cold component), possibly providing an explanation of the non-observation of the signal in the stacked analysis of dwarf spheroidals presented in [139]; establishing this would, however, require detailed numerical simulations that are beyond the scope of this work.

7.3 Summary

In this chapter we have incorporated two recent potential hints of new physics, the PeV neutrinos at IceCube and the 3.5 keV X-ray line, into a broader, independently motivated framework of a PeV scale supersymmetric neutrino sector.

- The right handed sterile neutrinos are expected to be charged under some new symmetry (e.g., $U(1)'$) beyond the SM gauge group, which enables light masses at phenomenologically interesting scales (keV-GeV). In order to successfully realize the desired active and sterile neutrino masses without unnaturally small parameters, this symmetry must be broken by a PeV scale vev, which corresponds to a desired scale in some approaches to supersymmetry breaking.

- The lightest sterile neutrino can have a mass of 7 keV and be produced non-resonantly through the DW mechanism to form a fraction of dark matter; its decay can explain the 3.5 keV X-ray line.

- The neutrino sector can be extended to include additional fields with similar operators to the ones that give rise to neutrino masses. This can give a PeV scale dark matter

component whose relic abundance is set by freeze-in processes, and an appropriate charge under the $U(1)'$ symmetry makes it long-lived and gives a decay spectrum into neutrinos consistent with the high energy events observed at IceCube.

The two signals considered here, at such different energy scales, fit rather naturally into a broader particle physics framework and could be the first indications of a rich, hitherto unexplored neutrino sector.

Appendix A

Boltzmann Equations and Collision Terms

A.1 Scenario I: ϕ in equilibrium, no supersymmetry

Assuming that N_i has a negligible initial abundance, the relevant phase space density weights in the Boltzmann equations simplify to

$$\Omega(\phi \to N_1 \, N_1) \approx f_\phi, \quad \Omega(\phi \, \phi \to N_1 \, N_1) \approx f_\phi f_\phi, \tag{A.1}$$

resulting in the following Boltzmann equation for f_{N_1}:

$$Hr \frac{\partial f_{N_1}}{\partial r} = C_{\phi \to N_1 \, N_1}[f_{N_1}] + C_{\phi \, \phi \to N_1 \, N_1}[f_{N_1}]. \tag{A.2}$$

Each collision term takes the form given in Eq. 6.11. Since both processes take place for temperatures much greater than the mass m_{N_1}, we will approximate N_1 as massless throughout the calculation. Furthermore, since the annihilation of ϕ is a UV process taking place only a high temperatures just after reheating, we will set $m_\phi \to 0$ for the computation of the annihilation collision term.

The collision term for the annihilation process is

$$C_{\phi \, \phi \to N_1 \, N_1}[f_{N_1}] = \frac{2}{2E_{N_1}} \int \mathrm{d}\Pi_\phi \, \mathrm{d}\Pi_{\phi'} \, \mathrm{d}\Pi_{N_1'} |\mathcal{M}|^2 (2\pi)^4 \delta^4 \left(\Sigma p\right) f_\phi(p_\phi) f_\phi(p_{\phi'}) \tag{A.3}$$

$$= \frac{x_1^2}{(2\pi)^3 M_*^2} \, T^3 \exp(-p_{N_1}/T) \, \Theta(T - T_d). \tag{A.4}$$

where T_d is the decoupling temperature of ϕ (Eq. 6.28).

The collision term corresponding to ϕ decay is

$$C_{\phi \to N_1 N_1}[f_{N_1}] = \frac{2}{2E_{N_1}} \int d\Pi_\phi \, d\Pi_{N_1'} |\mathcal{M}|^2 (2\pi)^4 \delta^4 \left(\Sigma p\right) f_\phi(p_\phi) \tag{A.5}$$

$$= \frac{x_{1\,\text{eff}}^2 m_\phi^2}{16\pi p_{N_1}^2} \int_{p_{\phi,\text{min}}}^\infty dp_\phi \frac{p_\phi}{E_\phi} f_\phi(p_\phi) \,, \tag{A.6}$$

where $x_{1\,\text{eff}} = \frac{2x_1 \langle \phi \rangle}{M_*}$ and kinematic considerations restrict the momentum integration over p_ϕ to be greater than

$$p_{\phi,\text{min}} \equiv \left| p_{N_1} - \frac{m_\phi}{4p_{N_1}} \right| \,. \tag{A.7}$$

A.2 Scenario II: ϕ freezes in, no supersymmetry

Since ϕ freezes in, $f_\phi \ll 1$, and for its UV production process $L_i H \to N_{2,3} \phi$ we can approximate

$$\Omega(L_i H \to N_{2,3} \phi) \approx f_H f_{L_i} \approx e^{(E_{L_i} + E_H)/T} \,. \tag{A.8}$$

This frozen-in population of ϕ decays entirely into sterile neutrinos once ϕ obtains a vev. Such decays lead to DM production via $\phi \to N_1 N_1$, with

$$\Omega(\phi \to N_1 N_1) \simeq f_\phi \,. \tag{A.9}$$

The corresponding Boltzmann equations for the freeze-in of ϕ and subsequent production of dark matter N_1 are

$$Hr \frac{\partial f_\phi}{\partial r} = \sum_{\substack{i=e,\mu,\tau \\ j=2,3}} C_{L_i H \to N_j \phi}[f_\phi] + \sum_{k=1,2,3} C_{\phi \to N_k N_k}[f_\phi] \tag{A.10}$$

$$Hr \frac{\partial f_{N_1}}{\partial r} = C_{\phi \to N_1 N_1}[f_{N_1}] \,. \tag{A.11}$$

A.2.1 Collision Terms for ϕ

Here me must track the production of ϕ through $L_i H \to N_{2,3} \phi$ and its eventual decay $\phi \to N_i N_i$. The freeze-in of ϕ takes place at temperatures much higher than the mass of

any particle involved, hence we treat all particles as massless, obtaining

$$C_{L_i H \to N_j \phi}[f_\phi] = \frac{1}{2E_\phi} \int d\Pi_L \, d\Pi_H \, d\Pi_N |\mathcal{M}|^2 (2\pi)^4 \delta^4 (\Sigma p) \, f_L(p_L) f_H(p_H)$$

$$= \frac{y_{ij}^2}{4\pi^3 M_*^2} \, T^3 \exp(-p_\phi/T) \,. \tag{A.12}$$

The decay process, $\phi \to N_i N_i$ for $i = 1, 2, 3$, gives the corresponding collision term for f_ϕ:

$$C_{\phi \to N_i N_i}[f_\phi] = \frac{-1}{2E_\phi} \int d\Pi_N \, d\Pi'_N |\mathcal{M}|^2 (2\pi)^4 \delta^4 (\Sigma p) \, f_\phi(p_\phi)$$

$$= -\frac{x_{i \text{ eff}}^2 m_\phi^2}{16\pi E_\phi} f_\phi(p_\phi) \,. \tag{A.13}$$

A.2.2 Collision Terms for N_1

Since dark matter production through ϕ decay mainly takes place at temperatures below m_ϕ, for calculating f_{N_1} we make the approximation that the decaying ϕ is at rest:

$$f_\phi(p_\phi, T) \simeq 2\pi^2 n_\phi(T) \frac{\delta(p_\phi)}{p_\phi^2} \,, \quad \text{for } T \ll m_\phi \,, \tag{A.14}$$

where $n_\phi(T)$ is determined by solving Eq. A.10 for $f_\phi(p_\phi, T)$ and integrating over the phase space of p_ϕ. Inserting this approximation in Eq. A.6, we find

$$C_{\phi \to N_1 N_1}[f_{N_1}] \simeq \frac{\pi x_{1 \text{ eff}}^2}{2m_\phi} n_\phi(T) \delta \left(p_N - \frac{m_\phi}{2} \right) \,. \tag{A.15}$$

A.2.3 Analytical Results for Ω_{N_1}

Here we examine the freeze-in abundance of N_1 and derive some analytical results. The population of N_1 in this scenario comes entirely from ϕ decays. Therefore, we will track the UV freeze-in of ϕ and its subsequent decay to dark matter.

The yield of ϕ during the UV freeze-in era can be found by considering the Boltzmann equation for f_ϕ, only taking into account the annihilation $L_i + H \to N_j + \phi$ and ignoring the

decay of ϕ:

$$L[f_\phi] = \sum_{i,j=1,2,3} C_{L_i H \to N_j \phi}[f_\phi]$$

$$= \frac{y^2}{4\pi^3} \frac{T^3}{M_*^2} e^{-\sqrt{p^2 + m_\phi^2}/T} , \tag{A.16}$$

where $y^2 \equiv \sum_{i,j} y_{ij}^2$ and we have restored the factor of m_ϕ in the expression for energy. Integrating both sides over ϕ momentum space, we obtain an expression in terms of the number density n_ϕ:

$$\dot{n}_\phi + 3H n_\phi = \frac{y^2}{8\pi^5} \frac{T^4 m_\phi^2}{M_*^2} K_2 \left(\frac{m_\phi}{T} \right) . \tag{A.17}$$

Recasting this expression in terms the yield $Y_\phi = \frac{n_\phi}{s}$, where $s = \frac{2\pi^2 g_*^S T^3}{45}$ is the entropy density, and using the relationship between time and temperature during the radiation dominated era

$$t = \frac{0.301}{\sqrt{g_*^\rho}} \frac{M_P}{T^2} , \tag{A.18}$$

we find that

$$\frac{dY_\phi}{dT} = -\frac{45 y^2}{1.66 \times 16\pi^7 g_*^S \sqrt{g_*^\rho}} \frac{M_P}{M_*^2} \frac{m_\phi^2}{T^2} K_2 \left(\frac{m_\phi}{T} \right) . \tag{A.19}$$

Integrating from $T = T_{RH}$ to $T = 0$, we find the yield of ϕ after it has frozen-in:

$$Y_{\phi,FI} \simeq \frac{45 y^2}{1.66 \times 8\pi^7 g_*^S \sqrt{g_*^\rho}} \frac{M_P T_{RH}}{M_*^2} , \tag{A.20}$$

where we have used the approximation

$$\frac{m_\phi^2}{T^2} K_2 \left(\frac{m_\phi}{T} \right) \simeq \begin{cases} 2 & T_{RH} \gg m_\phi \\ 0 & T_{RH} \ll m_\phi \end{cases} . \tag{A.21}$$

Let us now estimate the temperature T_{FI} at which ϕ has "frozen-in". Since the yield of ϕ will asymptotically approach $Y_{\phi,FI}$ as $T \to 0$, we will define T_{FI} as the temperature at which the yield is half the final freeze-in yield, i.e. $Y_\phi(T_{FI}) = \frac{1}{2} Y_{\phi,FI}$. Since $\frac{dY_\phi}{dT}$ is approximately constant for high temperatures, $T \gg m_\phi$, the freeze in temperature is $T_{FI} \simeq \frac{1}{2} T_{RH}$.

We can compare T_{FI} with the temperature at which the ϕ population starts to decay, at

time $\tau_\phi = \Gamma_\phi^{-1}$. Using the time-temperature relation in eq. A.18, this temperature is

$$T_{\phi \to NN} = \frac{x \langle \phi \rangle}{M_*} \sqrt{\frac{0.301 M_P m_\phi}{4\pi \sqrt{g_*^\rho}}}$$

$$\simeq 1.7 \text{ TeV} \times x \ \left(\frac{\langle \phi \rangle}{100 \text{ PeV}} \right) \left(\frac{10^{16} \text{ GeV}}{M_*} \right) \left(\frac{m_\phi}{1 \text{ PeV}} \right)^{1/2} , \quad (A.22)$$

where $x^2 \equiv \sum_i x_i^2$. So for reheat temperatures much higher than the TeV scale, the freeze-in and decay of ϕ are well separated processes, for typical parameter choices in this model.

ϕ will decay to N_i with branching ratio x_i^2/x^2. In the extreme case where $x_1 \gg x_{2,3}$, we expect every ϕ particle to decay into two N_1's, so that the final N_1 yield is twice that of the frozen-in ϕ yield. In general, the N_1 yield will be

$$Y_{N_1, FI} = 2 \frac{x_1^2}{x^2} Y_{\phi, FI} . \quad (A.23)$$

Taking into account the entropy dilution from $N_{2,3}$ decays, the abundance of N_1 today will be

$$\Omega_{N_1} = \frac{m_{N_1} s_0 Y_{N_1, FI}}{S_{N23} \rho_c} . \quad (A.24)$$

A.3 Scenario III: ϕ in equilibrium, supersymmetry

Since ϕ and ψ are in equilibrium whereas $\tilde{N}_i$ and N_i have negligible abundance at high temperatures, we approximate

$$\Omega(\phi\phi \to N_1 N_1) \simeq f_\phi f_\phi , \quad \Omega(\phi\psi \to N_1 \tilde{N}_1) \simeq f_\phi f_\psi , \quad \Omega(\psi\psi \to \tilde{N}_1 \tilde{N}_1) \simeq f_\psi f_\psi .$$

$$\Omega(\phi \to N_1 N_1) \simeq \Omega(\phi \to \tilde{N}_1 \tilde{N}_1) \simeq f_\phi , \quad \Omega(\tilde{N}_1 \to \psi N_1) \simeq f_{\tilde{N}_1} . \quad (A.25)$$

Note that the phase space densities of N_1 and $\tilde{N}_1$ from UV freeze-in should be identical, hence they do not need to be tracked separately, whereas the IR components will differ due to $\phi \to \tilde{N}_1 \tilde{N}_1$ proceeding via the soft term.

The Boltzmann equations describing the evolution of N_1 and $\tilde{N}_1$ distributions are

$$Hr \frac{\partial f_{N_1}}{\partial r} = C_{\phi\phi \to N_1 N_1}[f_{N_1}] + C_{\phi\psi \to N_1 \tilde{N}_1}[f_{N_1}] + C_{\tilde{N}_1 \to N_1 \psi}[f_{N_1}] + C_{\phi \to N_1 N_1}[f_{N_1}] , \quad (A.26)$$

$$Hr \frac{\partial f_{\tilde{N}_1}}{\partial r} = C_{\psi\psi \to \tilde{N}_1 \tilde{N}_1}[f_{\tilde{N}_1}] + C_{\phi\psi \to N_1 \tilde{N}_1}[f_{\tilde{N}_1}] + C_{\tilde{N}_1 \to N_1 \psi}[f_{\tilde{N}_1}] + C_{\phi \to \tilde{N}_1 \tilde{N}_1}[f_{\tilde{N}_1}] . \quad (A.27)$$

A.3.1 UV Freeze-In

Collision terms describing the UV freeze-in of N_1 and $\tilde{N}_1$ are similar to the $\phi\,\phi \to N_1\,N_1$ collision term in Scenario I (Eq. A.4), similarly resulting in

$$C_{\phi\phi \to N_1 N_1}[f_{N_1}] = 4 \times C_{\phi\psi \to N_1 \tilde{N}_1}[f_{N_1}] = \frac{4\eta^2}{(2\pi)^3 M_*^2}\, T^3 \exp(-p_{N_1}/T)\,\Theta(T - T_d), \qquad (A.28)$$

$$C_{\psi\psi \to \tilde{N}_1 \tilde{N}_1}[f_{\tilde{N}_1}] = 4 \times C_{\phi\psi \to N_1 \tilde{N}_1}[f_{\tilde{N}_1}] = \frac{4\eta^2}{(2\pi)^3 M_*^2}\, T^3 \exp(-p_{\tilde{N}_1}/T)\,\Theta(T - T_d), \qquad (A.29)$$

where the factor of 4 accounts for permutations of incoming and outgoing particles.

A.3.2 IR Freeze-In

The two collision terms corresponding to the IR freeze-in of N_1 are also similar to previously calculated collision terms; we have

$$C_{\phi \to N_1 N_1}[f_{N_1}] = \frac{\eta_{1\,\text{eff}}^2 m_\phi^2}{8\pi p_{N_1}^2} \int_{p_{\phi,\text{min}}}^{\infty} \mathrm{d}p_\phi \frac{p_\phi}{E_\phi} f_\phi(p_\phi). \qquad (A.30)$$

Likewise, since $\tilde{N}_1$ decays late, we make the approximation that it is at rest at the time of decay

$$f_{\tilde{N}_1}\left(p_{\tilde{N}_1}, T\right) \simeq \pi^2 n_{\tilde{N}_1}(T) \frac{\delta(p_{\tilde{N}_1})}{p_{\tilde{N}_1}^2}, \quad \text{for } T \ll m_{\tilde{N}_1}, \qquad (A.31)$$

where the number density $n_{\tilde{N}_1}$ is found by solving the Boltzmann equations for $\tilde{N}_1$. The corresponding collision term is

$$C_{\tilde{N}_1 \to N_1 \psi}[f_{N_1}] \simeq \frac{\pi \eta_{1\,\text{eff}}^2}{8 m_{\tilde{N}_1}}\, n_{\tilde{N}_1}(T)\, \delta\left(p_{N_1} - \frac{m_{\tilde{N}_1}^2 - m_\psi^2}{2 m_{\tilde{N}_1}}\right). \qquad (A.32)$$

The corresponding collision term for $f_{\tilde{N}_1}$ can be found in a similar manner to $C_{\phi \to N_i N_i}[f_\phi]$ in scenario II:

$$C_{\tilde{N}_1 \to N_1 \psi}[f_{\tilde{N}_1}] = -\frac{\eta_{1\,\text{eff}}^2 (m_{\tilde{N}_1}^2 - m_\psi^2)^2}{16\pi E_{\tilde{N}_1} m_{\tilde{N}_1}^2} f_{\tilde{N}_1}(p_{\tilde{N}_1}). \qquad (A.33)$$

The collision term for $f_{\tilde{N}_1}$ for $\phi \to \tilde{N}_i \tilde{N}_i$ arising from the soft SUSY breaking term $\eta_i \frac{A_{\eta_i}}{M_*} \phi\phi \tilde{N}_i \tilde{N}_i$ is:

$$C_{\phi \to \tilde{N}_1 \tilde{N}_1}[f_{\tilde{N}_1}] = \frac{\eta_{1\,\text{eff}}^2 A_{\eta_i}^2}{4\pi E_{\tilde{N}_1} p_{\tilde{N}_1}} \int_{p_{\phi,\text{min}}}^{p_{\phi,\text{max}}} \mathrm{d}p_\phi \frac{p_\phi}{E_\phi} f_\phi(p_\phi), \qquad (A.34)$$

where

$$p_{\phi,\ \substack{\max \\ \min}} = \frac{\pm p_{\tilde{N}_1} m_\phi^2 + E_{\tilde{N}_1} m_\phi \sqrt{m_\phi^2 - 4m_{\tilde{N}_1}^2}}{2m_{\tilde{N}_1}^2} \,. \tag{A.35}$$

A.4 Scenario IV: ϕ freezes in, supersymmetry

The full set of Boltzmann equations describing the evolution of ϕ, N_1, and $\tilde{N}_1$ are

$$Hr\frac{\partial f_\phi}{\partial r} = \sum_{\substack{i=e,\mu,\tau \\ j=2,3}} \left(C_{L_i\, H \to N_j\, \phi}[f_\phi] + C_{L_i\, \tilde{H} \to \tilde{N}_j\, \phi}[f_\phi] + C_{\tilde{L}_i\, \tilde{H} \to N_j\, \phi}[f_\phi] \right)$$

$$+ \sum_{k=1,2,3} \left(C_{\phi \to N_k\, N_k}[f_\phi] + C_{\phi \to \tilde{N}_k\, \tilde{N}_k}[f_\phi] \right) \tag{A.36}$$

$$Hr\frac{\partial f_{N_1}}{\partial r} = C_{\phi \to N_1\, N_1}[f_{N_1}] + C_{\tilde{N}_1 \to N_1\, \psi}[f_{N_1}] \tag{A.37}$$

$$Hr\frac{\partial f_{\tilde{N}_1}}{\partial r} = C_{\tilde{N}_1 \to N_1\, \psi}[f_{\tilde{N}_1}] + C_{\phi \to \tilde{N}_1\, \tilde{N}_1}[f_{\tilde{N}_1}] \,. \tag{A.38}$$

A.4.1 Collision Terms for ϕ

Collision terms for ϕ are almost identical to those in Scenario II, with additional channels:

$$\sum_{\substack{i=e,\mu,\tau \\ j=2,3}} \left(C_{L_i\, H \to N_j\, \phi}[f_\phi] + C_{L_i\, \tilde{H} \to \tilde{N}_j\, \phi}[f_\phi] + C_{\tilde{L}_i\, \tilde{H} \to N_j\, \phi}[f_\phi] \right) = \sum_{\substack{i=e,\mu,\tau \\ j=2,3}} \frac{4\xi_{ij}^2}{\pi^3 M_*^2}\, T^3 \exp(-p_\phi/T)\,. \tag{A.39}$$

Similarly, for the decay processes,

$$C_{\phi \to N_i\, N_i}[f_\phi] = -\frac{\eta_{i\ \text{eff}}^2\, m_\phi^2}{16\pi E_\phi} f_\phi(p_\phi) \tag{A.40}$$

$$C_{\phi \to \tilde{N}_i\, \tilde{N}_i}[f_\phi] = -\frac{\eta_{i\ \text{eff}}^2 A_{\eta_i}^2}{8\pi m_\phi} \sqrt{1 - \frac{4m_{\tilde{N}_1}^2}{m_\phi^2}}\, \frac{m_\phi}{E_\phi} f_\phi(p_\phi)\,. \tag{A.41}$$

A.4.2 Collision Terms for $\tilde{N}_1$ and N_1

$\tilde{N}_1$ production via $\phi \to \tilde{N}_1\, \tilde{N}_1$ occurs when ϕ is approximately at rest (see Eq. A.14), giving

$$C_{\phi \to \tilde{N}_1\, \tilde{N}_1}[f_{\tilde{N}_1}] \simeq \frac{\pi \eta_{1\ \text{eff}}^2 A_{\eta_1}^2}{4m_\phi^3 \sqrt{1 - 4m_{\tilde{N}_1}^2/m_\phi^2}} n_\phi(T) \delta\left(p_N - \sqrt{m_\phi^2/4 - m_{\tilde{N}_1}^2} \right)\,. \tag{A.42}$$

Its decay proceeds just as in Scenario III (Eq. A.33).

For decays into N_1, as in Scenario II, the decaying ϕ and $\tilde{N}_1$ are taken to be at rest, thus the collision terms for f_{N_1} are identical to Eq. A.15 (for ϕ decay) and Eq. A.32 (for $\tilde{N}_1$ decay).

Appendix B

Possibilities for X Decay

In this appendix, we examine the lifetime of the scalar X, which may decay into ϕ and/or ψ. We consider a list of different operators that may couple these fields. In each case, we assume that X has only one dominant decay channel, set by the operator under consideration, which fixes the lifetime of X. Our goal will be to determine the operator of smallest mass dimension that keeps X stable on time scales of order the age of the Universe ($\sim 10^{17}$ s).

To begin, consider the decay of X into n particles. In general, the rate for an n-body decay is given by:

$$d\Gamma_X = \frac{(2\pi)^4}{2M_X}|\mathcal{M}|^2 d\Phi_n(P_X; p_1, \ldots, p_n) \tag{B.1}$$

where

$$d\Phi_n(P_X; p_1, \ldots, p_n) = \delta^4\left(P_X - \sum_{i=1}^{n} p_i\right) \prod_{i=1}^{n} \frac{d^3 p_i}{(2\pi)^3 2E_i} \tag{B.2}$$

is the n-body phase space.

Here, we will estimate the phase space factors by assuming that the final particles are massless scalars, so that $\mathcal{M}$ is a constant. For an operator of dimension d the corresponding matrix element is approximately:

$$|\mathcal{M}|^2 \sim \lambda^2 \frac{M_X^{2(d-n-1)}}{M_*^{2(d-4)}}, \tag{B.3}$$

where M_* is the cutoff scale, and λ is a dimensionless coupling.

With constant $\mathcal{M}$, we express the decay rate as:

$$\Gamma_X = \frac{(2\pi)^4}{2M_X}|\mathcal{M}|^2 f_n, \tag{B.4}$$

where f_n is the n-body phase space factor, obtained by integrating over the n-body phase

space $d\Phi_n$.

The 4-body phase space $d\Phi_4$ may be calculated using the well known 2- and 3-body phase spaces. In general, n-body phase space may be calculated recursively:

$$
\begin{aligned}
d\Phi_n(P; p_1, \ldots, p_n) &= d\Phi_j(q; p_1, \ldots, p_j) \\
&\times d\Phi_{n-j+1}(P; q, p_j + 1, \ldots, p_n)(2\pi)^3 dq^2,
\end{aligned}
\tag{B.5}
$$

for some $1 < j < n$. The expressions for 2- and 3-body phase spaces with massless particles are:

$$
\begin{aligned}
d\Phi_2(q; p_1, p_2) &= \frac{1}{8(2\pi)^6} \, d\Omega_1^* &&\text{(1+2 rest frame)} \\
d\Phi_3(P_X; q, p_3, p_4) &= \frac{1}{8(2\pi)^9} \, dE_3 \, dE_4 \, d\alpha \, d(\cos\beta) \, d\gamma &&\text{(X rest frame)}
\end{aligned}
\tag{B.6}
$$

where the * indicates the quantity is evaluated in the $q = p_1 + p_2$ rest frame, $m_{12}^2 = q^2$, and α, β, γ are the Euler angles needed to specify the plane of the 3-body decay. Using equation B.5 we find:

$$
d\Phi_4(P_X; p_1, \ldots, p_4) = \frac{1}{64(2\pi)^{10}} \, d\Omega_1^* \, dE_3 \, dE_4 \, dm_{12}^2,
\tag{B.7}
$$

after integrating over the angles α, β, γ (since $|\mathcal{M}|^2$ is constant).

A convenient change of coordinates can be made using the relation:

$$
m_{12}^2 = M_X^2 - 2M_X(E_3 + E_4) + 2E_3 E_4(1 - \cos\theta_{34}),
\tag{B.8}
$$

where θ_{34} is the angle between $\mathbf{p_3}$ and $\mathbf{p_4}$ in the X rest frame. Now we may exchange the differential $dm_{12}^2 \to 2E_3 E_4 \, d(\cos\theta_{34})$, where the sign is compensated by choosing to integrate $\cos\theta_{34}$ from -1 to +1:

$$
d\Phi_4(P_X; p_1, \ldots, p_4) = \frac{E_3 E_4}{32(2\pi)^{10}} \, d\Omega_1^* \, dE_3 \, dE_4 \, d(\cos\theta_{34}).
\tag{B.9}
$$

Integrating over Ω_1^* and $\cos\theta_{34}$, and $E_{3,4}$ over the range $0 < E_{3,4} < M_X/2$ and $E_3 + E_4 > M_X/2$, gives the phase space factor:

$$
f_4 = \frac{5M_X^4}{3072(2\pi)^9}.
\tag{B.10}
$$

For completeness, we give the 2- and 3- body phase space factors as well:

$$f_2 = \frac{1}{4(2\pi)^5}$$

$$f_3 = \frac{M_X^2}{32(2\pi)^7} \,.$$

(B.11)

Using our estimation for $\mathcal{M}$ and f_n, we can use equation B.4 to approximate the lifetime of X coming from various operators $\mathcal{O}$.

$\mathcal{O}$	τ_X
$X\phi^2$	3.31×10^{-49} s $\times \lambda^{-2} \left(\frac{M_X}{\text{PeV}}\right) \left(\frac{M_*}{10^{16}\text{ GeV}}\right)^{-2}$
$X\phi^3$	1.04×10^{-26} s $\times \lambda^{-2} \left(\frac{M_X}{\text{PeV}}\right)^{-1}$
$X\phi^4$	7.92×10^{-4} s $\times \lambda^{-2} \left(\frac{M_X}{\text{PeV}}\right)^{-3} \left(\frac{M_*}{10^{16}\text{ GeV}}\right)^{2}$
$X\psi\psi$	3.31×10^{-29} s $\times \lambda^{-2} \left(\frac{M_X}{\text{PeV}}\right)^{-1}$
$X\langle\phi\rangle\psi\psi$	3.31×10^{-13} s $\times \lambda^{-2} \left(\frac{M_X}{\text{PeV}}\right)^{-1} \left(\frac{\langle\phi\rangle}{100\text{ PeV}}\right)^{-2} \left(\frac{M_*}{10^{16}\text{ GeV}}\right)^{2}$
$X\langle\phi\rangle^2\psi\psi$	3.31×10^{3} s $\times \lambda^{-2} \left(\frac{M_X}{\text{PeV}}\right)^{-1} \left(\frac{\langle\phi\rangle}{100\text{ PeV}}\right)^{-4} \left(\frac{M_*}{10^{16}\text{ GeV}}\right)^{4}$
$X\langle\phi\rangle^3\psi\psi$	3.31×10^{19} s $\times \lambda^{-2} \left(\frac{M_X}{\text{PeV}}\right)^{-1} \left(\frac{\langle\phi\rangle}{100\text{ PeV}}\right)^{-6} \left(\frac{M_*}{10^{16}\text{ GeV}}\right)^{6}$

The simplest operator that can yield a long enough lifetime for X is:

$$X\langle\phi\rangle^3\psi\psi \,.$$

(B.12)

Such an operator may originate from the superpotential term

$$\mathcal{W} \supset \frac{\lambda_2}{M_*^3}\mathcal{X}\Phi^5 \,,$$

(B.13)

with three vev insertions in the corresponding lagrangian term. This analysis leads us to choose a $U(1)'$ charge of $+5$ for the scalar X (where ϕ has charge -1) to ensure its stability.

Bibliography

[1] F. Reines and C. L. Cowan, "The neutrino," *Nature* **178** (1956) 446–449.

[2] G. Danby, J. M. Gaillard, K. A. Goulianos, L. M. Lederman, N. B. Mistry, M. Schwartz, and J. Steinberger, "Observation of High-Energy Neutrino Reactions and the Existence of Two Kinds of Neutrinos," *Phys. Rev. Lett.* **9** (1962) 36–44.

[3] **DONUT** Collaboration, K. Kodama *et al.*, "Observation of tau neutrino interactions," *Phys. Lett.* **B504** (2001) 218–224, `arXiv:hep-ex/0012035 [hep-ex]`.

[4] S. Weinberg, "Baryon and Lepton Nonconserving Processes," *Phys. Rev. Lett.* **43** (1979) 1566–1570.

[5] B. Pontecorvo, "Neutrino Experiments and the Problem of Conservation of Leptonic Charge," *Sov. Phys. JETP* **26** (1968) 984–988. [Zh. Eksp. Teor. Fiz.53,1717(1967)].

[6] G. F. Giudice and A. Strumia, "Probing High-Scale and Split Supersymmetry with Higgs Mass Measurements," *Nucl.Phys.* **B858** (2012) 63–83, `arXiv:1108.6077 [hep-ph]`.

[7] N. Arkani-Hamed, A. Gupta, D. E. Kaplan, N. Weiner, and T. Zorawski, "Simply Unnatural Supersymmetry," `arXiv:1212.6971 [hep-ph]`.

[8] A. Arvanitaki, N. Craig, S. Dimopoulos, and G. Villadoro, "Mini-Split," *JHEP* **1302** (2013) 126, `arXiv:1210.0555 [hep-ph]`.

[9] J. D. Wells, "Implications of supersymmetry breaking with a little hierarchy between gauginos and scalars," `arXiv:hep-ph/0306127 [hep-ph]`.

[10] N. Arkani-Hamed and S. Dimopoulos, "Supersymmetric unification without low energy supersymmetry and signatures for fine-tuning at the LHC," *JHEP* **0506** (2005) 073, `arXiv:hep-th/0405159 [hep-th]`.

[11] G. Giudice and A. Romanino, "Split supersymmetry," *Nucl.Phys.* **B699** (2004) 65–89, arXiv:hep-ph/0406088 [hep-ph].

[12] J. D. Wells, "PeV-scale supersymmetry," *Phys.Rev.* **D71** (2005) 015013, arXiv:hep-ph/0411041 [hep-ph].

[13] S. B. Roland, B. Shakya, and J. D. Wells, "Neutrino Masses and Sterile Neutrino Dark Matter from the PeV Scale," *Phys. Rev.* **D92** no. 11, (2015) 113009, arXiv:1412.4791 [hep-ph].

[14] S. B. Roland and B. Shakya, "Cosmological Imprints of Frozen-In Light Sterile Neutrinos," arXiv:1609.06739 [hep-ph].

[15] S. B. Roland, B. Shakya, and J. D. Wells, "PeV neutrinos and a 3.5keV x-ray line from a PeV-scale supersymmetric neutrino sector," *Phys. Rev.* **D92** no. 9, (2015) 095018, arXiv:1506.08195 [hep-ph].

[16] E. Bulbul, M. Markevitch, A. Foster, R. K. Smith, M. Loewenstein, *et al.*, "Detection of An Unidentified Emission Line in the Stacked X-ray spectrum of Galaxy Clusters," *Astrophys.J.* **789** (2014) 13, arXiv:1402.2301 [astro-ph.CO].

[17] A. Boyarsky, O. Ruchayskiy, D. Iakubovskyi, and J. Franse, "Unidentified Line in X-Ray Spectra of the Andromeda Galaxy and Perseus Galaxy Cluster," *Phys.Rev.Lett.* **113** (2014) 251301, arXiv:1402.4119 [astro-ph.CO].

[18] **IceCube** Collaboration, M. Aartsen *et al.*, "Observation of High-Energy Astrophysical Neutrinos in Three Years of IceCube Data," *Phys.Rev.Lett.* **113** (2014) 101101, arXiv:1405.5303 [astro-ph.HE].

[19] E. W. Kolb and M. S. Turner, "The Early Universe," *Front. Phys.* **69** (1990) 1–547.

[20] V. Mukhanov, *Physical Foundations of Cosmology.* Cambridge University Press, Oxford, 2005.

[21] J. B. Hartle, *An introduction to Einstein's general relativity.* Addison-Wesley, 2003.

[22] J. Lesgourgues, G. Mangano, G. Miele, and S. Pastor, "Neutrino cosmology," *Contemporary Physics* **54** no. 3, (2013) 178–179.

[23] **Planck** Collaboration, P. A. R. Ade *et al.*, "Planck 2015 results. XIII. Cosmological parameters," arXiv:1502.01589 [astro-ph.CO].

[24] J. Bernstein, *Kinetic Theory in the Expanding Universe.* Cambridge University Press, 1988.

[25] S. Groot, W. Leeuwen, and C. van Weert, *Relativistic Kinetic Theory: Principles and Applications.* North-Holland Pub. Co., 1980.

[26] G. Jungman, M. Kamionkowski, and K. Griest, "Supersymmetric dark matter," *Phys. Rept.* **267** (1996) 195–373, arXiv:hep-ph/9506380 [hep-ph].

[27] J. Ellis and K. A. Olive, "Supersymmetric Dark Matter Candidates," arXiv:1001.3651 [astro-ph.CO].

[28] L. J. Hall, K. Jedamzik, J. March-Russell, and S. M. West, "Freeze-In Production of FIMP Dark Matter," *JHEP* **03** (2010) 080, arXiv:0911.1120 [hep-ph].

[29] C. Cheung, G. Elor, L. J. Hall, and P. Kumar, "Origins of Hidden Sector Dark Matter I: Cosmology," *JHEP* **03** (2011) 042, arXiv:1010.0022 [hep-ph].

[30] F. Elahi, C. Kolda, and J. Unwin, "UltraViolet Freeze-in," arXiv:1410.6157 [hep-ph].

[31] Ya. B. Zeldovich, "Gravitational instability: An Approximate theory for large density perturbations," *Astron. Astrophys.* **5** (1970) 84–89.

[32] M. Boylan-Kolchin, J. S. Bullock, and M. Kaplinghat, "Too big to fail? The puzzling darkness of massive Milky Way subhaloes," *Mon.Not.Roy.Astron.Soc.* **415** (2011) L40, arXiv:1103.0007 [astro-ph.CO].

[33] M. Boylan-Kolchin, J. S. Bullock, and M. Kaplinghat, "The Milky Way's bright satellites as an apparent failure of LCDM," *Mon.Not.Roy.Astron.Soc.* **422** (2012) 1203–1218, arXiv:1111.2048 [astro-ph.CO].

[34] M. R. Lovell, V. Eke, C. S. Frenk, L. Gao, A. Jenkins, *et al.*, "The Haloes of Bright Satellite Galaxies in a Warm Dark Matter Universe," *Mon.Not.Roy.Astron.Soc.* **420** (2012) 2318–2324, arXiv:1104.2929 [astro-ph.CO].

[35] S. Dodelson and L. M. Widrow, "Sterile-neutrinos as dark matter," *Phys. Rev. Lett.* **72** (1994) 17–20, arXiv:hep-ph/9303287 [hep-ph].

[36] A. D. Dolgov and F. L. Villante, "BBN bounds on active sterile neutrino mixing," *Nucl. Phys.* **B679** (2004) 261–298, arXiv:hep-ph/0308083 [hep-ph].

[37] A. Kusenko, "Sterile neutrinos: The Dark side of the light fermions," *Phys.Rept.* **481** (2009) 1–28, `arXiv:0906.2968 [hep-ph]`.

[38] K. Abazajian, "Production and evolution of perturbations of sterile neutrino dark matter," *Phys.Rev.* **D73** (2006) 063506, `arXiv:astro-ph/0511630 [astro-ph]`.

[39] A. Dolgov and S. Hansen, "Massive sterile neutrinos as warm dark matter," *Astropart.Phys.* **16** (2002) 339–344, `arXiv:hep-ph/0009083 [hep-ph]`.

[40] K. Abazajian, G. M. Fuller, and M. Patel, "Sterile neutrino hot, warm, and cold dark matter," *Phys.Rev.* **D64** (2001) 023501, `arXiv:astro-ph/0101524 [astro-ph]`.

[41] T. Asaka, M. Laine, and M. Shaposhnikov, "Lightest sterile neutrino abundance within the nuMSM," *JHEP* **01** (2007) 091, `arXiv:hep-ph/0612182 [hep-ph]`. [Erratum: JHEP02,028(2015)].

[42] L. Wolfenstein, "Neutrino Oscillations in Matter," *Phys. Rev.* **D17** (1978) 2369–2374.

[43] S. P. Mikheev and A. Yu. Smirnov, "Resonant amplification of neutrino oscillations in matter and solar neutrino spectroscopy," *Nuovo Cim.* **C9** (1986) 17–26.

[44] S. P. Mikheev and A. Yu. Smirnov, "Resonance Amplification of Oscillations in Matter and Spectroscopy of Solar Neutrinos," *Sov. J. Nucl. Phys.* **42** (1985) 913–917. [Yad. Fiz.42,1441(1985)].

[45] X.-D. Shi and G. M. Fuller, "A New dark matter candidate: Nonthermal sterile neutrinos," *Phys. Rev. Lett.* **82** (1999) 2832–2835, `arXiv:astro-ph/9810076 [astro-ph]`.

[46] T. Asaka, S. Blanchet, and M. Shaposhnikov, "The nuMSM, dark matter and neutrino masses," *Phys. Lett.* **B631** (2005) 151–156, `arXiv:hep-ph/0503065 [hep-ph]`.

[47] T. Asaka and M. Shaposhnikov, "The nuMSM, dark matter and baryon asymmetry of the universe," *Phys. Lett.* **B620** (2005) 17–26, `arXiv:hep-ph/0505013 [hep-ph]`.

[48] T. Asaka, M. Shaposhnikov, and A. Kusenko, "Opening a new window for warm dark matter," *Phys. Lett.* **B638** (2006) 401–406, `arXiv:hep-ph/0602150 [hep-ph]`.

[49] M. Shaposhnikov and I. Tkachev, "The nuMSM, inflation, and dark matter," *Phys. Lett.* **B639** (2006) 414–417, `arXiv:hep-ph/0604236 [hep-ph]`.

[50] K. Petraki and A. Kusenko, "Dark-matter sterile neutrinos in models with a gauge singlet in the Higgs sector," *Phys. Rev.* **D77** (2008) 065014, `arXiv:0711.4646 [hep-ph]`.

[51] A. Kusenko, "Sterile neutrinos, dark matter, and the pulsar velocities in models with a Higgs singlet," *Phys. Rev. Lett.* **97** (2006) 241301, `arXiv:hep-ph/0609081 [hep-ph]`.

[52] J. McDonald, "Gauge singlet scalars as cold dark matter," *Phys. Rev.* **D50** (1994) 3637–3649, `arXiv:hep-ph/0702143 [HEP-PH]`.

[53] C. E. Yaguna, "The Singlet Scalar as FIMP Dark Matter," *JHEP* **08** (2011) 060, `arXiv:1105.1654 [hep-ph]`.

[54] A. Merle, V. Niro, and D. Schmidt, "New Production Mechanism for keV Sterile Neutrino Dark Matter by Decays of Frozen-In Scalars," *JCAP* **1403** (2014) 028, `arXiv:1306.3996 [hep-ph]`.

[55] A. Adulpravitchai and M. A. Schmidt, "A Fresh Look at keV Sterile Neutrino Dark Matter from Frozen-In Scalars," *JHEP* **01** (2015) 006, `arXiv:1409.4330 [hep-ph]`.

[56] Z. Kang, "Upgrading sterile neutrino dark matter to FI*m*P using scale invariance," *Eur. Phys. J.* **C75** no. 10, (2015) 471, `arXiv:1411.2773 [hep-ph]`.

[57] M. Frigerio and C. E. Yaguna, "Sterile Neutrino Dark Matter and Low Scale Leptogenesis from a Charged Scalar," *Eur. Phys. J.* **C75** no. 1, (2015) 31, `arXiv:1409.0659 [hep-ph]`.

[58] K. Kadota, "Sterile neutrino dark matter in warped extra dimensions," *Phys. Rev.* **D77** (2008) 063509, `arXiv:0711.1570 [hep-ph]`.

[59] A. Abada, G. Arcadi, and M. Lucente, "Dark Matter in the minimal Inverse Seesaw mechanism," *JCAP* **1410** (2014) 001, `arXiv:1406.6556 [hep-ph]`.

[60] B. Shakya, "Sterile Neutrino Dark Matter from Freeze-In," *Mod. Phys. Lett.* **A31** no. 06, (2016) 1630005, `arXiv:1512.02751 [hep-ph]`.

[61] D. Gorbunov and M. Shaposhnikov, "How to find neutral leptons of the νMSM?," *JHEP* **0710** (2007) 015, `arXiv:0705.1729 [hep-ph]`.

[62] M. Laine and M. Shaposhnikov, "Sterile neutrino dark matter as a consequence of nuMSM-induced lepton asymmetry," *JCAP* **0806** (2008) 031, `arXiv:0804.4543 [hep-ph]`.

[63] S. Tremaine and J. Gunn, "Dynamical Role of Light Neutral Leptons in Cosmology," *Phys.Rev.Lett.* **42** (1979) 407–410.

[64] A. Boyarsky, O. Ruchayskiy, and D. Iakubovskyi, "A Lower bound on the mass of Dark Matter particles," *JCAP* **0903** (2009) 005, `arXiv:0808.3902 [hep-ph]`.

[65] P. B. Pal and L. Wolfenstein, "Radiative Decays of Massive Neutrinos," *Phys.Rev.* **D25** (1982) 766.

[66] A. Boyarsky, A. Neronov, O. Ruchayskiy, and M. Shaposhnikov, "Constraints on sterile neutrino as a dark matter candidate from the diffuse x-ray background," *Mon. Not. Roy. Astron. Soc.* **370** (2006) 213–218, `arXiv:astro-ph/0512509 [astro-ph]`.

[67] R. Essig, E. Kuflik, S. D. McDermott, T. Volansky, and K. M. Zurek, "Constraining Light Dark Matter with Diffuse X-Ray and Gamma-Ray Observations," *JHEP* **1311** (2013) 193, `arXiv:1309.4091 [hep-ph]`.

[68] A. Boyarsky, J. Lesgourgues, O. Ruchayskiy, and M. Viel, "Lyman-alpha constraints on warm and on warm-plus-cold dark matter models," *JCAP* **0905** (2009) 012, `arXiv:0812.0010 [astro-ph]`.

[69] U. Seljak, A. Makarov, P. McDonald, and H. Trac, "Can sterile neutrinos be the dark matter?," *Phys. Rev. Lett.* **97** (2006) 191303, `arXiv:astro-ph/0602430 [astro-ph]`.

[70] A. D. Dolgov, "Neutrinos in cosmology," *Phys. Rept.* **370** (2002) 333–535, `arXiv:hep-ph/0202122 [hep-ph]`.

[71] A. Merle and M. Totzauer, "keV Sterile Neutrino Dark Matter from Singlet Scalar Decays: Basic Concepts and Subtle Features," *JCAP* **1506** (2015) 011, `arXiv:1502.01011 [hep-ph]`.

[72] Y. I. Izotov, T. X. Thuan, and N. G. Guseva, "A new determination of the primordial He abundance using the Hei $\lambda 10830$ emission line: cosmological implications," *Mon. Not. Roy. Astron. Soc.* **445** no. 1, (2014) 778–793, `arXiv:1408.6953 [astro-ph.CO]`.

[73] R. Cooke, M. Pettini, R. A. Jorgenson, M. T. Murphy, and C. C. Steidel, "Precision measures of the primordial abundance of deuterium," *Astrophys. J.* **781** no. 1, (2014) 31, `arXiv:1308.3240 [astro-ph.CO]`.

[74] Z. Hou, R. Keisler, L. Knox, M. Millea, and C. Reichardt, "How Massless Neutrinos Affect the Cosmic Microwave Background Damping Tail," *Phys. Rev.* **D87** (2013) 083008, `arXiv:1104.2333 [astro-ph.CO]`.

[75] M. Shaposhnikov, "The nuMSM, leptonic asymmetries, and properties of singlet fermions," *JHEP* **0808** (2008) 008, `arXiv:0804.4542 [hep-ph]`.

[76] A. Roy and M. Shaposhnikov, "Resonant production of the sterile neutrino dark matter and fine-tunings in the [nu]MSM," *Phys.Rev.* **D82** (2010) 056014, `arXiv:1006.4008 [hep-ph]`.

[77] P. Minkowski, "mu –> e gamma at a Rate of One Out of 1-Billion Muon Decays?," *Phys.Lett.* **B67** (1977) 421.

[78] R. N. Mohapatra and G. Senjanovic, "Neutrino Masses and Mixings in Gauge Models with Spontaneous Parity Violation," *Phys.Rev.* **D23** (1981) 165.

[79] T. Yanagida, "Horizontal Symmetry and Masses of Neutrinos," *Prog.Theor.Phys.* **64** (1980) 1103.

[80] M. Gell-Mann, P. Ramond, and R. Slansky, "Complex Spinors and Unified Theories," *Conf.Proc.* **C790927** (1979) 315–321, `arXiv:1306.4669 [hep-th]`.

[81] J. Schechter and J. Valle, "Neutrino Masses in SU(2) x U(1) Theories," *Phys.Rev.* **D22** (1980) 2227.

[82] A. Merle, "keV Neutrino Model Building," *Int.J.Mod.Phys.* **D22** (2013) 1330020, `arXiv:1302.2625 [hep-ph]`.

[83] **IceCube** Collaboration, M. Aartsen *et al.*, "First observation of PeV-energy neutrinos with IceCube," *Phys.Rev.Lett.* **111** (2013) 021103, `arXiv:1304.5356 [astro-ph.HE]`.

[84] N. Arkani-Hamed, L. J. Hall, H. Murayama, D. Tucker-Smith, and N. Weiner, "Small neutrino masses from supersymmetry breaking," *Phys. Rev.* **D64** (2001) 115011, `arXiv:hep-ph/0006312 [hep-ph]`.

[85] N. Arkani-Hamed, L. J. Hall, H. Murayama, D. Tucker-Smith, and N. Weiner, "Neutrino masses at v**(3/2)," `arXiv:hep-ph/0007001 [hep-ph]`.

[86] P. Langacker, "A Mechanism for ordinary sterile neutrino mixing," *Phys. Rev.* **D58** (1998) 093017, `arXiv:hep-ph/9805281 [hep-ph]`.

[87] A. Boyarsky, A. Neronov, O. Ruchayskiy, M. Shaposhnikov, and I. Tkachev, "Where to find a dark matter sterile neutrino?," *Phys. Rev. Lett.* **97** (2006) 261302, `arXiv:astro-ph/0603660 [astro-ph]`.

[88] A. Boyarsky, J. Nevalainen, and O. Ruchayskiy, "Constraints on the parameters of radiatively decaying dark matter from the dark matter halo of the Milky Way and Ursa Minor," *Astron. Astrophys.* **471** (2007) 51–57, `arXiv:astro-ph/0610961 [astro-ph]`.

[89] A. Boyarsky, D. Iakubovskyi, O. Ruchayskiy, and V. Savchenko, "Constraints on decaying Dark Matter from XMM-Newton observations of M31," *Mon. Not. Roy. Astron. Soc.* **387** (2008) 1361, `arXiv:0709.2301 [astro-ph]`.

[90] A. Boyarsky, D. Malyshev, A. Neronov, and O. Ruchayskiy, "Constraining DM properties with SPI," *Mon. Not. Roy. Astron. Soc.* **387** (2008) 1345, `arXiv:0710.4922 [astro-ph]`.

[91] A. Boyarsky, O. Ruchayskiy, and M. Shaposhnikov, "The Role of sterile neutrinos in cosmology and astrophysics," *Ann.Rev.Nucl.Part.Sci.* **59** (2009) 191–214, `arXiv:0901.0011 [hep-ph]`.

[92] A. Boyarsky, J. Lesgourgues, O. Ruchayskiy, and M. Viel, "Realistic sterile neutrino dark matter with keV mass does not contradict cosmological bounds," *Phys. Rev. Lett.* **102** (2009) 201304, `arXiv:0812.3256 [hep-ph]`.

[93] A. Harada, A. Kamada, and N. Yoshida, "Structure formation in a mixed dark matter model with decaying sterile neutrino: the 3.5 keV X-ray line and the Galactic substructure," `arXiv:1412.1592 [astro-ph.CO]`.

[94] B. Shuve and I. Yavin, "Dark matter progenitor: Light vector boson decay into sterile neutrinos," *Phys. Rev.* **D89** no. 11, (2014) 113004, `arXiv:1403.2727 [hep-ph]`.

[95] L. Lello and D. Boyanovsky, "Cosmological Implications of Light Sterile Neutrinos produced after the QCD Phase Transition," *Phys. Rev.* **D91** (2015) 063502, `arXiv:1411.2690 [astro-ph.CO]`.

[96] D. Boyanovsky, "Clustering properties of a sterile neutrino dark matter candidate," *Phys. Rev.* **D78** (2008) 103505, `arXiv:0807.0646 [astro-ph]`.

[97] A. Kusenko, F. Takahashi, and T. T. Yanagida, "Dark Matter from Split Seesaw," *Phys.Lett.* **B693** (2010) 144–148, `arXiv:1006.1731 [hep-ph]`.

[98] M. Blennow, E. Fernandez-Martinez, and B. Zaldivar, "Freeze-in through portals," *JCAP* **1401** no. 01, (2014) 003, `arXiv:1309.7348 [hep-ph]`.

[99] S. Khalil and O. Seto, "Sterile neutrino dark matter in B - L extension of the standard model and galactic 511-keV line," *JCAP* **0810** (2008) 024, `arXiv:0804.0336 [hep-ph]`.

[100] P. S. Bhupal Dev, A. Mazumdar, and S. Qutub, "Constraining Non-thermal and Thermal properties of Dark Matter," *Front. Phys.* **2** (2014) 26, `arXiv:1311.5297 [hep-ph]`.

[101] G. M. Fuller, C. T. Kishimoto, and A. Kusenko, "Heavy sterile neutrinos, entropy and relativistic energy production, and the relic neutrino background," `arXiv:1110.6479 [astro-ph.CO]`.

[102] P. Hernandez, M. Kekic, and J. Lopez-Pavon, "N_{eff} in low-scale seesaw models versus the lightest neutrino mass," *Phys.Rev.* **D90** (2014) 065033, `arXiv:1406.2961 [hep-ph]`.

[103] A. C. Vincent, E. F. Martinez, P. Hernandez, M. Lattanzi, and O. Mena, "Revisiting cosmological bounds on sterile neutrinos," `arXiv:1408.1956 [astro-ph.CO]`.

[104] **PIENU** Collaboration, M. Aoki *et al.*, "Search for Massive Neutrinos in the Decay $\pi \to e\nu$," *Phys.Rev.* **D84** (2011) 052002, `arXiv:1106.4055 [hep-ex]`.

[105] **CHARM** Collaboration, F. Bergsma *et al.*, "A Search for Decays of Heavy Neutrinos in the Mass Range 0.5-GeV to 2.8-GeV," *Phys.Lett.* **B166** (1986) 473.

[106] O. Ruchayskiy and A. Ivashko, "Experimental bounds on sterile neutrino mixing angles," *JHEP* **1206** (2012) 100, `arXiv:1112.3319 [hep-ph]`.

[107] G. Bernardi *et al.*, "Search for Neutrino Decay," *Phys. Lett.* **B166** (1986) 479–483.

[108] G. Bernardi *et al.*, "Further Limits on Heavy Neutrino Couplings," *Phys. Lett.* **B203** (1988) 332–334.

[109] **NuTeV, E815** Collaboration, A. Vaitaitis *et al.*, "Search for neutral heavy leptons in a high-energy neutrino beam," *Phys. Rev. Lett.* **83** (1999) 4943–4946, `arXiv:hep-ex/9908011 [hep-ex]`.

[110] J. Casas and A. Ibarra, "Oscillating neutrinos and $\mu \to e, \gamma$," *Nucl.Phys.* **B618** (2001) 171–204, `arXiv:hep-ph/0103065 [hep-ph]`.

[111] S. Horiuchi, P. J. Humphrey, J. Onorbe, K. N. Abazajian, M. Kaplinghat, and S. Garrison-Kimmel, "Sterile neutrino dark matter bounds from galaxies of the Local Group," *Phys. Rev.* **D89** no. 2, (2014) 025017, `arXiv:1311.0282 [astro-ph.CO]`.

[112] M. Nemevsek, G. Senjanovic, and Y. Zhang, "Warm Dark Matter in Low Scale Left-Right Theory," *JCAP* **1207** (2012) 006, `arXiv:1205.0844 [hep-ph]`.

[113] F. Bezrukov, H. Hettmansperger, and M. Lindner, "keV sterile neutrino Dark Matter in gauge extensions of the Standard Model," *Phys. Rev.* **D81** (2010) 085032, `arXiv:0912.4415 [hep-ph]`.

[114] A. V. Patwardhan, G. M. Fuller, C. T. Kishimoto, and A. Kusenko, "Diluted equilibrium sterile neutrino dark matter," *Phys. Rev.* **D92** no. 10, (2015) 103509, `arXiv:1507.01977 [astro-ph.CO]`.

[115] A. Falkowski, J. T. Ruderman, and T. Volansky, "Asymmetric Dark Matter from Leptogenesis," *JHEP* **05** (2011) 106, `arXiv:1101.4936 [hep-ph]`.

[116] A. Biswas and A. Gupta, "Freeze-in Production of Sterile Neutrino Dark Matter in U(1)$_{\rm B-L}$ Model," `arXiv:1607.01469 [hep-ph]`.

[117] S. Horiuchi, B. Bozek, K. N. Abazajian, M. Boylan-Kolchin, J. S. Bullock, S. Garrison-Kimmel, and J. Onorbe, "Properties of resonantly produced sterile neutrino dark matter subhaloes," *Mon. Not. Roy. Astron. Soc.* **456** no. 4, (2016) 4346–4353, `arXiv:1512.04548 [astro-ph.CO]`.

[118] A. Schneider, "Astrophysical constraints on resonantly produced sterile neutrino dark matter," *JCAP* **1604** no. 04, (2016) 059, `arXiv:1601.07553 [astro-ph.CO]`.

[119] S. F. King and A. Merle, "Warm Dark Matter from keVins," *JCAP* **1208** (2012) 016, `arXiv:1205.0551 [hep-ph]`.

[120] D. J. H. Chung, E. W. Kolb, and A. Riotto, "Production of massive particles during reheating," *Phys. Rev.* **D60** (1999) 063504, `arXiv:hep-ph/9809453 [hep-ph]`.

[121] J. Knig, A. Merle, and M. Totzauer, "keV Sterile Neutrino Dark Matter from Singlet Scalar Decays: The Most General Case," `arXiv:1609.01289 [hep-ph]`.

[122] R. J. Scherrer and M. S. Turner, "Decaying Particles Do Not Heat Up the Universe," *Phys. Rev.* **D31** (1985) 681.

[123] R. H. Cyburt, B. D. Fields, K. A. Olive, and T.-H. Yeh, "Big Bang Nucleosynthesis: 2015," *Rev. Mod. Phys.* **88** (2016) 015004, `arXiv:1505.01076 [astro-ph.CO]`.

[124] D. Hooper, F. S. Queiroz, and N. Y. Gnedin, "Non-Thermal Dark Matter Mimicking An Additional Neutrino Species In The Early Universe," *Phys. Rev.* **D85** (2012) 063513, `arXiv:1111.6599 [astro-ph.CO]`.

[125] C. S. Fong, H. Minakata, B. Panes, and R. Z. Funchal, "Possible Interpretations of IceCube High-Energy Neutrino Events," *JHEP* **1502** (2015) 189, `arXiv:1411.5318 [hep-ph]`.

[126] Y. Ema, R. Jinno, and T. Moroi, "Cosmic-Ray Neutrinos from the Decay of Long-Lived Particle and the Recent IceCube Result," *Phys.Lett.* **B733** (2014) 120–125, `arXiv:1312.3501 [hep-ph]`.

[127] Y. Ema, R. Jinno, and T. Moroi, "Cosmological Implications of High-Energy Neutrino Emission from the Decay of Long-Lived Particle," *JHEP* **1410** (2014) 150, `arXiv:1408.1745 [hep-ph]`.

[128] B. Feldstein, A. Kusenko, S. Matsumoto, and T. T. Yanagida, "Neutrinos at IceCube from Heavy Decaying Dark Matter," *Phys.Rev.* **D88** no. 1, (2013) 015004, `arXiv:1303.7320 [hep-ph]`.

[129] A. Esmaili and P. D. Serpico, "Are IceCube neutrinos unveiling PeV-scale decaying dark matter?," *JCAP* **1311** (2013) 054, `arXiv:1308.1105 [hep-ph]`.

[130] A. Esmaili, S. K. Kang, and P. D. Serpico, "IceCube events and decaying dark matter: hints and constraints," *JCAP* **1412** no. 12, (2014) 054, `arXiv:1410.5979 [hep-ph]`.

[131] Y. Bai, R. Lu, and J. Salvado, "Geometric Compatibility of IceCube TeV-PeV Neutrino Excess and its Galactic Dark Matter Origin," `arXiv:1311.5864 [hep-ph]`.

[132] A. Bhattacharya, M. H. Reno, and I. Sarcevic, "Reconciling neutrino flux from heavy dark matter decay and recent events at IceCube," *JHEP* **1406** (2014) 110, `arXiv:1403.1862 [hep-ph]`.

[133] T. Higaki, R. Kitano, and R. Sato, "Neutrinoful Universe," *JHEP* **1407** (2014) 044, `arXiv:1405.0013 [hep-ph]`.

[134] A. Bhattacharya, R. Gandhi, and A. Gupta, "The Direct Detection of Boosted Dark Matter at High Energies and PeV events at IceCube," *JCAP* **1503** no. 03, (2015) 027, `arXiv:1407.3280 [hep-ph]`.

[135] C. Rott, K. Kohri, and S. C. Park, "Superheavy dark matter and IceCube neutrino signals:bounds on decaying dark matter," `arXiv:1408.4575 [hep-ph]`.

[136] T. E. Jeltema and S. Profumo, "Discovery of a 3.5 keV line in the Galactic Center and a Critical Look at the Origin of the Line Across Astronomical Targets," `arXiv:1408.1699 [astro-ph.HE]`.

[137] A. Boyarsky, J. Franse, D. Iakubovskyi, and O. Ruchayskiy, "Comment on the paper "Dark matter searches going bananas: the contribution of Potassium (and Chlorine) to the 3.5 keV line" by T. Jeltema and S. Profumo," `arXiv:1408.4388 [astro-ph.CO]`.

[138] E. Bulbul, M. Markevitch, A. R. Foster, R. K. Smith, M. Loewenstein, *et al.*, "Comment on "Dark matter searches going bananas: the contribution of Potassium (and Chlorine) to the 3.5 keV line"," `arXiv:1409.4143 [astro-ph.HE]`.

[139] D. Malyshev, A. Neronov, and D. Eckert, "Constraints on 3.55 keV line emission from stacked observations of dwarf spheroidal galaxies," *Phys.Rev.* **D90** no. 10, (2014) 103506, `arXiv:1408.3531 [astro-ph.HE]`.

[140] M. E. Anderson, E. Churazov, and J. N. Bregman, "Non-Detection of X-Ray Emission From Sterile Neutrinos in Stacked Galaxy Spectra," `arXiv:1408.4115 [astro-ph.HE]`.

[141] S. Riemer-Sorensen, "Questioning a 3.5 keV dark matter emission line," `arXiv:1405.7943 [astro-ph.CO]`.

[142] A. Boyarsky, J. Franse, D. Iakubovskyi, and O. Ruchayskiy, "Checking the dark matter origin of 3.53 keV line with the Milky Way center," `arXiv:1408.2503 [astro-ph.CO]`.

[143] K. Griest and M. Kamionkowski, "Unitarity Limits on the Mass and Radius of Dark Matter Particles," *Phys.Rev.Lett.* **64** (1990) 615.

[144] J. F. Navarro, C. S. Frenk, and S. D. White, "The Structure of cold dark matter halos," *Astrophys.J.* **462** (1996) 563–575, arXiv:astro-ph/9508025 [astro-ph].

[145] M. R. Lovell, C. S. Frenk, V. R. Eke, A. Jenkins, L. Gao, *et al.*, "The properties of warm dark matter haloes," *Mon.Not.Roy.Astron.Soc.* **439** no. 1, (2014) 300–317, arXiv:1308.1399 [astro-ph.CO].

[146] A. Ibarra and D. Tran, "Gamma Ray Spectrum from Gravitino Dark Matter Decay," *Phys.Rev.Lett.* **100** (2008) 061301, arXiv:0709.4593 [astro-ph].

[147] T. Sjstrand, S. Ask, J. R. Christiansen, R. Corke, N. Desai, *et al.*, "An Introduction to PYTHIA 8.2," *Comput.Phys.Commun.* **191** (2015) 159–177, arXiv:1410.3012 [hep-ph].

[148] C.-Y. Chen, P. S. B. Dev, and A. Soni, "A Possible Two-component Flux for the High Energy Neutrino Events at IceCube," arXiv:1411.5658 [hep-ph].

[149] D. V. Semikoz and G. Sigl, "Ultrahigh-energy neutrino fluxes: New constraints and implications," *JCAP* **0404** (2004) 003, arXiv:hep-ph/0309328 [hep-ph].

[150] **Fermi-LAT** Collaboration, M. Ackermann *et al.*, "The spectrum of isotropic diffuse gamma-ray emission between 100 MeV and 820 GeV," *Astrophys.J.* **799** no. 1, (2015) 86, arXiv:1410.3696 [astro-ph.HE].

[151] K. Murase, R. Laha, S. Ando, and M. Ahlers, "Testing the Dark Matter Scenario for PeV Neutrinos Observed in IceCube," arXiv:1503.04663 [hep-ph].

[152] A. Esmaili and P. D. Serpico, "Gamma-ray bounds from EAS detectors and heavy decaying dark matter constraints," arXiv:1505.06486 [hep-ph].

[153] "Ams-02 collaboration, talks at the 'AMS Days at CERN', 15-17 April 2015..".

[154] G. Giesen, M. Boudaud, Y. Genolini, V. Poulin, M. Cirelli, *et al.*, "AMS-02 antiprotons, at last! Secondary astrophysical component and immediate implications for Dark Matter," arXiv:1504.04276 [astro-ph.HE].

[155] K. N. Abazajian, "Resonantly Produced 7 keV Sterile Neutrino Dark Matter Models and the Properties of Milky Way Satellites," *Phys.Rev.Lett.* **112** no. 16, (2014) 161303, arXiv:1403.0954 [astro-ph.CO].

[156] A. Merle and A. Schneider, "Production of Sterile Neutrino Dark Matter and the 3.5 keV line," arXiv:1409.6311 [hep-ph].

[157] N. Haba, H. Ishida, and R. Takahashi, "ν_R dark matter-philic Higgs for 3.5 keV X-ray signal," *Phys.Lett.* **B743** (2015) 35–38, `arXiv:1407.6827 [hep-ph]`.

[158] W. Rodejohann and H. Zhang, "Signatures of Extra Dimensional Sterile Neutrinos," *Phys.Lett.* **B737** (2014) 81–89, `arXiv:1407.2739 [hep-ph]`.

[159] H. Ishida and H. Okada, "3.55 keV X-ray Line Interpretation in Radiative Neutrino Model," `arXiv:1406.5808 [hep-ph]`.

[160] D. J. Robinson and Y. Tsai, "Dynamical framework for KeV Dirac neutrino warm dark matter," *Phys.Rev.* **D90** no. 4, (2014) 045030, `arXiv:1404.7118 [hep-ph]`.

[161] S. Chakraborty, D. K. Ghosh, and S. Roy, "7 keV Sterile neutrino dark matter in $U(1)_R-$ lepton number model," *JHEP* **1410** (2014) 146, `arXiv:1405.6967 [hep-ph]`.

[162] S. Patra and P. Pritimita, "7 keV sterile neutrino Dark Matter in extended seesaw framework," `arXiv:1409.3656 [hep-ph]`.

[163] T. Tsuyuki, "Neutrino masses, leptogenesis, and sterile neutrino dark matter," *Phys.Rev.* **D90** (2014) 013007, `arXiv:1403.5053 [hep-ph]`.

[164] S. K. Kang and A. Patra, "keV Sterile Neutrino Dark Matter and Low Scale Leptogenesis," `arXiv:1412.4899 [hep-ph]`.

[165] H. Ishida, K. S. Jeong, and F. Takahashi, "7 keV sterile neutrino dark matter from split flavor mechanism," *Phys.Lett.* **B732** (2014) 196–200, `arXiv:1402.5837 [hep-ph]`.

[166] F. Bezrukov and D. Gorbunov, "Relic Gravity Waves and 7 keV Dark Matter from a GeV scale inflaton," *Phys.Lett.* **B736** (2014) 494–498, `arXiv:1403.4638 [hep-ph]`.

[167] K. P. Modak, "3.5 keV X-ray Line Signal from Decay of Right-Handed Neutrino due to Transition Magnetic Moment," *JHEP* **03** (2015) 064, `arXiv:1404.3676 [hep-ph]`.

[168] B. Moore, S. Ghigna, F. Governato, G. Lake, T. R. Quinn, *et al.*, "Dark matter substructure within galactic halos," *Astrophys.J.* **524** (1999) L19–L22, `arXiv:astro-ph/9907411 [astro-ph]`.

[169] A. V. Kravtsov, "Dark matter substructure and dwarf galactic satellites," *Adv.Astron.* **2010** (2010) 281913, `arXiv:0906.3295 [astro-ph.CO]`.